SILESIAN UNIVERSITY OF TECHNOLOGY

Faculty of Automatic Control, Electronics and Computer Science

Department of Measurements and Control Systems

Doctoral Dissertation

Application of smart materials for selected vibration reduction problems

Author: Jarosław Rzepecki

Supervisor: prof. dr hab. inż. Marek Pawełczyk

Gliwice, February 2022

To my wife Martyna,
and my parents Małgorzata and Jerzy

Abstract

Vibration is a phenomenon that is commonly used in technology, e.g., in musical instruments or resonant circuits. However, vibration may also be a side effect of working machinery devices or household appliances, which is associated with discomfort and, in extreme situations, with negative impact on human health. Thus, the methods for vibration reduction are employed, i.e. passive, semi-active, and active.

In this dissertation smart materials are applied for reduction of the vibrations in a road vehicle and a device casing with the size of a typical household appliance. Semi-active methods are mainly used, however, in some cases passive and active methods are also investigated to compare the efficiency of different solutions.

The vibration generated by a device enclosed inside the casing can be reduced using many approaches varying from the use of additional damping material layers to active reduction with the use of electrodynamic exciters. In the presented research a semi-active approach with piezoelectric elements attached on a single panel front wall of casing is investigated. The proper dissipation of the absorbed mechanical energy may increase the efficiency of vibration damping.

The use of a double-panel structure instead of a single panel may reduce the propagation of the vibration outside the casing. Moreover, the additional coupling elements mounted between the panels can provide improvement of the efficiency of vibration reduction. In this dissertation a new type of electromagnetic coupling element is presented and validated. This element placed as a link between the panels allows to achieve the reduction of maximal and mean values of the transmitted vibration energy.

The road vehicles are equipped with suspension to improve comfort and safety during the driving. The most popular solutions are passive systems, while semi-active and active suspensions are usually available in premium cars. The presented results were obtained during the experiments performed for the semi-active suspension based on magnetorheological (MR) dampers. The different approach in estimation of the velocity of the suspension using linear variable differential transformer (LVDT) sensors is also presented.

Streszczenie

Drgania są zjawiskiem powszechnie stosowanym w technologii, np. w instrumentach muzycznych lub obwodach rezonansowych. Drgania mogą być również efektem ubocznym pracy maszyn lub urządzeń gospodarstwa domowego, co wiąże się z dyskomfortem, a w skrajnych sytuacjach z negatywnym wpływem na zdrowie człowieka. Stosowane są więc metody redukcji drgań: pasywne, półaktywne i aktywne.

W niniejszej rozprawie zastosowano inteligentne materiały w celu redukcji drgań w pojeździe drogowym oraz drgań obudowy urządzenia o wielkości typowego sprzętu gospodarstwa domowego. Wykorzystano głównie metody półaktywne, jednak w niektórych przypadkach badane są również metody pasywne i aktywne w celu porównania skuteczności różnych rozwiązań.

Drgania generowane przez urządzenia zamknięte wewnątrz obudowy można redukować na wiele sposobów: od użycia dodatkowych warstw materiału tłumiącego po aktywną redukcję z użyciem wzbudników elektrodynamicznych. W prezentowanych badaniach rozpatrywane jest podejście półaktywne z elementami piezoelektrycznymi zamontowanymi na jednopanelowej, czołowej ścianie obudowy. Odpowiednie rozpraszanie pochłoniętej energii mechanicznej może zwiększyć skuteczność tłumienia drgań.

Zastosowanie konstrukcji dwupanelowej zamiast jednopanelowej może ograniczyć propagację drgań na zewnątrz obudowy. Ponadto, dodatkowe elementy sprzęgające zamontowane pomiędzy panelami mogą poprawić skuteczność redukcji drgań. W rozprawie przedstawiono i zwalidowano nowy typ elektromagnetycznego elementu sprzęgającego. Dzięki zastosowaniu takiego elementu jako łącznika pomiędzy panelami można osiągnąć redukcję maksymalnych i średnich wartości energii drgań.

Pojazdy drogowe wyposażone są w zawieszenia poprawiające komfort i bezpieczeństwo podczas jazdy. Najpopularniejszymi rozwiązaniami są systemy pasywne, natomiast zawieszenia półaktywne i aktywne dostępne są zazwyczaj w samochodach klasy premium. Przedstawione wyniki uzyskano podczas eksperymentów przeprowadzonych dla półaktywnego zawieszenia, opartego na tłumikach MR. Przedstawiono również odmienne podejście w estymacji prędkości zawieszenia poprzez użycie czujników LVDT.

Acknowledgements

The author would like to thank Professor Marek Pawełczyk for his supervision, encouragement, and support.

The author would also like to thank Anna Chrapońska for being a great coworker and friend, and for the fruitful long-term cooperation with joint research.

The author would also like to thank members of the Department of Measurement and Control Systems for a friendly atmosphere, cooperation and valuable comments.

The research has been partially supported by the National Science Centre, Poland, decision no. DEC-2017/25/B/ST7/02236, and by the Ministry of Education and Science.

Finally, to my wife Martyna and family for their patience, support and keeping me motivated.

Contents

1 Introduction **1**

1.1 Vibration of devices 1
1.2 Passive methods 2
1.3 Semi-active methods 3
1.4 Active methods 4
1.5 Smart materials 5
1.6 Motivation for the research 6
1.7 Objective and thesis 7
1.8 Contents 7

2 Laboratory equipment **9**

2.1 Background 9
2.2 Rigid frame device casing 9
2.2.1 Description of system 9
2.2.2 Casing walls 11
2.2.3 Measurement and control system 15
2.3 All-terrain vehicle with semi-active suspension 18
2.3.1 Description of system 18
2.3.2 MR dampers 19
2.3.3 Measurement and control system 19
2.4 Acoustic camera 22
2.4.1 Description of device 22
2.4.2 Microphone array geometries 23
2.4.3 Measurement system 26
2.4.4 Preliminary validation 27

3 Device casing with a single panel **29**

3.1 Background 29

3.2 Single panel modeling 30
3.2.1 Isotropic steel panel 30
3.2.2 Orthotropic aluminum panel 31
3.3 Piezoelectric shunt damping 32
3.3.1 Passive circuit 32
3.3.2 Switching circuit 33
3.4 Synchronized switch damping 33
3.4.1 Isotropic steel panel 34
3.4.2 Orthotropic aluminum panel 37
3.5 Influence of casing walls on front panel frequency response 41
3.6 Single electromagnetic coupling 45
3.7 Discussion 48

4 Device casing with a double-panel structure 49
4.1 Background 49
4.2 Electromagnetic couplings 50
4.2.1 Semi-active electromagnetic element for damping of transverse vibration of planar structures 50
4.2.2 Properties of electromagnetic couplings 51
4.2.3 Vibration damping using single coupling 55
4.2.4 Vibration damping using five couplings 61
4.3 Modified Chladni's method 75
4.3.1 Electromagnetic couplings case 77
4.3.2 Stiff couplings case 81
4.4 Discussion 84

5 Magnetorheological vehicle suspension 85
5.1 Background 85
5.2 Vehicle suspension modeling 86
5.3 Vibration attenuation 87
5.4 Estimation of suspension velocity using LVDT 92
5.5 Discussion 95

6 Summary 97
6.1 Conclusion 97
6.2 Author's contribution 99
6.3 Further research 99

Nomenclature

Acronyms

MR — Magnetorheological

LVDT — Linear variable differential transformer

LDV — Laser-Doppler vibrometer

HVAC — Heating, ventilation, air conditioning

ER — Electrorheological

SMA — Shape-memory alloy

DE — Dielectric elastomer

SME — Shape-memory effect

SE — Superelasticity

MFC — Macro fiber composite

IR — Infrared

ATV — All-terrain vehicle

MCU — Microcontroller unit

IMU — Inertial measurement unit

DOA — Direction of arrival

MUSIC — Multiple signal classification

BSR — Buzz, squeak, rattle

GLCM — Gray level coocurrence matrix

AMS — Average microphone spacing

SONAH — Statistically optimised near-field acoustic holography

DAC — Digital to analog converter

PSD — Power spectral density

CLD — Constrained layer damping

ATVA — Actively tunable vibration absorber

PSDa — Piezoelectric shunt damping

PZT — Lead zirconate titane

Opamp — Operational amplifier

SSD — Synchronized switch damping
SSDI — Synchronized switch damping on inductor
SSDS — Synchronized switch damping with short circuit
SSDV — Synchronized switch damping on voltage sources
SSDVa — Synchronized switch damping on adaptive voltage sources
SSDNC — Synchronized switch damping with negative capacitance
DDS — Direct digital synthesizer
DAQ — Data acquisition
MOSFET — Metal-oxide semiconductor field-effect transistor
PCB — Printed circuit board
ESD — Energy spectral density
SPL — Sound pressure level
PSU — Power supply unit
PC — Phononic crystal
RMS — Root mean square
FRF — Frequency response function
PWM — Pulse-width modulation
DIC — Digital image correlation
MIMO — Multiple input, multiple output
DoF — Degrees of freedom

Symbols

D — Flexural rigidity
$w(x,y,t)$ — Transverse displacement dependent on x,y directions and time
E — Young's modulus
ρ — Mass density per unit area of the panel
t — Continuous time
h — Thickness of a plate
ν — Poisson's ratio
∇^2 — Laplacian operator
G — Rigidity modulus
H — Hysteresis
DC_{up} — Value of duty cycle up
DC_{dw} — Value of duty cycle down
DC_{max} — Maximal value of duty cycle
M — Mass matrix

C — Damping matrix

K — Stiffness matrix

x — Displacement of vibrating structure

F — Force generated by MR damper

m_u — Unsprung mass

m_s — Sprung mass

c_u — Damping between unsprung mass and road

c_s — Damping between unsprung and sprung mass

k_u — Stiffness between unsprung mass and road

k_s — Stiffness between unsprung and sprung mass

δ — Gain factor

v_s — Velocity of sprung mass

v_u — Velocity of usprung mass

v_{mr} — Suspension velocity

i_{mr} — Current applied to MR damper

α_0, α_1, β_0, c_0, c_1 — Constant parameters of inverse model of MR damper

List of Tables

2.1 Main parameters of panels. 11
2.2 Main technical data of investigated ATV. 18
2.3 Main parameters of investigated array geometries. 24
2.4 Main parameters of Panasonic WM-61A microphones. 26

3.1 Sensors coordinates. 40
3.2 Power of the signals measured by microphones and LDV, for investigated circuits. 40

4.1 Differences of energy values between ON and OFF states for the 4^{th} mode. 59
4.2 Differences of energy values between ON and OFF states for the 5^{th} mode. 59
4.3 Differences of energy values between ON and OFF states for the 11^{th} mode. 60
4.4 Differences of energy values between ON and OFF states for the 12^{th} mode. 60
4.5 Maximal energy values obtained on MFC elements, depending on the number of coupling elements and duty cycle of PWM signal, up to 500 Hz. 67
4.6 Mean energy values obtained on MFC elements, depending on the number of coupling elements and duty cycle of PWM signal, up to 500 Hz. 68
4.7 Advantages and disadvantages of the considered methods. 75
4.8 Temperature of panel for 11 V coil supply voltage, depending on time. . 80

5.1 RMS values of vertical acceleration with corresponding values of current. 92

List of Figures

2.1 Schemes of described rigid frame. 10
2.2 Interior of the casing covered by a layer of acoustic foam. 11
2.3 Simulation results for the first fifteen modeshapes of the isotropic, 0.5 mm thick, steel, single panel used in experiments. 12
2.4 Simulation results for the first fifteen modeshapes of the orthotropic, 1.0 mm thick, aluminum, single panel used in experiments. 13
2.5 Panels used in the experiments. 14
2.6 Equipment used in main experiments on rigid frame casing, with selected parameters listed in tables. 17
2.7 Investigated ATV. 18
2.8 Construction of MR damper. 19
2.9 Equipment used in main experiments on ATV, with selected parameters. 22
2.10 Compared microphone array geometries. 23
2.11 Prototypes of acoustic cameras. 24
2.12 Normalized sound intensity maps for investigated arrays. 25
2.13 Scheme of measurement and control system for the acoustic camera. . . 26
2.14 Test objects for acoustic camera. 27
2.15 Mean PSD for hair dryer with amplitude normalized to 1. 27
2.16 Mean PSD for fan with amplitude normalized to 1. 28
2.17 Mean PSD for small fans with amplitude normalized to 1. 28

3.1 Rigid device casing with MFC elements used in the experiment. 34
3.3 Electrical representation of implemented passive SSDI circuit. 35
3.4 Scheme of measurement and control system for the SSDI experiment with isotropic panel. 36
3.5 ESD of measured vibration for open, short, and SSDI circuits. 36
3.6 Displacement of the central point of vibrating structure for open, short, and SSDI circuits. 37

3.7 Rigid device casing with MFC elements used in experiment. 37
3.8 Electrical representation of implemented semi-active SSDI. 38
3.9 Scheme of measurement and control system for SSDI and SSDV experiment with orthotropic panel. 39
3.10 Scheme of the placement of microphones, LDV, and the casing. 39
3.11 Scheme of experimental setup for measurement of panel's response characteristics. 41
3.12 ESD of measured vibration for the walls made from different materials, with a single panel as a front wall. 42
3.13 ESD of measured vibration for the frame with a double-panel structure. 43
3.14 ESD of measured vibration for foams with a single panel, and foams with a double-panel structure. 44
3.15 ESD of measured vibration for aluminum with a single panel, aluminum with a double-panel structure, and aluminum with foams and a single panel. 44
3.16 Laboratory setup used in the experiment. 45
3.17 Scheme of measurement and control system for a single panel with a single electromagnetic element. 46
3.18 Measurement points and the placement of coupling. 46
3.19 Velocity of panel's vibration measured in the point no. 1. 47
3.20 Velocity of panel's vibration measured in the point no. 2. 47

4.1 Proposed semi-active damper, mounted in different configurations. . . . 51
4.2 Solenoid before modifications, and Acculab VI-3mg electronic scale with solenoid mounted on stand. 52
4.3 Comparison of solenoids' characteristics of force in PWM's duty cycle function, depending on core's displacement and coil supply voltage. . . 53
4.4 Comparison of solenoids' characteristics of force in PWM's duty cycle function, depending on PWM frequency. 54
4.5 Hysteresis loop of investigated solenoid. 54
4.6 Enlargement of interpolated measurements of hysteresis loop. 55
4.7 Coil and a core before mountage on radiating panel. 56
4.8 Scheme of measurement and control system for a double-panel structure with a single electromagnetic coupling. 56
4.9 Grid of measurement points distributed on a panel. 57
4.10 Mean ESD of measured vibration for ON and OFF states. 57

4.11 Energy distribution on panel presented as a color map, for ON state, for the four selected modes with contours of corresponding, simulated modeshapes. 58
4.12 Placement of electromagnetic couplings and attachement of the coils. . 61
4.13 Enlargement of the incident panel with attached coils. 61
4.14 Scheme of measurement and control system for a double-panel structure with five electromagnetic couplings. 62
4.15 Frequency patterns generated from values of vibration energy for every MFC element, and different combinations of coupling numbers. 63
4.16 ESD of measured vibration for zero couplings, the best case and the worst case for MFC1. 69
4.17 ESD of measured vibration for zero couplings, the best case and the worst case for MFC2. 70
4.18 ESD of measured vibration for zero couplings, the best case and the worst case for MFC3. 70
4.19 ESD of measured vibration for zero couplings, the best case and the worst case for MFC4. 71
4.20 ESD of measured vibration for zero couplings, the best case and the worst case for MFC5. 71
4.21 ESD of measured vibration for zero couplings, and one coupling with 99% duty cycle of PWM signal, for MFC1. 72
4.22 ESD of measured vibration for zero couplings, and one coupling with 99% duty cycle of PWM signal, for MFC2. 73
4.23 ESD of measured vibration for zero couplings, and one coupling with 99% duty cycle of PWM signal, for MFC3. 73
4.24 ESD of measured vibration for zero couplings, and one coupling with 99% duty cycle of PWM signal, for MFC4. 74
4.25 ESD of measured vibration for zero couplings, and one coupling with 99% duty cycle of PWM signal, for MFC5. 74
4.26 Schemes of casing configuration used in experiment. 77
4.27 Scheme of measurement and control system for modified Chladni's experiment. 77
4.28 Vision images of modeshapes for 90 Hz with the different numbers of activated couplings. 78
4.29 Obtained modeshape presented with the use of different types of images and filters. 79

4.30 Modeshapes for 90 Hz, depending on number of activated couplings. . . 80
4.31 Packet of neodymium magnets, and the placement of couplings on the panel. 81
4.32 5^{th} modeshape for different combinations of couplings. 82
4.33 13^{th} modeshape for different combinations of couplings. 82
4.34 14^{th} modeshape for different combinations of couplings. 83

5.1 General scheme of MIMO system for investigated vehicle. 86
5.2 Quarter model of investigated vehicle. 87
5.3 Scheme of measurement and control system for semi-active suspension of a single quarter of an ATV. 89
5.4 0.08 m thick wooden beam, used as an obstacle, compared with investigated vehicle. 89
5.5 Stages of the movement of the vehicle through the 0.08 m wooden beam. 90
5.6 Velocity of the suspension estimated for each wheel and different currents 91
5.7 Comparison of vertical acceleration affecting on driver, for different currents. 92
5.8 Estimation of vertical suspension velocity of rear left quarter of vehicle using accelerometers and LVDT for different control currents. 93
5.9 Comparison of vertical acceleration affecting on driver, for suspension velocity estimated using accelerometers and LVDT. 94

Chapter 1

Introduction

1.1 Vibration of devices

Vibrations are a subject of people's interest since the creation of the first musical instrument, and the knowledge in this area was developed by ancient civilizations, especially the Greek. Pythagoras (582—507 B.C.) is considered as a pioneer, who scientifically investigated sound. In the second century, Zhang Heng invented the first seismograph in the aftermath of many earthquakes that struck Chinese civilization. Galileo Galilei studied the behaviour of a pendulum, and one of the results was the discovery of the relationship between the frequency of vibration and the length of a pendulum. This, and many other results of his research were described in *Discourses Concerning Two New Sciences*, published in 1638. In 1667, after many experiments concerning sound transmission through a taunt wire, and the relationship between the frequency and pitch of a vibrating string, Robert Hooke invented tin can telephone. In 1686 sir Issac Newton published *Philosophiae Naturalis Principia Mathematica*, which includes, e.g., the three laws of motion. The second law is the basis to derive the equations of motion describing a vibrating body. Many other discoveries related to sound and vibration were made over the following decades [1].

Nowadays, a vibratory system is considered as mass — related with its kinetic energy, spring — related with its potential energy, and damper — related with the gradual loss of energy by the system [1]. Vibration can be defined as periodic movements of a mechanical system about its equilibrium position, that begins, when a mass is displaced from its balance state due to an impact of energy from an external source. A force generated in a potential energy element restores the mass into its equilibrium [2]. Vibrations can be classified in many ways. In literature, the following division

is commonly used [1]:

- Free vibrations without damping — the system is displaced from its equilibrium by initial force and then freely oscillates to return to the balance state.
- Free vibrations with damping — during the oscillations the system lost energy due to the friction or other sources of mechanical resistance.
- Forced vibrations — the external time-varying force impacts on the mechanical system, causing its oscillations. If the frequency of the disturbance covers with the natural frequencies of the system, a resonance phenomenon occurs.

Vibration is a phenomenon that is commonly used in everyday technology. An example can be musical instruments based on mechanical vibration, electric resonant circuits, or acoustic vibration, produced by the movement of a loudspeaker membrane. However, the vibrations can be also undesirable because in many cases they can cause discomfort and even may have negative impact on humans health. Such situations are common in mechanical vehicles, as well as in household appliances or industrial machinery. To avoid negative impact of the vibration on the users of machines and devices, many types of tests are performed during the manufacturing or diagnosis process. Usually, such tests are an analysis of the response of the system on vibration excited by an external force coming from, e.g., shakers or loudspeakers generating a specific type of signal. The different types of excitation signals can be used, e.g., random, sine, or impulse [3]. Usually, for acquisition of the response signal laser-Doppler vibrometer (LDV), accelerometers, microphones, or acoustic cameras are used. As the result of the tests many types of response of the system can be obtained and presented in different forms, e.g., plots of frequency or time-frequency functions, plots of modeshapes corresponding to natural frequencies, or recordings of undesired sounds emmited during the vibration. After the analysis the data can be used to improve vibration isolation, or for design and employment of the vibration damping system using one of the methods: passive, semi-active, or active.

1.2 Passive methods

The main assumption of the passive approach in vibration reduction is the inability to supply the system with the energy coming from an external source. It can be done in two ways: by the use of an additional layer of material with damping properties or

by the use of an element, that does not requires energy to work. The most popular solutions are shock absorbers, sandwich structures, and vibration isolators.

A shock absorber is the element that dampens impulses coming from shock excitation. The absorbed energy is usually converted to heat and then dissipated. Typically, these elements combined with a spring constitute passive suspension in the vehicles. The passive suspension has a single stiff and damping characteristics, that are tuned for specific vehicles and the conditions for which it was designed. For instance, for more comfortable driving experiences, a smooth dampers work is more preferred than the stability and control. Thus, the suspension characteristic will be more soft, oppositely to the sports cars, designed for higher velocities and more dynamic driving. Usually, the characteristic of the suspension is a compromise between these two aspects [4].

Sandwich structure is a composite material consists of at least three layers: two external, called face sheets, and one internal, called a core. The face sheets should provide bending rigidity to the construction, simultaneously with being thin comparatively to the core. The material and geometry selection for the core depends mainly on the preferred application of the sandwich. The core's structure is designed to stabilize the face sheets from wrinkling and buckling, and to support whole sandwich structure, similarly to an I-beam [5]. Sandwich structures are widely used in civil engineering, aeronautics, ships and road vehicles.

A vibration isolator is the element mounted between the vibrating mass and source of the mechanical excitation for the reduction of the undesirable vibration trasmission to the isolated system. The element consists of stiffness and damping parts [1]. The vibration isolators are widely used in many systems and devices, such as: heating, ventilation, air conditioning (HVAC) systems, pumps, washing machines, motors and systems of building protection from earthquakes.

1.3 Semi-active methods

In the semi-active case, supplying the system using an energy from the external source is acceptable only to change of properties of the structure, e.g., its stiffness. The employment of semi-active methods allows for switching between different damping characteristics for higher flexibility in the reduction of the vibration. Semi-active systems can be considered as a passive system with the infinite number of damping characteristics. The most popular solutions are magnetostrictive materials, and MR and electrorheological (ER) fluids.

Magnetostrictive material can convert energy from magnetic to kinetic, in both directions. Thus, when the material is magnetized it strains, and under the mechanical force it changes its magnetic state. Due to this property this material can be used as both sensor and actuator [6]. Magnetostriction in materials is an inherent property of ferromagnetism, hence, it does not degrade over time [7]. Magnetostrictive materials are used in various applications, such as: motors, actuators, and torque sensors [8].

MR fluid is a kind of smart fluid including micron-sized magnetized particles. By applying a magnetic field to MR fluid, magnetic moments are given to the particles, increasing apparent viscosity of fluid. The magnetized particles attract each other, becoming together a viscoelastic solid. The yield stress of MR fluid can be precisely adjusted by control of the intensity of the magnetic field [9]. MR fluids are widely used, mainly as MR dampers, in automotive, military, and aerospace industries.

ER fluid is a kind of smart fluid, similar to MR fluid with viscosity changed by applying of an external electric field, instead of a magnetic field [10]. However, MR fluids are more advantageous over ER fluids in some aspects, i.e., yield stress is 20-50 times stronger, these fluids are also more robust to moisture, and the required power and voltage are smaller in comparison to ER fluids [11]. ER fluids are used in various applications, often related to the automotive industry, such as: shock absorbers, hydraulic valves, clutches, and brakes.

1.4 Active methods

Active methods are based on the supply of the system with energy coming from the external source. In such an approach, the sets of sensors and actuators are integrated with a control algorithm by a feedback loop. The main advantages over passive and semi-active methods are the higher efficiency, and adaptability to changing conditions [12]. The following examples can be distinguished as the popular actuators used in active methods: voice coils, electromagnetic inertial actuators, and hydraulic/pneumatic/hybrid actuators.

Voice coil is an electromagnetic actuator, that can generate precisely controllable force. It can withstand accelerations more than 20-times higher than gravitational acceleration. Moreover, voice coil is also characterized by its high accuracy of positioning, and low time required to come back to its balance state after the high-acceleration move. These elements are applied in many solutions based on the active vibration damping, e.g., in disc drives, laser-cutting machines, medical equipment, or shaker

tables [13].

The electromagnetic inertial actuator is the kind of element, which is based on the voice coil. The coil remains static and is integrated with the outer part of the actuator, attached to the vibrating structure. The coil provides the sinusoidal control current with the set frequency. The mass with permanent magnets moves freely inside the coil [14]. These elements are used mainly in transportation, where they are mounted on airplane fuselages or under boat engines.

The hydraulic/pneumatic/hybrid actuator is the element, which converts the pressure of medium, i.e., fluid, air, or both, depending on the kind of actuator, into the mechanical force. The value of force is based on the value of control signal: voltage or current. These actuators are widely used in the industry, mainly as the element of motion or clamping systems, e.g., in valves. Moreover, it is also a part of the active suspension systems in various type of land vehicles.

1.5 Smart materials

The smart materials are the group of materials, that can change its properties, e.g., stiffness, shape or color in response to different factors or environmental conditions, e.g., temperature, stress, electric or magnetic fields [15]. Smart materials can also be a part (but not necessarily) of smart systems, that can function similarly to smart materials [16]. Smart materials are widely used in many industries, such as: automotive, aerospace, civil engineering, medicine, and transportation [7]. Many groups of smart materials can be distinguished. However, taking into account only elements related to vibration damping, these are previously mentioned: magnetostrictive materials, and smart fluids, i.e., MR and ER fluids. Moreover, the other materials can also be distinguished: piezoelectric elements, shape-memory alloys (SMA), and dielectric elastomers (DE).

Piezoelectric element is based on the piezoelectric effect, what can be explained as a linear interaction between electrical and mechanical quantities taking place in piezoelectric material. A mechanical deformation of this material under external force is related to the changes of electric polarization in the electrodes covering the material. Thus, the element can be used in the measurement of voltage generated under mechanical deformation. Additionally, the electrical charge stored in internal capacitance of the piezoelectric element can be used in the opposite way: to generate mechanical force. The piezoelectric elements are widely used in many industries and medicine [17].

Moreover, these elements can be used in all cases: passive, semi-active, and active, dependent on the application.

SMA is the material that has two unusual properties: shape-memory effect (SME) and superelasticity (SE). The material with SME can be deformed at a low temperature and return to its original shape after heating. SE is a property that allows to withstand large strains, without permament deformation [18]. SMAs are widely used in the aerospace industry for the vibration damping of engines mounted in commercial jets and launch vehicles. SMAs are also applied in automotive, medicine, and robotics.

DE is the element that transforms electrical charge into mechanical force, generating the large strains. It is a kind of capacitor, that consists of elastomer film enclosed by electrodes on both sides. This construction resembles sandwich structure. Many different types of the actuators can be distinguished depending on the shape and application, e.g., framed, cylindrical, stack, bending, thickness mode [19]. DE are used as actuators, e.g., in robotic artificial muscles, pumps, rotary motors, smart skins, and deformable surfaces in aerospace and optics [20].

1.6 Motivation for the research

Vibration is a phenomenon that is commonly used in everyday technology. The most common examples are musical instruments based on mechanical vibration, electric resonant circuits, or acoustic vibration, produced by the movement of a loudspeaker membrane. However, the vibrations are often eliminated because in many cases they can cause discomfort and even have a negative impact on human health. As examples, vibration in mechanical vehicles, as well as vibration in household appliances or industrial machines can be mentioned.

In these cases, active methods are the most effective solution in the context of vibration reduction. However, due to the high cost of their implementation, and above all energy consumption, they cannot be widely used. For this reason, the research presented in this dissertation is mainly based on the semi-active methods. Despite the limited efficiency in the case of non-stationary vibration, they are still an alternative for active methods, due to low energy demand. Progressive miniaturization and reduction of the production costs of smart materials, increases the probability of transferring the applied solutions to mass production.

Noise and vibration are investigated in the Department of Measurements and Control Systems at the Silesian University of Technology for 25 years [21, 22]. Developed

solutions and conducted research made this group and scientists belonging to it well recognized in this field, both in Poland and in the world.

1.7 Objective and thesis

The objective of this dissertation is to validate the possibility of successful use and performance of actuators based on smart materials for the reduction of vibrations of a vehicle suspension and a device casing, which are examples of a wide group of applications.

The following thesis is formulated: **It is possible to effectively reduce vibrations of mechanical structures by using smart materials, based on electrical or electromagnetic induction phenomena, to control the stiffness of the structure in selected areas or damping of vibrations in selected points of the structure**.

1.8 Contents

The dissertation consists of six chapters. Each of them is divided into sections corresponding to the problems described in the introduction, at the beginning of each chapter.

In Chapter 1 the general information about vibration reduction and smart materials is presented, including literature study related to the scope of this dissertation.

In Chapter 2 the list of elements of laboratory equipment with main parameters is presented. Moreover, each of the systems investigated in the experiments, i.e., device casing and all-terrain vehicle (ATV), is also briefly described. This chapter also includes the description of the process of the design and optimization of microphone array, and construction of the acoustic camera based on it.

Chapter 3 concerns the device casing with a single panel as a front wall. Two different plates were investigated: isotropic steel and orthotropic aluminum. A brief introduction is included in the first section. In the second section, mathematical models of the plates are presented and described. The information included in this section was necessary to obtain the modeshapes and corresponding resonant frequencies for both the panels. The third section contains literature study on the piezoelectric shunt damping (PSDa) systems. One of the PSDa examples is described in the fourth section with more details from the practical side. It includes also experimental results for both

the panels with five and nine piezoelectric elements, respectively. The fifth section contains an investigation of the influence of type and material of walls covering the device casing on frequency response of the front panel. In the next section a new electromagnetic coupling element is preliminarily tested. In the last section results presented in this chapter are discussed.

In Chapter 4 the device casing with a double-panel structure as a front wall is considered. The first section contains a brief literature study on the research based on this structure. The second section introduces a new type of electromagnetic coupling element with the most important information about principle of work and its properties. The experimental results for the single and five coupling elements are also presented. In the next section, the modified Chladni's method for visualization of the modeshapes of vibrating structure is considered. Besides the description of such an approach, the experimental results are also presented for semi-active electromagnetic couplings, as well as passive magnetic couplings. The last section summarizes the research described in the whole chapter.

Chapter 5 contains the theoretical and experimental analysis of the ATV. In the first section the vehicle suspension is shortly discussed. In the second section a mathematical model of the suspension based on MR dampers is described. The information included in this section is used for the implementation of algorithm for vibration attenuation, executed in the next section. The fourth section contains a more precise approach in the estimation of suspension velocity for more efficient attenuation of the road inducted vibration of the vehicle. The last section summarize s the considerations included in this chapter.

Chapter 6 is a summary of this dissertation, and presents the main conclusions drawn from the performed experiments. It also contains the author's contribution and discusses further research.

Chapter 2

Laboratory equipment

2.1 Background

The performed research consists of three main parts: *device casing with a single panel*, *device casing with a double-panel structure*, and *magnetorheological vehicle suspension*. Each of them concerns methods for structural vibration attenuation.

The first two parts are based on the *rigid frame device casing* (see Section 2.2), designed for easier reconfiguration of the structure of a top and side walls. It allows for consideration of different experimental scenarios: fully or partially closed casing with a single panel, or double-panel structure as a front wall. It is also possible to analyse different mediums and mechanical couplings between the panels.

The third part is based on the *All-terrain vehicle with semi-active suspension* (see Section 2.3), which is a quad vehicle, equipped with modified suspension. The manufacturer's dampers were replaced by the MR dampers. With this modification it is possible to change characteristics of the suspension, depending on road-inducted excitation.

In this Chapter each of the laboratory stands is described, with technical details. Furthermore, measurement and control systems used in these experiments, including sensors and actuators, are presented.

2.2 Rigid frame device casing

2.2.1 Description of system

The casing described in this Section is presented in Fig. 2.1. The schemes include all important dimensions, oblique section of rigid frame, and different mounting config-

urations of a panel: with and without additional, square clamping frame. The main part of the casing is a rigid, cubical frame welded from 3 mm thick steel profiles [23]. The bottom part of the casing stands on the 60 mm thick plywood platform with rubber wheels to minimize vibration propagation to the laboratory floor. Moreover, the interior of the casing can be additionally filled by a 40 mm thick layer of acoustic foam, placed in the space between panels (Fig. 2.2). This solution improves the acoustic insulation of the top, bottom and side walls, except investigated a single panel or double-panel structure. Each side of the rigid frame, except the bottom, has twenty screws, embedded on the inner and outer part of the casing, for panel mounting. With the 10 mm length screws it is possible to use panels of different thicknesses. Furthermore, the panels can be also clamped by an additional square frame (Fig. 2.1(d)) to provide boundary conditions closer as much as it is possible to be fully clamped.

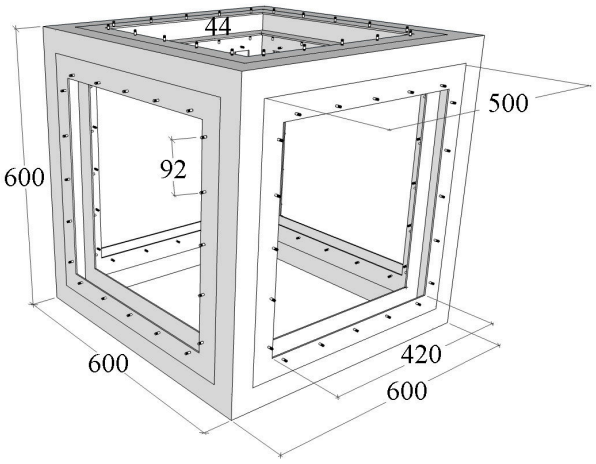

(a) View of opened casing with dimensions.

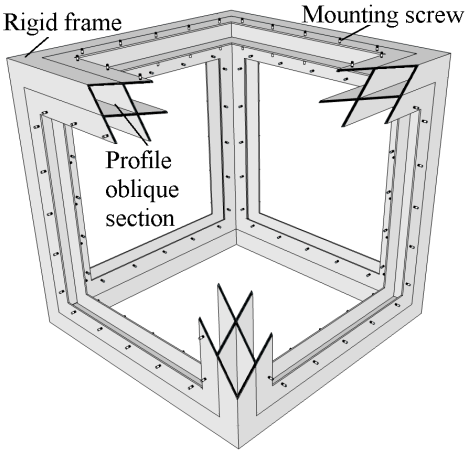

(b) View of oblique casing section.

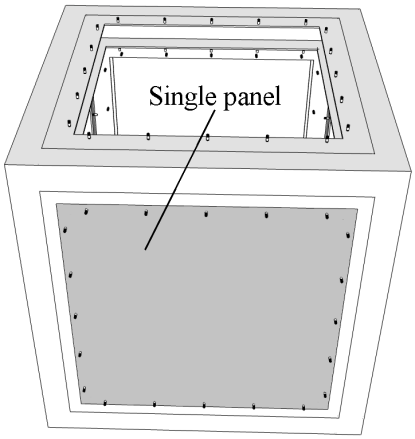

(c) View of rigid frame with a single panel.

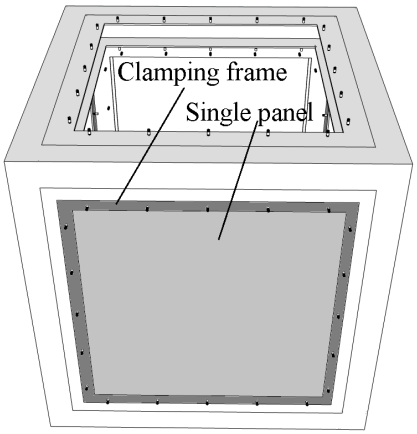

(d) View of rigid frame with a single panel with clamping frame.

Figure 2.1: Schemes of described rigid frame. The dimensions are given in mm.

Figure 2.2: Interior of the casing covered by a layer of acoustic foam.

2.2.2 Casing walls

During the experiments a 0.5 mm, 0.6 mm thick steel isotropic and 1.0 mm thick aluminum orthotropic panels are used, as the front wall of a rigid frame casing. A single panels are used or combined into a double-panel structure.

The experiments for a rigid frame casing with a single panel are performed for frequencies, selected from the first fifteen modes for steel (Fig. 2.3) and aluminum panels (Fig. 2.4). The choice depends on type and placement of the structure, and the experimental scenario. The modeshapes are obtained using models implemented in FreeFEM software. The models of both steel and aluminum panels are included and described in Section 3.2. For a single panel it is assumed that boundary contidions are fully clamped, and the thicknesses are 0.5 mm for the steel panel and 1.0 mm for the aluminum panel. The main parameters of panels are presented in Table 2.1.

Table 2.1: Main parameters of panels.

Parameter	**Value, unit (steel)**	**Value, unit (aluminum)**
Dimensions	420 × 420 × 0.5 mm	420 × 420 × 1.0 mm
Mass	0.69 kg	0.47 kg
Density	7850 kg/m^3	2680 kg/m^3
Young modulus	200 GPa	70.50 GPa
Poisson ratio	0.30	0.33

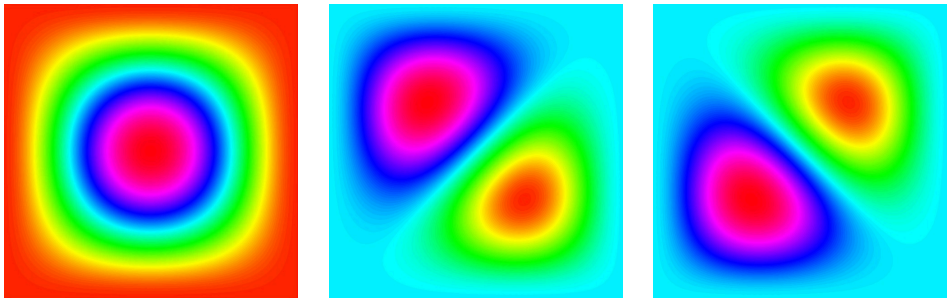
Mode 1, 24.96 Hz.

Mode 2, 50.75 Hz.

Mode 3, 50.76 Hz.

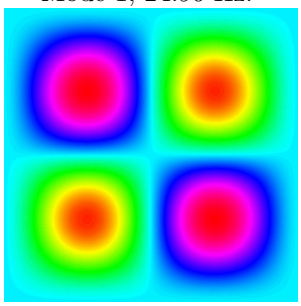
Mode 4, 74.72 Hz.

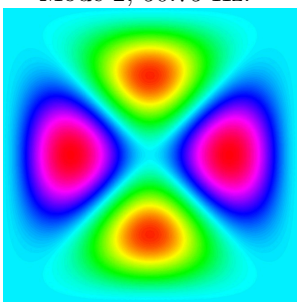
Mode 5, 90.60 Hz.

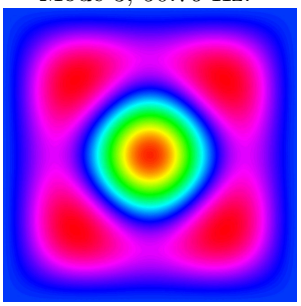
Mode 6, 91.04 Hz.

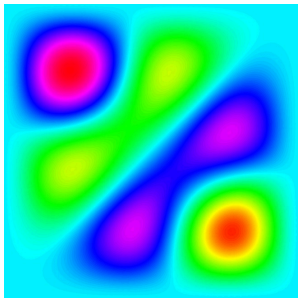
Mode 7, 113.50 Hz.

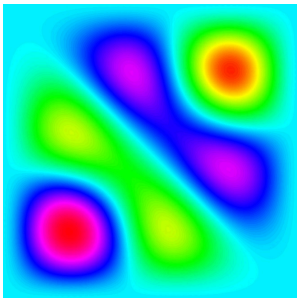
Mode 8, 113.57 Hz.

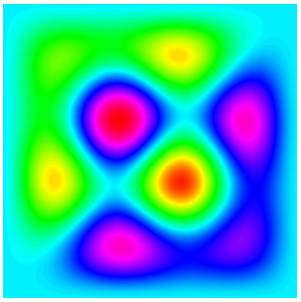
Mode 9, 144.17 Hz.

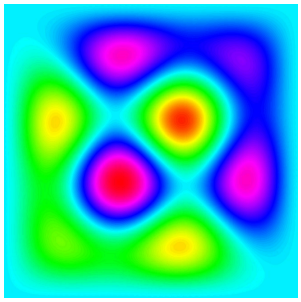
Mode 10, 144.18 Hz.

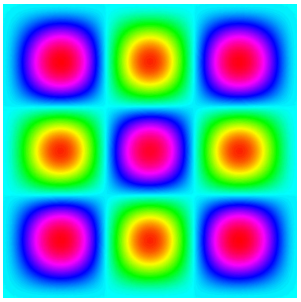
Mode 11, 151.07 Hz.

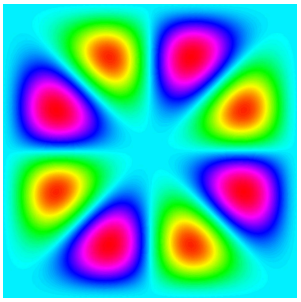
Mode 12, 165.79 Hz.

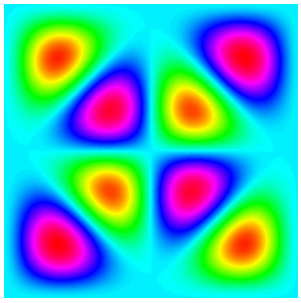
Mode 13, 166.51 Hz.

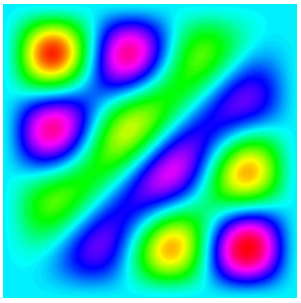
Mode 14, 202.53 Hz.

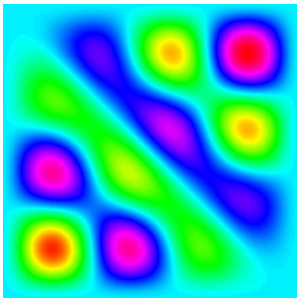
Mode 15, 202.78 Hz.

Figure 2.3: Simulation results for the first fifteen modeshapes of the isotropic, 0.5 mm thick, steel, single panel used in experiments.

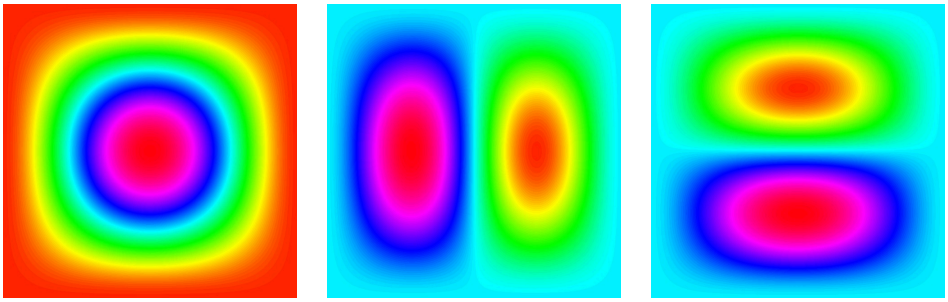
Mode 1, 51.28 Hz. Mode 2, 103.52 Hz. Mode 3, 105.20 Hz.

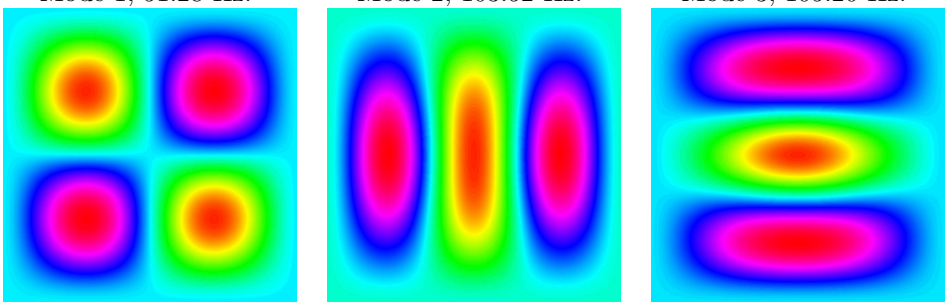
Mode 4, 153.86 Hz. Mode 5, 184.84 Hz. Mode 6, 188.94 Hz.

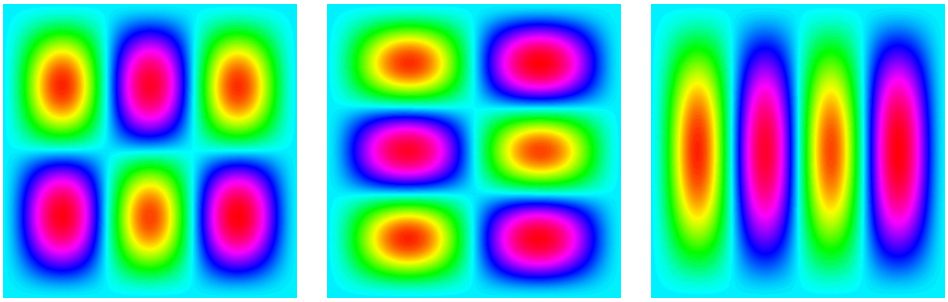
Mode 7, 232.78 Hz. Mode 8, 235.20 Hz. Mode 9, 293.61 Hz.

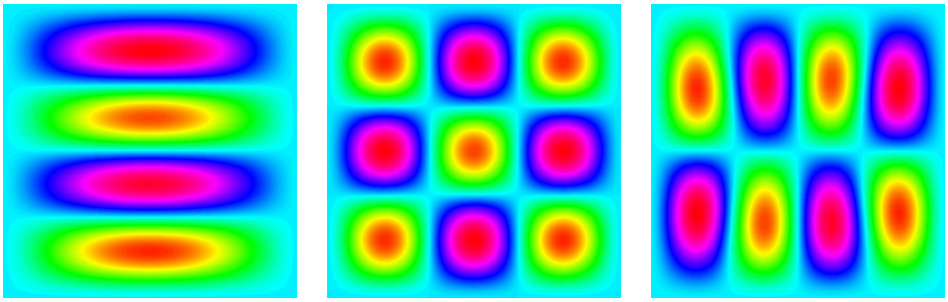
Mode 10, 300.58 Hz. Mode 11, 311.69 Hz. Mode 12, 339.93 Hz.

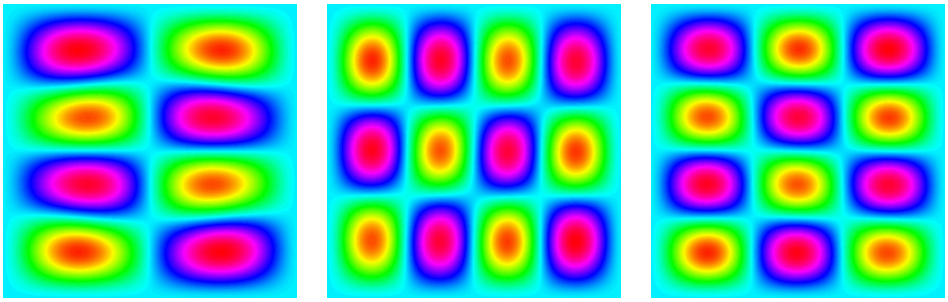
Mode 13, 345.61 Hz. Mode 14, 417.00 Hz. Mode 15, 420.14 Hz.

Figure 2.4: Simulation results for the first fifteen modeshapes of the orthotropic, 1.0 mm thick, aluminum, single panel used in experiments.

For a double-panel structure the boundary conditions are the same, the thickness of the inner (incident) panel is 0.6 mm, the thickness of the outer (radiating) panel is 0.5 mm, and the panels are separated by a 50 mm cavity gap. Both the panels are made from steel and their thicknesses in a double-panel structure are different, to avoid coincidence effect, when the coupled panels move in phase, at the same resonant frequency [24]. However, the modeling of a double-panel structure is a more complex issue [25], thus, its modeshapes and resonant frequencies are not further theoretically investigated. The other, top and side walls are usually a 3 mm thick aluminum (Fig. 2.5(c)) or a 4 mm thick plywood panels with additional bitumen layer (Fig. 2.5(d)), depending on the type of experiment. However, in the Section 3.3 an empty frame (Fig. 2.5(a)) and foam layers (Fig. 2.5(b)) are also examinated.

(a) Frame without top and side walls.

(b) Foam layers.

(c) Aluminum panels.

(d) Plywood panels.

Figure 2.5: Panels used in the experiments.

2.2.3 Measurement and control system

The experiments were performed according to different scenarios, with the use of a variety of laboratory equipment. The most important elements of measurement and control system are presented in Figure 2.6 with the main parameters, listed in tables. Depending on the experiment, the following equipment was used:

- NI PCI-6289 with SCB-68A connecting panel — for data acquisition from macro fiber composite (MFC) elements, microphones and LDV, and generation of excitation signal.
- NI myRIO-1900 embedded system — for generation of excitation signal and control of electromagnetic couplings.
- dSpace DS1104 card with CLP1104 connecting panel — for data acquisition from microphones and LDV.
- Meter International Corp. FG 503 — for generation of excitation signal.
- Behringer B208D BK active loudspeaker — for excitation the investigated structures to vibration.
- HW-517 modules — for control of electromagnetic couplings.
- JF-0530B modified push-pull solenoids — for coupling of plates in a double-panel structure.
- Smart Material M8514-P2 MFCs — for vibration damping in shunt circuits and measurement of panel's vibration.
- Polytec PDV100 LDV — for measurement of investigated structure vibration.
- Beyerdynamic MM-1 microphones — for measurement of noise generated by source enclosed inside the investigated rigid frame casing.
- ThermoPro TP8 IR camera — to acquire the infrared (IR) images of modeshapes in modified Chladni's method for modal analysis of vibrating structure.
- Basler acA1280-60gc vision camera — to acquire vision images of modeshapes in modified Chladni's method for modal analysis of vibrating structure.

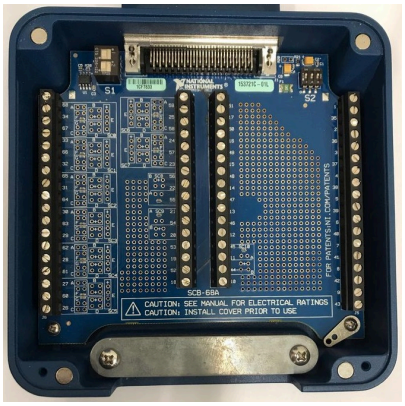

Parameter	Value, unit
AI sample rate	500 kS/s
AI resolution	18 bits
AI voltage range	0.1–10 V
AO update rate	1.25 MS/s
AO resolution	16 bits
AO current drive	5 mA

(a) NI PCI-6289 card with SCB-68A connecting panel.

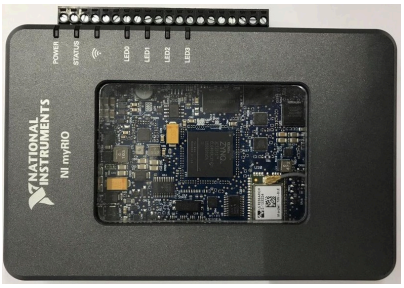

Parameter	Value, unit
AO update rate	345 kS/s
AO resolution	12 bits
AO current drive	2 mA
DO logic	3.3 V
Maximal PWM frequency	100 kHz

(b) NI myRIO-1900 device.

Parameter	Value, unit
AI sample rate	500 kS/s
AI resolution	12 bits
AI voltage range	±10 V

(c) dSpace DS1104 card with CLP1104 connecting panel.

Parameter	Value, unit
Frequency range	10 mHz–3 MHz
Resolution	10 mHz
Harmonic distortions	-60 dB

(d) Meter International Corp. FG 503 generator.

Parameter	Value, unit
Frequency range	65 Hz–20 kHz
RMS Power	170 W
Maximal SPL	113 dB

(e) Behringer B208D BK active loudspeaker.

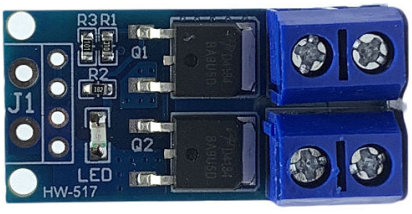

Parameter	Value, unit
Operation voltage	5–36 V
Maximal current	15 A
PWM frequency	0–20 kHz

(f) HW-517 modules.

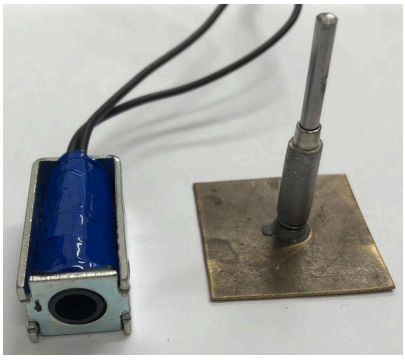

Parameter	Value, unit
Operating voltage	6 V
Operating current	0.3 A
Maximal force	5 N
Maximal voltage	12 V
Maximal current	1.5 A
Maximal stroke	10 mm

(g) JF-0530B modified push-pull solenoids.

Parameter	Value, unit
Young's modulus	30.3/15.8 GPa
Poisson's ratio	0.31

(h) Smart Material M8514-P2 MFCs.

Parameter	Value, unit
Frequency range	0.5 Hz–22 kHz
Resolution	< 0.02 μm·s^{-1}

(i) Polytec PDV100 LDV.

Parameter	Value, unit
Frequency range	20 Hz–20 kHz
SNR	$>$ 57 dB
Max. SPL	$>$ 122 dB

(j) Beyerdynamic MM-1 microphones.

Parameter	Value, unit
Resolution	384×288 px
Temperature range	-20–800 °C
Accuracy	±1 °C

(k) ThermoPro TP8 IR camera.

Parameter	Value, unit
Resolution	1280×1024 px
Frame rate	60 fps
Pixel bit depth	12 bits

(l) Basler acA1280-60gc vision camera.

Figure 2.6: Equipment used in main experiments on rigid frame casing, with selected parameters listed in tables.

2.3 All-terrain vehicle with semi-active suspension

2.3.1 Description of system

The ATV described in this Section is type CF-Moto-500, presented in Fig. 2.7. A scheme includes all of the important parts of the vibration attenuation system. The main technical data of the experimental vehicle is presented in Table 2.2 [26]. The manufacturer's dampers were replaced by the MR dampers — type Lord RD-8041-1 with short and long stroke for front and rear parts of the vehicle, respectively.

Figure 2.7: Investigated ATV.

Table 2.2: Main technical data of investigated ATV.

Parameter	Value, unit
Front wheel travel	0.17m
Rear wheel travel	0.23 m
Weight	357 kg (with oil and full fuel tank)
Wheelbase	1.29 m
Overall height	0.90 m
Overall width	1.17 m
Overall length	2.32 m

2.3.2 MR dampers

MR dampers are classified as intelligent structures. They consist of MR fluid, with viscosity dependant on the provided current and, in consequence, on magnetic field. The MR fluids consist of micro-size magnetically polarizable particles dispersed in a non-magnetic carrier medium, e.g. mineral or silicone oil. The behaviour of fluid can be changed from plastic to semisolid with a frequency up to 100 Hz [27].

Typically, MR damper consits of a cylinder filled with MR fluid, piston with magnetic coils, and gas chamber (Fig. 2.8). When the piston rod moves forward inside the cylinder, the MR fluid flows from the gas chamber, through the piston gaps. After supplying current to the damper, the magnetic field is generated, thanks to the phenomenon of electromagnetic induction, and MR fluid particles are polarized. In consequence, they are combined into the chain-like structures, perpendicularly to the direction of fluid flow, along the magnetic field lines [28].

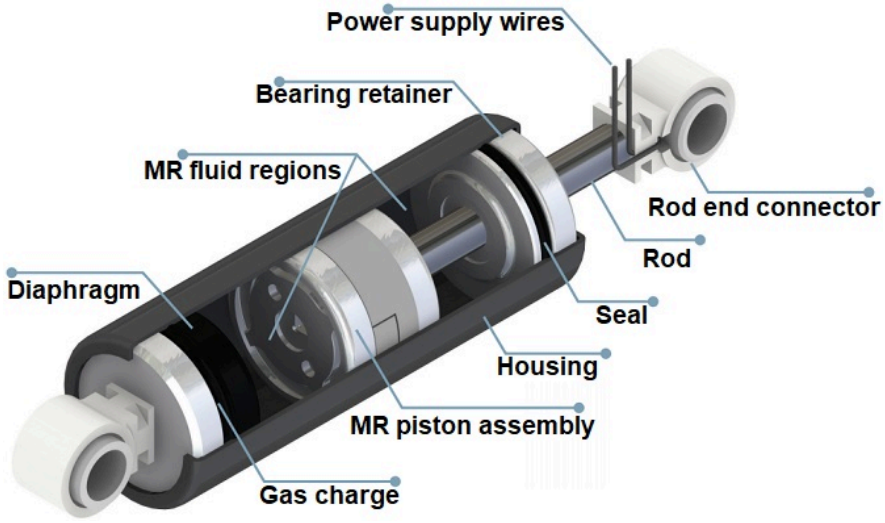

Figure 2.8: Construction of MR damper, *Credits: https://www.lord.com/products-and-solutions/active-vibration-control/industrial-suspension-systems/how-does-mr-damper-work, access: 20.01.2022.*

2.3.3 Measurement and control system

The experiments were performed with a variety of laboratory equipment mounted on the investigated ATV. The most important elements of measurement and control system are presented in Figure 2.9 with the main parameters, listed in tables. The exceptions are the custom made peripheral microcontroller units (MCU) for data acquisition from accelerometers mounted on sprung and unsprung masses, and control of MR

dampers. The other equipment was:

- Freescale Sabre Lite — the central unit of measurement and control system, for data processing, and communication with NI sbRIO and MCU.
- NI sbRIO-9636 — for data acquisition from accelerometers for driver's comfort measurement, Hall sensors and inertial measurement unit (IMU).
- Peltron WG09-x4 LVDT signal conditioner — the unit to provide a power supply to the LVDT sensors and conversion measurement to voltage.
- Peltron PTx LVDT sensors — LVDT for direct measurement of MR dampers sprungs deflection.
- Sparkfun MMA8452Q accelerometers — sensors for measurement of suspension acceleration, mounted on sprung and unsprung masses of experimental ATV.
- Lord Corporation RD-8041-1 MR dampers — MR dampers for semi-active vibration attenuation on investigated ATV.
- Waveshare AH49E Hall sensors — for measurement of the rotational speed of a vehicle's wheels.
- Xsens MTi IMU — sensor for measurement of the vehicle rotation, and acceleration affecting the driver.

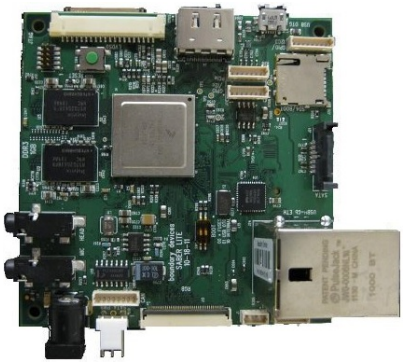

Parameter	Value, unit
Processor	Quad-Core 1 GHz
Memory	1 GB DDR3
Interfaces	CAN, I2C, GPIO

(a) Freescale Sabre Lite.

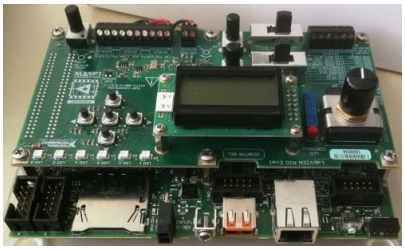

Parameter	Value, unit
AI range	500 kS/s
AI resolution	16 bits
AI range	±10 V
DO logic	3.3 V

(b) NI sbRIO-9636 embedded system.

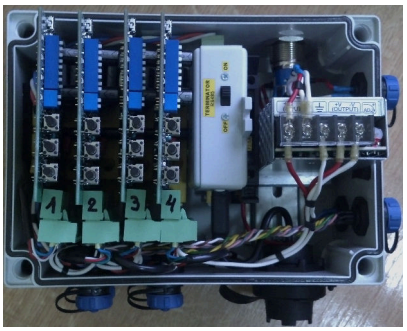

Parameter	Value, unit
AI sample rate	250 S/s
AI voltage range	0–10 V
Operating voltage	10.5–18 V
Measurement error	> 50 mV
Resolution	12 bits

(c) Peltron WG09-x4 LVDT signal conditioner.

Parameter	Value, unit
Output voltage range	0–10 V
Operating voltage	12 V

(d) Peltron PTx LVDT sensors.

Parameter	Value, unit
Acceleration range	±8 g
Resolution	12 bits
Operating voltage	1.95–3.6 V

(e) Sparkfun MMA8452Q accelerometers.

Parameter	Value, unit
Operating voltage	12 V
Maximal current	2 A
Damping force	> 2447 N

(f) Lord Corporation RD-8041-1 MR dampers.

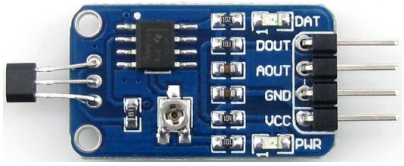

Parameter	Value, unit
Operating voltage	2.3–5.3 V
Output type	Digital

(g) Waveshare AH49E Hall sensors.

Parameter	Value, unit
Acceleration range	±5 g
Resolution	16 bits

(h) Xsens MTi IMU.

Figure 2.9: Equipment used in main experiments on ATV, with selected parameters.

2.4 Acoustic camera

2.4.1 Description of device

An acoustic camera is a device, widely used for localization of sound sources. It consists of two main parts: a vision camera — for vision image acquisition, and microphone array — for sound acquisition. Depending on the type of microphone array, it is possible to localize sound sources in one-, two-, or three-dimensional space. The signals from microphones are processed into the color map representing sound intensity, usually by the use of direction of arrival (DOA) algorithms, such as Bartlett, Capon, or Multiple signal classification (MUSIC) [29]. The color map is overlaid transparently on the image from vision camera, to obtain graphical representation of the sound sources positions. Acoustic cameras are often used in industry, as a tool for quality assurance. One of the widely described examples is buzz, squeak, rattle (BSR) localization of instrument panel in vehicles interior [30]. It is well known and important problem in product quality in automotive industry since many years. Usually, BSR are localized by

human auditors. However, such an approach has significant issues with reproducibility and repeatability of inspection results. Therefore, the solutions based on the acoustic cameras become more common [31]. Moreover, the acoustic camera can be used for vibration localization, based on the sound emission as a consequence of presence of phenomenons like friction. Lu et. al [32] described a fault diagnosis in bearings, using the gray level coocurrence matrix (GLCM) based extraction of features, corresponding to different vibration characteristics. The other example is localization of sources of chatter frequencies in gear cutter. The method was also validated using modal analysis, which proved the correspondence of both approaches. The first bending mode of stick blade was localized using an acoustic camera, and the vibration was reduced by suppressing the mechanical energy as heat [33].

2.4.2 Microphone array geometries

The first three microphone arrays, presented in Figure 2.10 were implemented (Fig. 2.11) and two of them were described in recent years [34, 35]. The microphones in grid array (Fig. 2.10(a)) were distributed, based on the general relations between frequency range, microphone spacing and array diameter [36]. The second investigated type of grid array was spiral (Fig. 2.10(b)), with logarithmical change of the spacing between microphones on each branch. It is known as Underbrink array — from the name of its inventor [37]. Two different sizes of the spiral array were investigated: 0.35 m — as the real, implemented prototype, and 0.6 m — as the simulated, resized version for comparison with pseudo-random array. The pseudo-random array (Fig. 2.10(c)) was designed similarly to the sector wheel arrays, described by Hald [38]. In this case, the first sector contains 12 microphones, distributed pseudo-randomly.

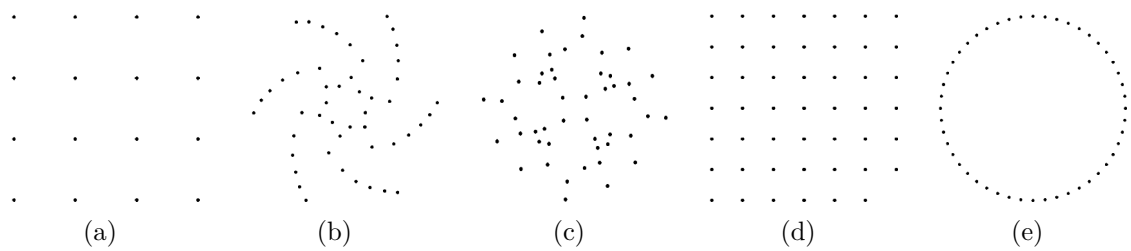

Figure 2.10: Compared microphone array geometries: (a) grid 1; (b) Underbrink 1, 2; (c) pseudo-random; (d) grid 2; (e) circular.

The main criterion was to obtain a minimal value of the average microphone spacing (AMS) (Eq. 2.1), with a simultaneous 0.66 m array diameter.

$$AMS = \frac{\sum_{i=1}^{N} \sqrt{{x_i}^2 + {y_i}^2}}{N}; \tag{2.1}$$

where N, x, y are number of microphones, and (x, y) values in a Cartesian coordinate system, respectively. The size of microphone array was adapted to dimensions of panels mounted on rigid casing (see Section 2.2.2). The main purpose of this microphone array geometry is to implement statistically optimised near-field acoustic holography (SONAH) [39] for modal analysis of investigated panels in rigid frame casing [40, 41]. Currently, the camera use only the MUSIC algorithm [42], provided as a dedicated LabVIEW library, developed by NGene company. Every other sector of microphone array is obtained by rotating the previous one by 90° angle.

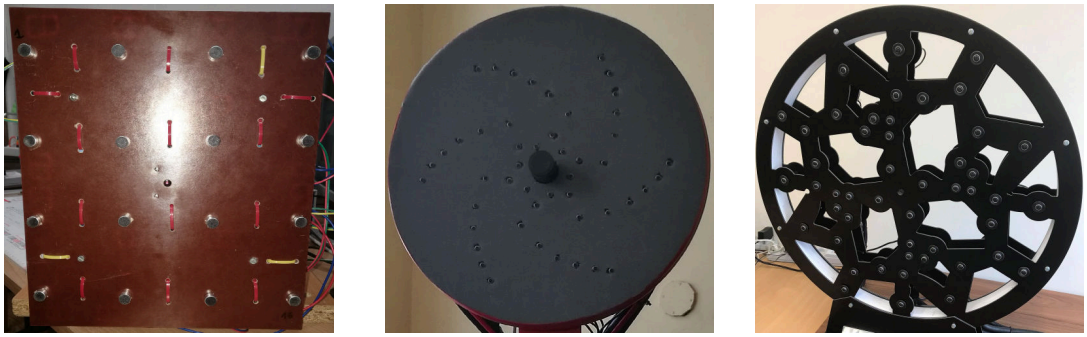

(a) (b) (c)

Figure 2.11: Prototypes of acoustic cameras: (a) grid (Fig. 2.10(a)); (b) Underbrink (Fig. 2.10(b)); (c) pseudo-random (Fig. 2.10(c)).

The main parameters of microphone array geometries are presented in Table 2.3. The first three are implemented prototypes, presented above, and other geometries are only the simulations included to compare the pseudo-random array with other shapes, redesigned to obtain the same diameter and number of microphones. Therefore, in the second, larger grid the microphone in the bottom-right corner has been removed to obtain 48 microphones (Fig. 2.10(d)).

Table 2.3: Main parameters of investigated array geometries.

	Grid 1	**Underbrink 1**	**P-random**	**Circular**	**Grid 2**	**Underbrink 2**
Diameter	0.21 m	0.35 m	0.66 m	0.66 m	0.66 m	0.66 m
Microphones	16	48	48	48	48	48
AMS	0.03 m	0.10 m	0.19 m	0.33 m	0.31 m	0.23 m

The investigated array geometries were simulated using the NGene library, dedicated for LabVIEW (Fig. 2.12). The first comparison was performed for four selected frequencies emitted by an artificial monopole sound source, radiating straight to the central point of array. The second comparison takes into account only the one frequency emmited by a single dipole source with an 60° angle between dipole legs. The amplitude is normalized, hence, the color map is rescaled to 0–1 range.

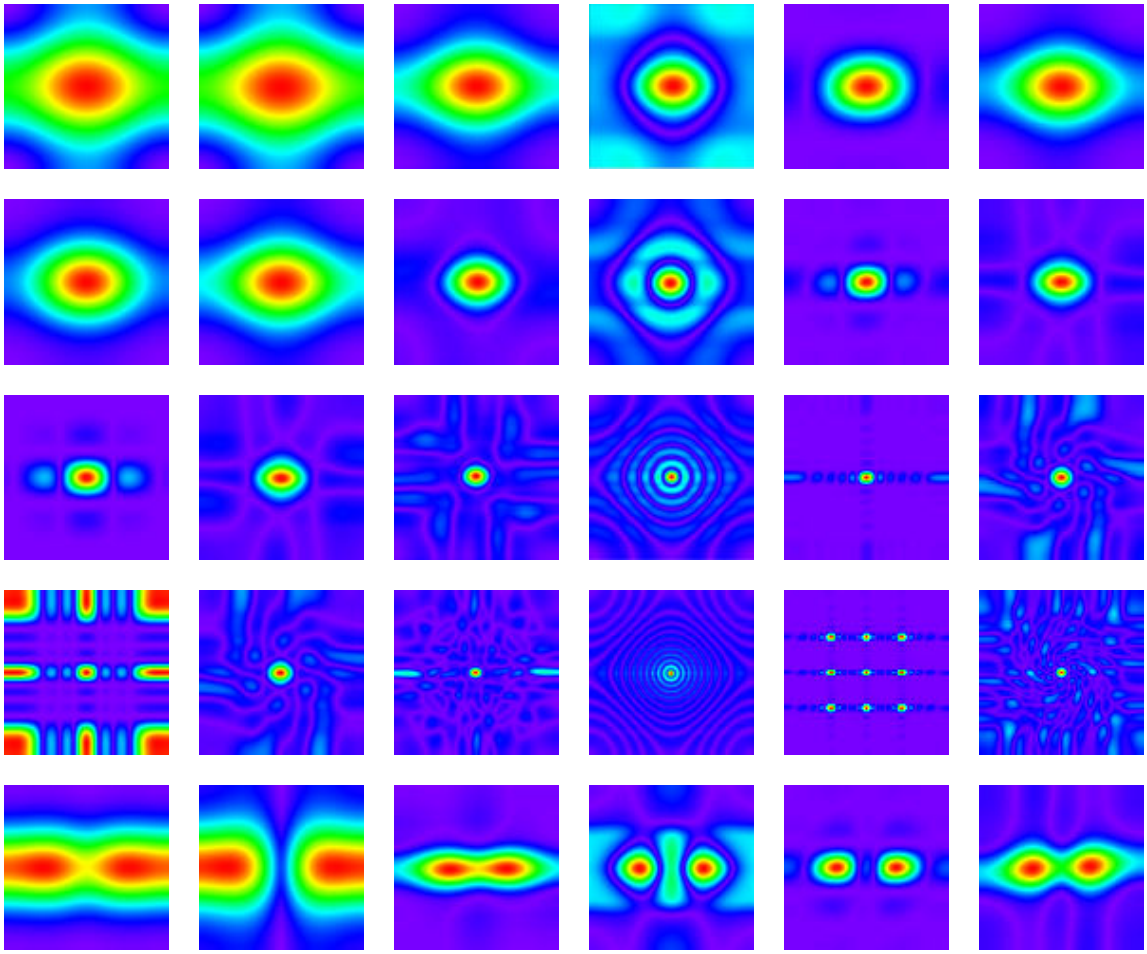

Figure 2.12: Normalized sound intensity maps for investigated arrays, the following rows correspond to sources: monopole 0.5 kHz; monopole 1 kHz; monopole 2.5 kHz; monopole 5 kHz; dipole 1 kHz.

The results for the pseudo-random array for 0.5 and 1 kHz monopole sources are slightly worse in comparison to the 0.66 m Underbrink array and to the 0.66 m grid array. However, the pseudo-random array efficiency increases for higher frequencies, where the side lobes are less visible in comparison to other geometries. For dipole source, the separation is visible, but incomplete, and worse in comparison to the 0.66 m Underbrink array, and in particular with the 0.66 m grid array.

2.4.3 Measurement system

The description of the measurement system concerns only the last prototype of acoustic camera — with pseudo-random microphone array (Fig. 2.11(c)). The system is divided into two main parts: vision and acoustic (Fig. 2.13). The first part is Basler acA1280-60gc camera, the same type as used in experiments described in Section 4.3. The acoustic part includes an array of analog electret microphones with built-in preamplifiers. The used microphones are high-quality Panasonic WM-61A, dedicated for measurements purposes. The main parameters are presented in Table 2.4.

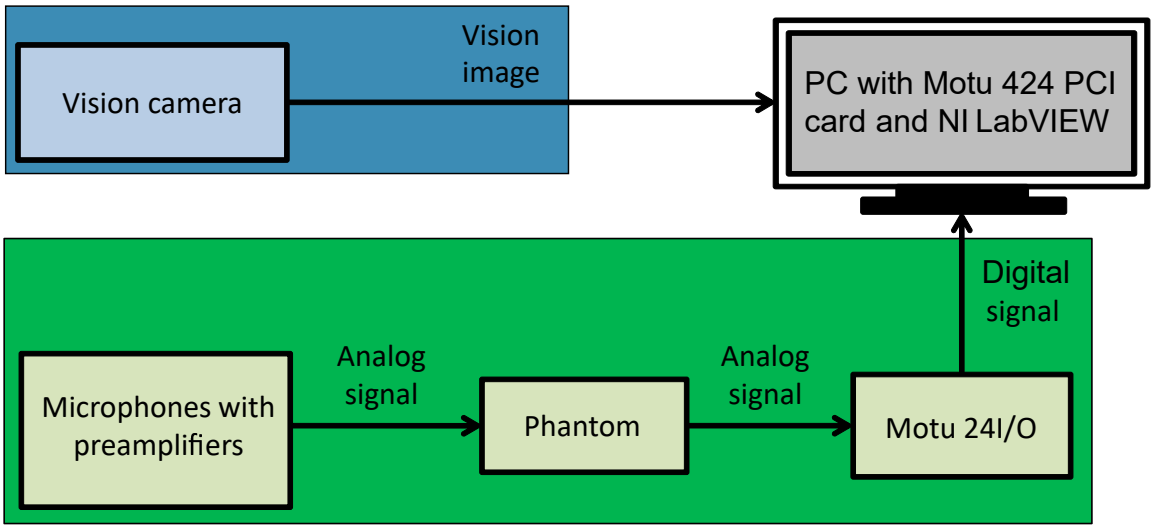

Figure 2.13: Scheme of measurement and control system for the acoustic camera.

The microphones are connected to the phantom unit supplying the preamplifiers and transmitting measurements to the Motu 24I/O digital to analog converter (DAC). After conversion the signals are transmitted to the Motu 424 PCI audiocard, and acquired in application, developed in the NI LabVIEW graphical environment.

Table 2.4: Main parameters of Panasonic WM-61A microphones.

Parameter	**Value, unit**
Sensitivity	-35±4 dB
Frequency range	20–20000 Hz
Max. operation voltage	10 V
Standard operation voltage	2 V
S/N ratio	> 62 dB

2.4.4 Preliminary validation

The prototype of the acoustic camera with pseudo-random microphone array (Fig. 2.11) was preliminarily validated with the use of different test objects, i.e.: hair dryer, fan, and small fans (Fig. 2.14).

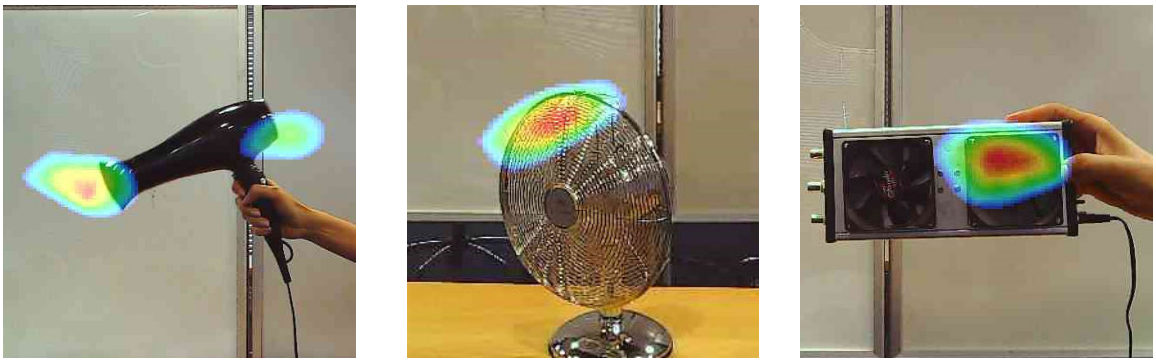

(a) (b) (c)

Figure 2.14: Test object for acoustic camera: (a) hair dryer; (b) fan; (c) small fans.

In Figures 2.15—2.17 a mean power spectral density (PSD) for all objects is presented. By mean PSD an averaged PSD of signals acquired by all of the microphones in array is meant. The amplitude of PSD is normalized to 1, because this information is further used in the acoustic map. The frequency bin is 18.5 Hz. Such a low resolution of the PSD plots is intentional. The frequency range of the noise emitted by the tested object was wide, hence, the decimation of the acquired data was possible. Such an approach allowed for localization of the non-stationary sources of the sound in real time, which will not be possible with the higher resolution for 48 channels simultaneously. The hair dryer (Fig. 2.15) emitted the sound in two ways: forward and rear. The dryer was also moved in different places, for simulation of the non-stationary source of the sound. The most significant frequency band was up to 3 kHz.

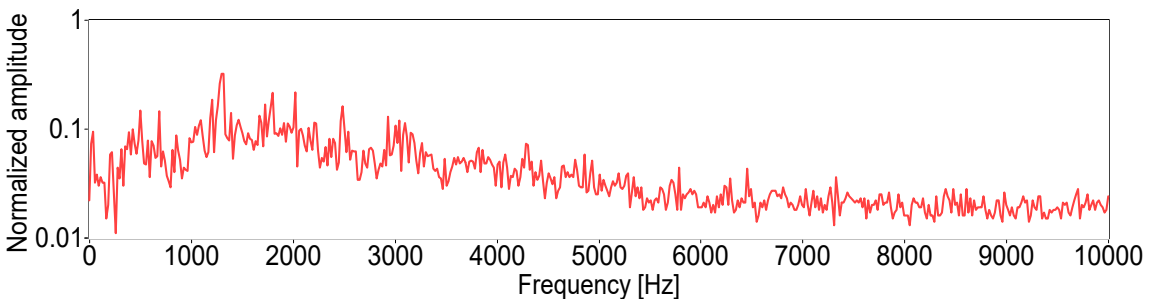

Figure 2.15: Mean PSD for hair dryer with amplitude normalized to 1.

The fan was a non-stationary source of sound, because the source was localized in different places, where rotating blades cut the air. Moreover, the fan was rotating around its vertical axis. Hence, the source of the sound was moving in two perpendicular planes. The most significant components of the PSD were observed up to 2 kHz.

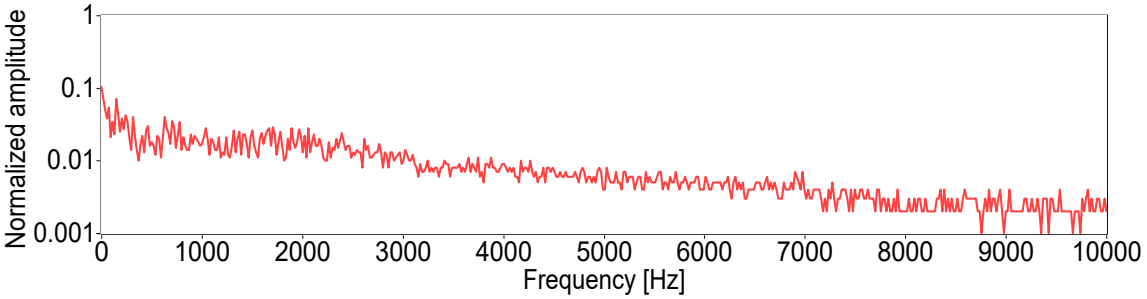

Figure 2.16: Mean PSD for fan with amplitude normalized to 1.

The small fans were mounted outside the aluminum casing. Only one fan was running at a time, and the active fan was selected with the use of a switch placed on the side of the casing. The object was a stationary source of sound except moments of switching between fans. The most significant frequency range was up to 2 kHz.

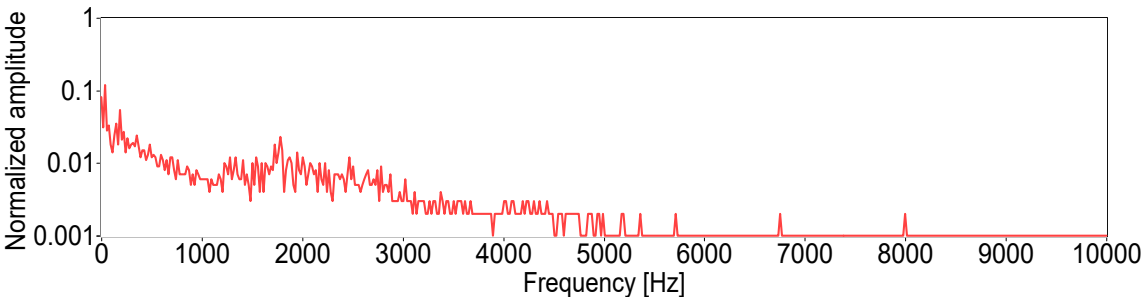

Figure 2.17: Mean PSD for small fans with amplitude normalized to 1.

It was proven, that the described device can localize both stationary and non-stationary sources of sound, in the mid-low frequency range, i.e., 3 kHz. The higher frequencies were not considered, because the acoustic camera was originally designed for the observation of lower frequencies, i.e., up to 500 Hz.

Chapter 3

Device casing with a single panel

3.1 Background

A single panel is the most popular solution for enclosing devices in order to protect them or isolate the environment against noise emitted by them. It is used e.g. in household appliances or in all types of machines and power tools. However, many of these casings still propagate noise or generate vibrations undesired for its users. Hence, many solutions were employed to reduce the negative effect of work of the machines and devices on human health or comfort. The most popular approaches are to modify the shape of the structure, attach the additional mass or stiffness [43] on its surface, or modify the material. The last idea can be implemented in numerous ways, e.g., by using sandwich structures [44], metastructures [45], or constrained layer damping (CLD) treatment [46]. Besides all the mentioned passive methods the semi-active shunt systems are also popular. It is mainly based on the piezoelectric elements [47], or electromagnetic transducers [48]. The last are active systems, e.g., actively tunable vibration absorbers (ATVA) [49], or electrodynamic exciters [50].

A single panel was investigated in the papers [51–53] with the author's contribution. All of the listed publications are focused on a single panel mounted on a rigid frame casing. The vibration was reduced using MFC elements in semi-active or active configurations. The first two papers are simulation and a passive implementation of a semi-active method of vibration reduction for the 11^{th} mode of an isotropic steel panel with five MFC elements. The last paper was a comparison between active method, and semi-active method implemented as passive, and semi-active circuits. The research is based on the orthotropic aluminum panel with nine MFC elements.

This Chapter presents the research included in [51–53] papers, with a brief descrip-

tion of the implemented circuits. The preliminary experiment with the new type of electromagnetic coupling is also presented, as well as the results of research on the influence of the type and material of the casing walls on the frequency response of a front panel.

3.2 Single panel modeling

In the research it was assumed that there are no mechanical interactions between the front and other walls. The modeling of the investigated object with all of the mechanical couplings would be much more complicated. The mathematical models of panels, used in further research, are based on the Kirchhoff-Love theory [54], which is a two-dimensional equivalent of the Euler-Bernoulli law for beams. It can be applied to elastic panels if the following conditions are satisfied [55, 56]:

- The panel is thin, which means that the thickness h is small in comparison to the other dimensions of panel (i.e. a — length and b — width).
- The panel is symmetric about the mid-surface (equivalently: the neutral plane), i.e., the planes perpendicular to the mid-surface will remain perpendicular after deformation of the panel.
- The rotating transverse normals remain perpendicular to the mid-surface after deformation of the panel.
- The transverse normals are not elongated during deformation of the panel — they are inextensible.

3.2.1 Isotropic steel panel

The governing equation describing transverse displacement w during vibration of free isotropic panel without any additional elements on its surface can be written as [57]:

$$D\nabla^4 w + \rho\frac{\partial^2 w}{\partial t^2} = 0, \tag{3.1}$$

where D is the flexural rigidity, defined as:

$$D = \frac{Eh^3}{12(1-\nu^2)}, \tag{3.2}$$

w is the transverse displacement, E is Young's modulus, ρ is mass density per unit area of the panel, t is time, h is thickness of the panel, ν is Poisson's ratio, and ∇^2 is the Laplacian operator. The previous assumptions imply that the normal strain along z direction can be neglected:

$$\frac{\partial w}{\partial z} = 0. \tag{3.3}$$

The Laplacian operator can be also expressed as [58]:

$$\nabla^2 = \frac{\partial^2}{\partial x^2} + \frac{\partial^2}{\partial y^2} = 0. \tag{3.4}$$

Thus, an equation (Eq. 3.1) can be written as:

$$D\left(\frac{\partial^4 w(x,y,t)}{\partial x^4} + 2\frac{\partial^4 w(x,y,t)}{\partial x^2 \partial y^2} + \frac{\partial^4 w(x,y,t)}{\partial y^4}\right) + \rho\frac{\partial^2 w(x,y,t)}{\partial t^2} = 0. \tag{3.5}$$

As stated in Section 2.2.1, the panel is mounted on a rigid frame casing using additional frame, providing approximately fully clamped boundary conditions [59]:

$$w = 0, \frac{\partial w}{\partial x} = 0 \text{ at } x = 0 \vee x = a \text{ for } 0 \leq y \leq b, \tag{3.6}$$

$$w = 0, \frac{\partial w}{\partial y} = 0 \text{ at } y = 0 \vee y = b \text{ for } 0 \leq x \leq a. \tag{3.7}$$

3.2.2 Orthotropic aluminum panel

Opposite to the isotropic panels, the orthotropic panels have different properties in both the orthogonal axes along the panel surface. The governing equation for the orthotropic panels can be obtained by modification of Equation 3.5, by taking into account the differences in material properties in x and y directions. Thus, it can be expressed as [60]:

$$D_x\frac{\partial^4 w(x,y,t)}{\partial x^4} + 2(D_x\nu_y + 2D_{xy})\frac{\partial^4 w(x,y,t)}{\partial x^2 \partial y^2} + D_y\frac{\partial^4 w(x,y,t)}{\partial y^4} + \rho\frac{\partial^2 w(x,y,t)}{\partial t^2} = 0, \tag{3.8}$$

where D_x, D_y and D_{xy} are the flexural rigidities, respectively defined as:

$$D_x = \frac{E_x h^3}{12(1-\nu_x\nu_y)},\ D_y = \frac{E_y h^3}{12(1-\nu_x\nu_y)},\ D_{xy} = \frac{Gh^3}{12}, \tag{3.9}$$

E_x, E_y are Young's moduli along x and y directions, respectively, ν_x, ν_y are Poisson's ratios for x and y directions, respectively, and G is rigidity modulus.

3.3 Piezoelectric shunt damping

Piezoelectrics are the group of materials, which can strain when electrical energy is applied across them, or can generate voltage during deformation of the element, basing on the phenomenon of electrical induction. The reason is that piezoelectric elements can transform energy between mechanical and electrical in both ways. The elements attached to the vibrating structure absorb the mechanical energy, transform it into the electrical charge and store in internal capacitance of the elements. To dissipate this energy, PSDa circuits are employed. In literature two main groups of PSDa circuits can be found: passive, and semi-active with switching. The most common examples of the piezoelectric elements used in PSDa cicruits are lead zirconate titane (PZT) or MFC.

3.3.1 Passive circuit

The main assumption in passive circuits, is they work without external energy. The easiest way to dissipate an electrical charge, is adding the resistor into the circuit. In these circuits, some of the energy is lost as heat emitted by the resistor. Additionally, by adding the inductor it is possible to build a shunt resonant circuit, using previosly mentioned resistor and internal capacitance of the piezoelectric elements [61]. These circuits are more effective, however, it could be tuned only to the single frequency of vibration. The values of inductance and resistance are optimised for the specific mode. Morover, passive RLC circuits are sensitive for changes of environmental conditions, e.g. temperature, and require large values of inductance, often higher than actually exists. To overcome this problem, Fleming et al. proposed a modified PSDa circuit with additional capacitance across the terminals of piezoelectric element [62]. However, parallel added capacitors worsen control performance. Therefore, the same authors proposed modified solution based on the circuit with negative capacitance, implemented using operational amplifiers (opamps), capable to reduce the required inductance with a good control performance [63]. However, in practical applications these circuits can be unstable. Besides the single-mode circuits, multimodal solutions were also proposed [64], [65]. Another approach to implement passive RLC shunt circuits are synthetic inductors built from the opamps [66]. However, as the negative capacitance circuits,

the opamps require an additional source of energy to be supplied, which makes this solution an active system. The other approach is switching circuit, widely developed in the synchronized switched damping (SSD) idea.

3.3.2 Switching circuit

The idea of switching circuit assumes switching between open and short states, four times during each period of vibration, when the structure reaches minimal or maximal displacement [67]. A time of switching is determined by the properly selected switching law. The most popular SSD method is SSD on inductor (SSDI), which is in fact switching RLC circuit [68]. This method can be implemented passively or semi-actively, which depends on the type of source of energy necessary to control the switches. Besides the SSDI, many other variations of SSD were developed. The basic method is SSD with short circuit (SSDS), where the energy is disspated only by the use of the resistor [69]. In 2006 Lefeuvre et al. proposed method with external voltage sources to improve the efficiency of vibration damping [70]. This method is known as SSD on voltage sources (SSDV). Badel proposed improvement SSD on adaptive voltage sources (SSDVa) to overcome the problems with stability. The value of voltage generated by an external source is automatically adjusted and proportional to displacement of the structure [71]. Another approach is the use of SSD with negative capacitance (SSDNC) instead of inductor, which may provide significantly better results than SSDI [72]. However, this solution is also active, because of opamps presence in the circuit.

3.4 Synchronized switch damping

The presented research is based on a rigid frame casing, described in Section 2.2. The experiments are divided into two stages, with different types of front panel and number of piezoelectric elements: 0.5 mm thick steel isotropic panel with five MFCs, and 1.0 mm thick aluminum orthotropic panel with nine MFCs. Both the experiments were performed using the different laboratory setup. The other walls of casing, i.e. top and side are made from 3 mm aluminum panels to enhance acoustic insulation of the investigated casing. The MFC elements were attached to the front panel's surface using epoxy glue to assure mechanical coupling between the vibrating structure and piezoelectric elements as high as it is possible. The SSDI circuit works efficiently for the higher values of voltage generated by the piezoelectric elements, hence, MFCs were connected in series. The places of attachement of the elements were determined by

positions of anti-nodes in investigated modeshapes of the vibrating structure.

3.4.1 Isotropic steel panel

During the first stage an 11^{th} mode was investigated (Fig. 2.3). MFCs were attached in the places of anti-nodes, compatible in phase (Fig. 3.1).

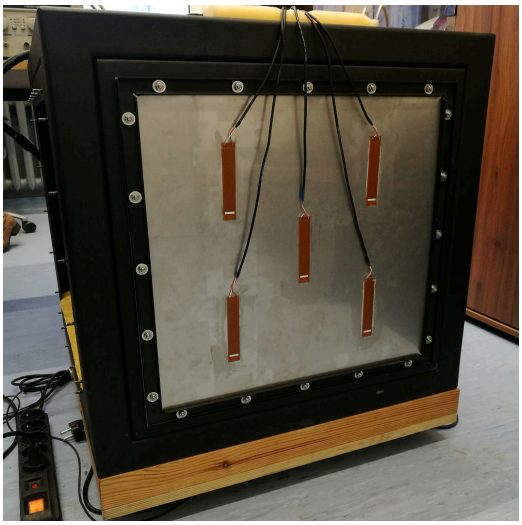

Figure 3.1: Rigid device casing with MFC elements used in the experiment.

The experiment was performed for three different circuits: open (Fig. 3.2(a)), short (Fig. 3.2(b)), and passive SSDI (Fig. 3.2(c)). MFCs in open circuit remain stiff and absorb energy from the vibrating structure through the mechanical coupling. Then, the mechanical energy is converted into the electrical charge and stored in internal capacitance of elements. When the MFCs are in short circuit, the electrical energy is dissipated in a similar way to the discharging of the capacitor with connected terminals. In this state, MFCs become flexible. The SSDI switches between the open and short circuits [73]. To improve an efficiency of vibration damping, a proper switching time should be selected.

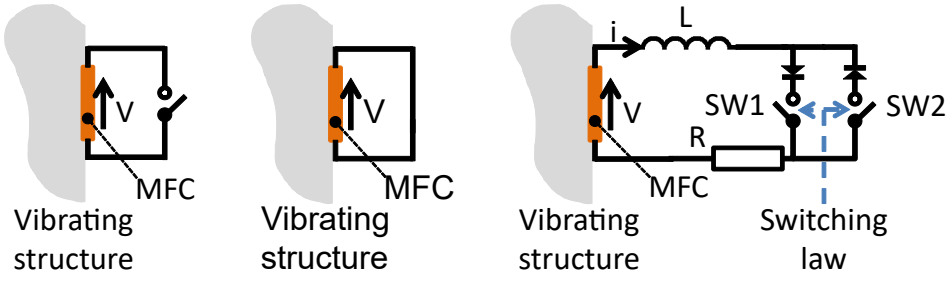

(a) Open. (b) Short. (c) SSDI.

Figure 3.2: Schematic representation of the circuits investigated in experiments.

The electrical representation of the passive SSDI implementation is presented in Figure 3.3. The circuit is a modification of the Wei's solution [74]. By the measurement of the voltage on the piezoelectric element and comparison with the previous value of the voltage, the change of the velocity direction of the structural vibration is detected. When the voltage decreases the sign of velocity also changes, and the circuit should be switched from open to short, to discharge the piezoelectric internal capacitance. The circuit is widely described by Mazur et al. [53]

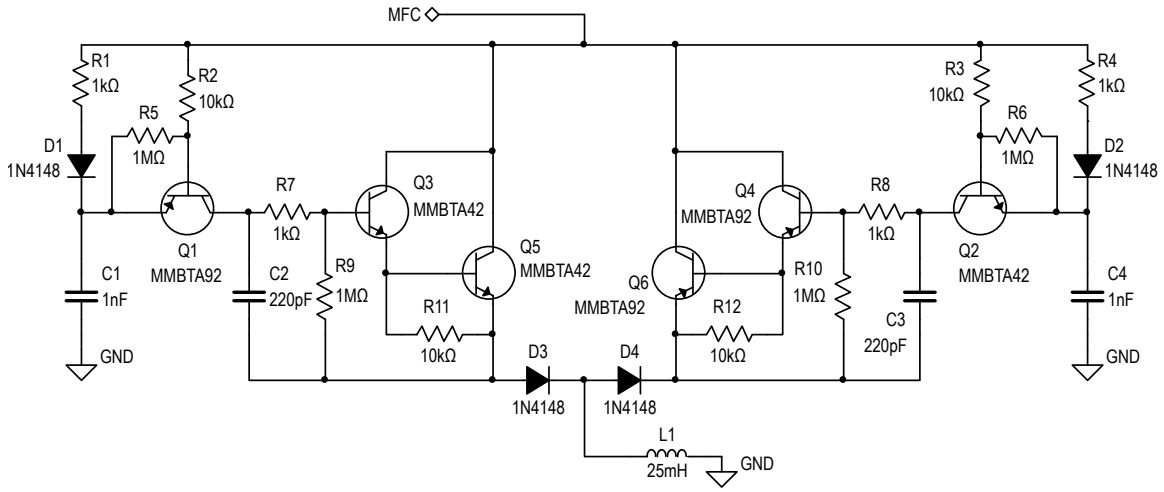

Figure 3.3: Electrical representation of implemented passive SSDI circuit [51].

An investigated structure mounted on a rigid frame casing is excited to vibration using active loudspeaker, placed outside the casing (Fig. 3.4). The loudspeaker emmits tonal signal, generated by NI myRIO in standalone mode, with direct digital synthesizer (DDS) signal generator application using NI LabVIEW FPGA. The structural vibration was measured using LDV, focused on the central point of a panel. The data was acquired using NI PCI-6289 data acquisition (DAQ) card, through the dedicated terminal panel. The measurements were processed and results were presented in NI LabVIEW graphical environment.

During the experiment an 11^{th} mode was investigated, which corresponds to 155 Hz, based on the preliminary experiment. However, with the changes of temperature the resonant frequencies change due to the thermal expansion of metal panels with fully clamped boundary conditions. Therefore, the structure was excited to vibration using a sequence of the tonal signals with frequencies varying from 143 Hz to 163 Hz with 0.1 Hz step. In this case, an 11^{th} mode appeared at 160.1 Hz. In Figure 3.5 an energy spectral density (ESD) of the measured signal is presented. It was observed that the energy values for open and short states are similar, while the frequencies are shifted.

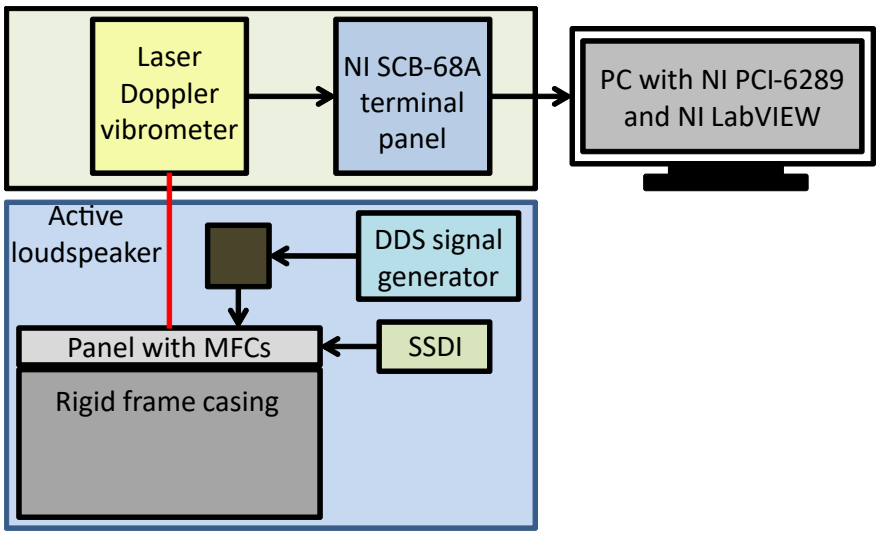

Figure 3.4: Scheme of measurement and control system for the SSDI experiment with isotropic panel.

It can be explained by the different MFC properties in both the states. In open state MFC is stiff and, in consequence, the resonant frequencies increase. When the piezoelectric element is short-circuited it becomes flexible. However, it should be noted that MFCs are still physically present on the structure and, depending on the mass ratio between the MFC and panel, it may affect the structure as an additional mass. For SSDI an approximately 3.5 dB energy value drop is observed.

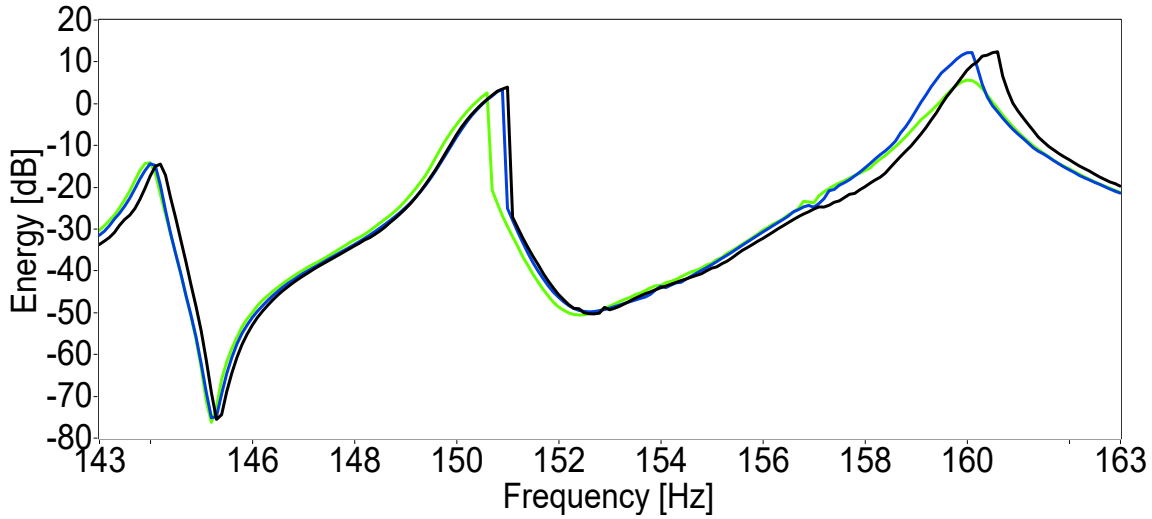

Figure 3.5: ESD of measured vibration for open (black), short (blue), and SSDI (green) circuits [52].

In Figure 3.6, the displacement of the structure is presented, during vibration with resonant frequency corresponding to an 11^{th} mode. It was observed that when the

elements are stiff, i.e., the circuit is open, the displacement of the structure is lower by approximately 16% in comparison to the short-circuited MFCs. With the SSDI this difference is approximately 31%. However, it is noteworthy that results for open circuit are seemingly better, due to the resonance shifting.

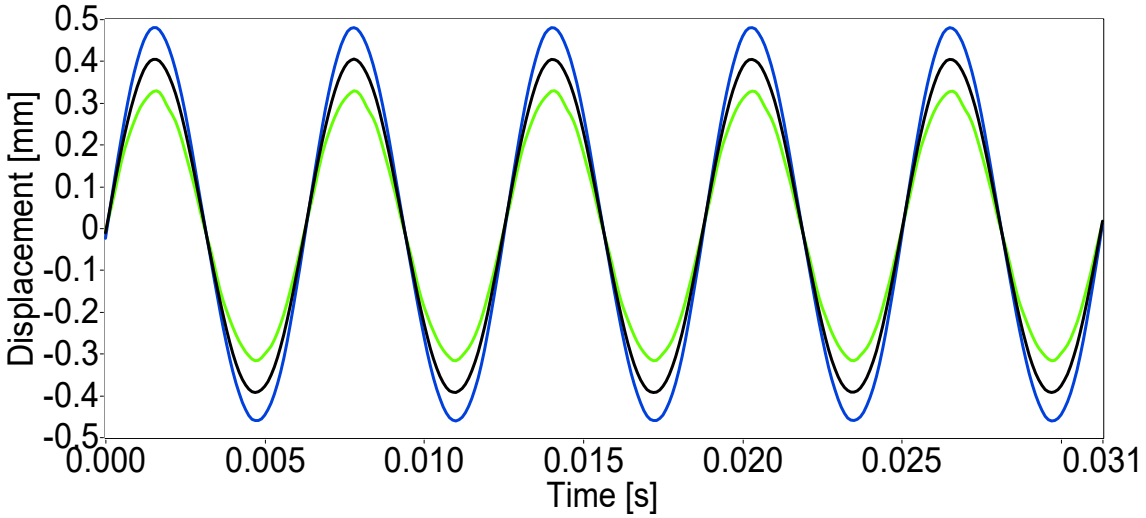

Figure 3.6: Displacement of the central point of vibrating structure, for open (black), short (blue), and SSDI (green) circuits [52].

3.4.2 Orthotropic aluminum panel

The second experiment was focused on the 5^{th} and 6^{th} modes (Fig. 2.3). MFC elements were attached in the places of anti-nodes of both the modes (Fig. 3.7).

Figure 3.7: Rigid device casing with MFC elements used in experiment [53].

The experiment was performed with MFC in open and short circuits. The SSDI was investigated in two different implementations: passive (the same, as before), and semi-active. Additionally, the results were compared with SSDV, representing an active circuits.

In the semi-active SSDI the switching between open and short circuits was implemented based on the metal-oxide semiconductor field-effect transistors (MOSFET) (Fig. 3.8) [53]. The circuit can also work as an unsymmetrical SSDV after changing the position of the SW1A switch, which was implemented on the second, identical printed circuit board (PCB).

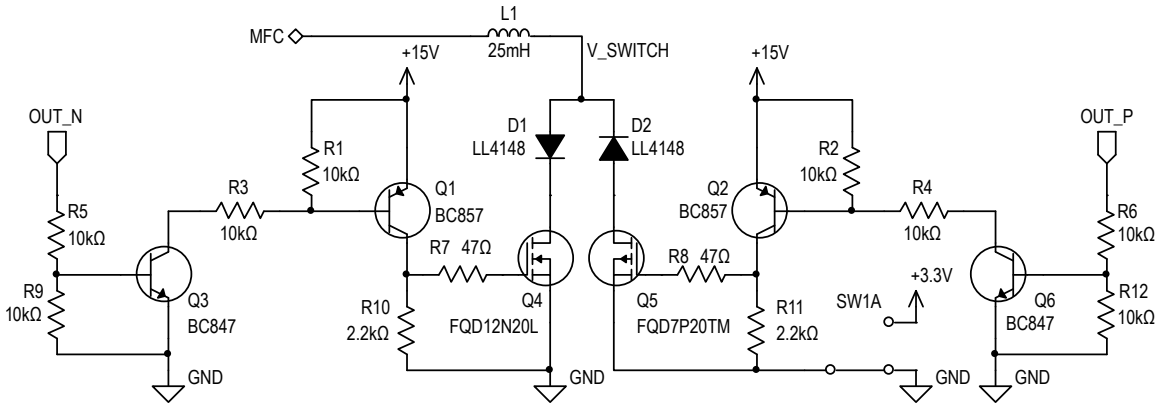

Figure 3.8: Electrical representation of implemented semi-active SSDI [53].

The semi-active implementation of the SSDI circuit presented above is widely described by Mazur et al. [53] with the information about design and principle of work.

The laboratory setup is similar to the configuration described in Section 3.4.1, however, the loudspeaker was placed inside the casing. The excitation, i.e., tonal signals were generated by dedicated microcontroller, placed on the same PCB as semi-active implementation of SSDI. The communucation between PCB and computer was established in both the directions, hence, the experiment can be performed remotely. The signals were acquired using dSpace platform, after passing through the anti-aliasing filters (Fig. 3.9).

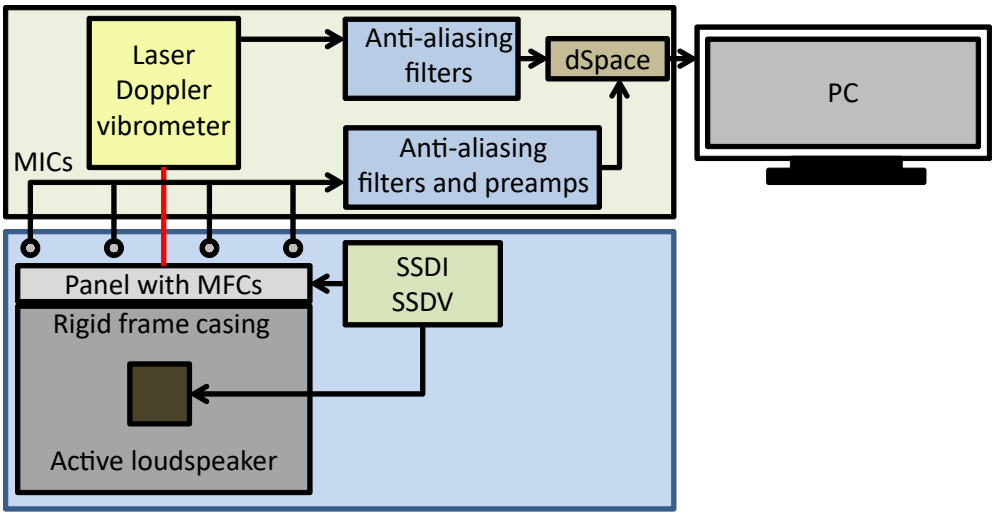

Figure 3.9: Scheme of measurement and control system for SSDI and SSDV experiment with orthotropic panel.

The vibration and noise were measured using LDV and microphones, respectively (Fig. 3.10). The microphones are distributed arbitrarly, with (x, y, z) coordinates presented in Table 3.1. M1—M4 microphones are placed near the vibrating panel to measure sound emission, while M5 and M6 measure sound pressure level (SPL) in places located far away from the casing. The coordinates system originates in the lower-mid section of the front side of casing.

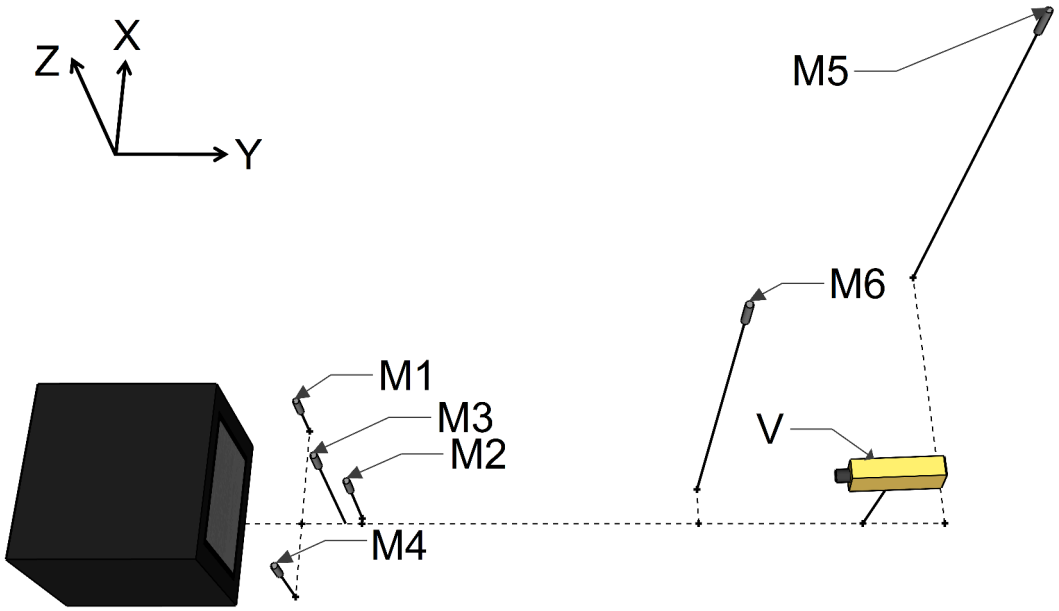

Figure 3.10: Scheme of the placement of microphones, LDV, and the casing.

Table 3.1: Sensors coordinates — values are given in meters.

Axis/Sensor	**M1**	**M2**	**M3**	**M4**	**M5**	**M6**	**V**
x	0.37	0.02	0	-0.27	1.01	0.13	0
y	0.21	0.43	0.37	0.21	2.56	1.66	2.26
z	0.35	0.32	0.73	0.31	1.58	1.45	0.55

In Table 3.2 the values of power of the noise and vibration are presented, relative to the corresponding frequency. The results are divided into three sections:

- Passive implementation of the SSDI, where an open circuit was not technically available. By the reduction, a difference of power of measured noise and vibration between short circuit and passive SSDI is meant.
- Semi-active implementation of the SSDI, where the reduction is the difference of power of measured noise and vibration between the short circuit and the best case.
- Active SSDV circuit, where a short circuit was not technically available. By the reduction a difference of power of measured noise and vibration between open circuit and SSDV is meant.

Table 3.2: Power of the signals measured by microphones and LDV, for investigated circuits [53].

Circuit	**Freq. [Hz]**	**V [dB]**	**M1 [dB]**	**M2 [dB]**	**M3 [dB]**	**M4 [dB]**	**M5 [dB]**	**M6 [dB]**
Short	166.5	-27.8	-34.4	-39.9	-40.9	-32.2	-50.5	-48.6
Passive	166.5	-31.6	-36.6	-47.2	-43.8	-33.9	-50.2	-51.2
Reduction	166.5	+3.8	+2.2	+7.3	+2.9	+1.7	-0.3	+2.6
Open	166.6	-27.4	-34.4	-36.9	-37.0	-33.9	-43.4	-45.3
Short	166.6	-27.6	-35.1	-36.7	-37.2	-37.2	-43.8	-45.8
Semi-active	166.6	-32.1	-42.5	-45.6	-40.7	-36.2	-56.5	-56.5
Reduction	166.6	+4.5	+7.4	+8.9	+3.5	-1.0	+12.7	+10.7
Open	165.9	-27.7	-34.6	-36.9	-38.3	-35.0	-44.2	-45.4
Active	165.9	-33.2	-45.7	-47.0	-42.1	-37.8	-64.5	-59.0
Reduction	165.9	+5.5	+11.1	+10.1	+3.8	+2.8	+20.3	+13.6

The best results were achieved for the SSDV circuit, as it was expected. The highest improvement of the vibration reduction was 5.5 dB, while for the semi-active and passive SSDI it was 4.5 dB and 3.8 dB, respectively. Moreover, for the semi-active case, it was observed that the power of noise and vibration signals measured while MFC elements were in open circuit was higher in comparison to the short circuit. This lead to the conclusion that permanent change of the stiffness of the structure in this particular case, worsen the efficiency of the noise and vibration reduction.

3.5 Influence of casing walls on front panel frequency response

To obtain better efficiency of SSDI circuit, the voltage generated by the MFC elements should be increased. In this Section the top and side walls made from different materials are investigated, as well as different types of front wall — a single panel or double-panel structure. The experimental setup is presented in Figure 3.11. The main element is a rigid frame casing with an active loudspeaker, placed inside. The excitation signal is provided by the external DDS generator. Vibration of the central point of investigated structure is measured using LDV, connected to PCI DAQ card, through the dedicated terminal panel. The data was acquired with 20 kHz sampling rate. The application for data acquisition, processing and presentation was developed in LabVIEW.

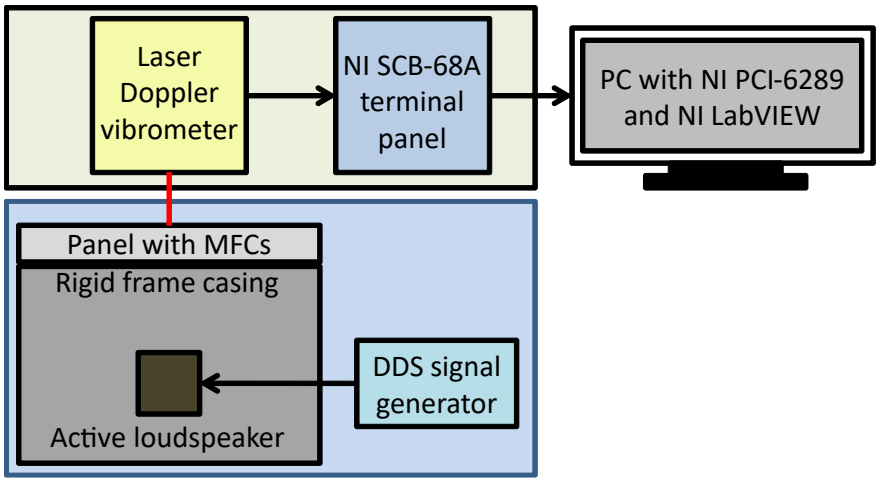

Figure 3.11: Scheme of experimental setup for measurement of panel's response characteristics.

During the experiment, numerous configurations were investigated, i.e. a single panel as the front wall:

- without top and side walls,
- with foam layers as walls,
- with 3 mm aluminum panels as walls,
- with 3 mm aluminum panels as walls with additional foam layer,
- with 3 mm plywood panels as walls,

and a double-panel structure as the front wall:

- without top and side walls,
- with foam layers as walls,
- with 3 mm aluminum panels as walls.

A single panel is a 0.5 mm thick isotropic steel panel, mounted on the outer side of the casing. In a double-panel structure, the 0.6 mm thick isotropic steel panel is mounted additionally on the inner side of the casing. The results of the experiments are presented in Figures 3.12 to 3.15, as a PSD, estimated using the Welch's method, recalculated to an ESD. The frequency range of analysed data was limited to 260 Hz.

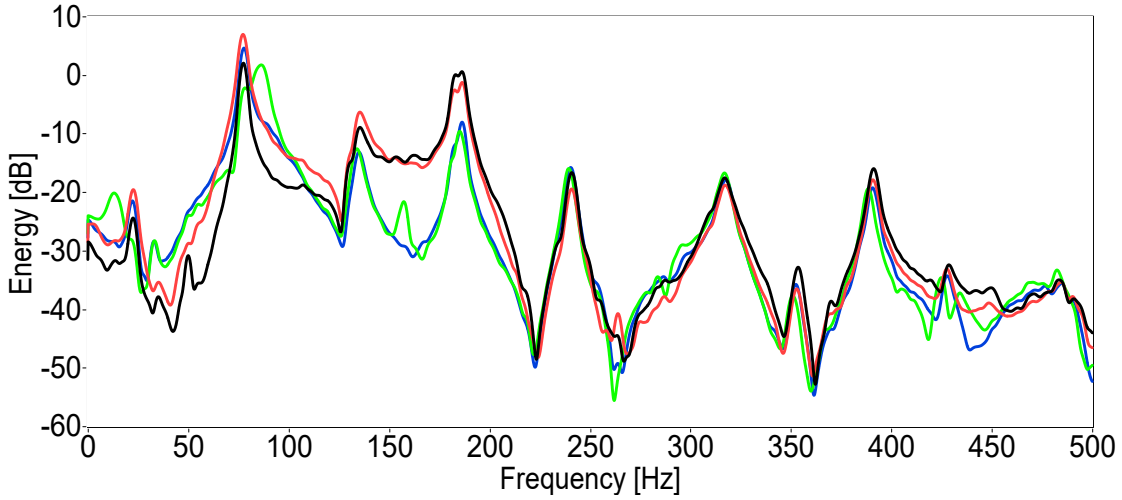

Figure 3.12: ESD of measured vibration for the walls made from different materials: frame without walls (black); foams (red); aluminum (green); plywood (blue), with a single panel as a front wall.

In Figure 3.12 it was observed that for the frame without walls, ESD of measured vibration was comparable to the results obtained for the frame with foams. The only exception was a peak that appeared in frequency around 50 Hz for the frame. For the

aluminum, differences were observed at around 15 Hz, 75 Hz, 85 Hz and 150–155 Hz. For the plywood, ESD of measured vibration was comparable to the results obtained for the frame and foams. It was observed for the frequencies up to 100 Hz, but the rest of the investigated frequency band is more similar to aluminum with the only exception at around 150–155 Hz. However, plywood has beneficial damping properties, due to bitumen layer, attached on panels, thus, it is not investigated in further experiments. In Figure 3.13 the frame with a single panel is compared with the frame with a double-panel structure.

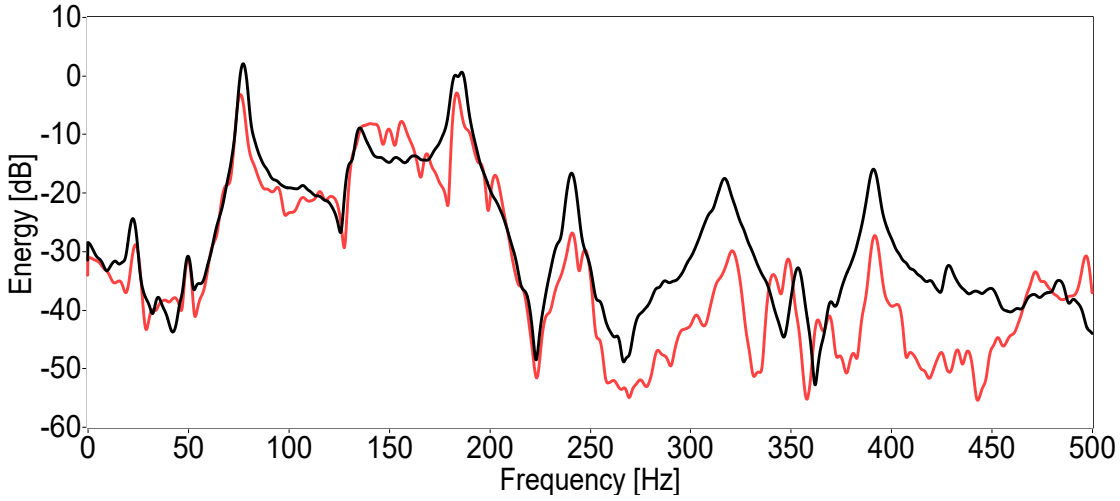

Figure 3.13: ESD of measured vibration for the frame with a single panel (black), and frame with a double-panel structure (red).

The ESD characteristic of measured vibration for a single panel is more smooth, in opposite to a double-panel structure, where the number of peaks and valleys are significantly higher between 75 Hz and 210 Hz. However, the ESD of measured vibration for a double-panel structure is lower in comparison to ESD of measured vibration for a single panel, except 135–170 Hz frequency range. In Figure 3.14 a comparison between a single panel and double-panel structure for the foam layers, as the side and top walls are presented. ESD of measured vibration for a double-panel structure is similar to the analogous ESD of measured vibration for the frame. However, the peak around 50 Hz for a double-panel structure is similar to the observed one on ESD of measured vibration for both the frame configurations (Fig. 3.13).

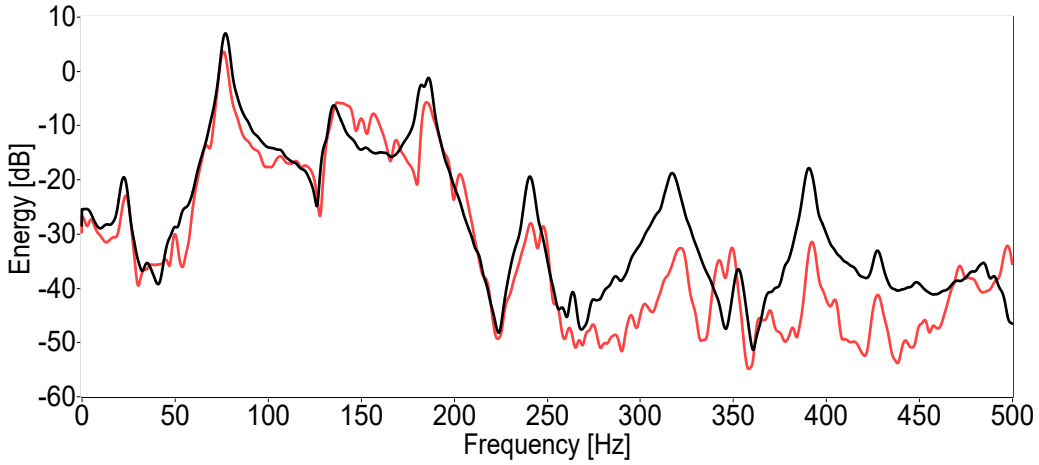

Figure 3.14: ESD of measured vibration for foams with a single panel (black), and foams with a double-panel structure (red).

In Figure 3.15, as for the previous materials, the ESD of measured vibration for a single panel is similar to the results obtained for a double-panel structure, but only above 55 Hz.

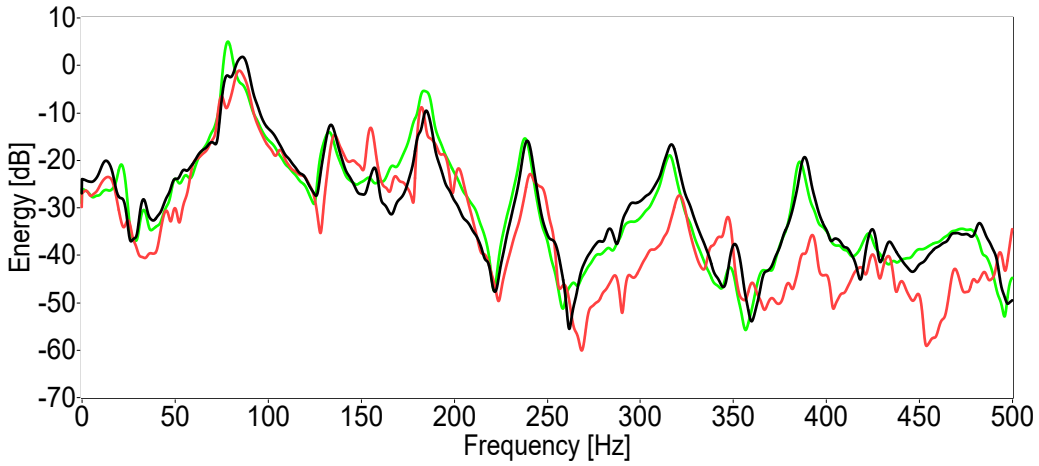

Figure 3.15: ESD of measured vibration for aluminum with a single panel (black), aluminum with a double-panel structure (red), and aluminum with foams and a single panel (green).

Below this frequency, it is more similar to a single panel with foams. It is worth mentioning that a combination of different materials, such as aluminum and foams, allows to shape an investigated panel's characteristic. Especially, it was observed on the magnified peaks around 20 Hz, 80 Hz and on the damped peak around 150–170 Hz, where the results were more similar to case with foams than to the case with aluminum.

The main conclusion is that the plywood with additional bitumen layer is the most beneficial for vibration reduction in comparison to other considered materials. The

use of a double-panel structure reduces the vibration in a major of the investigated frequency range. The combination of aluminum panels with foams proved that the sandwitch structures can be used as the passive method of shaping of the frequency characteristics.

3.6 Single electromagnetic coupling

In this Section, a preliminary experiment with the use of a new type of electromagnetic coupling is presented. The technical details and principle of work of the element are widely described in Section 4.2. The electromagnetic coupling was mounted on the stiff, aluminum profiles, rigidly connected with the frame of a casing (Fig. 3.16). This configuration allows for holding the vibrating panel, similarly to the spring connection with the rigid frame of the casing. The force of coupling varies depending on the force generated by the element.

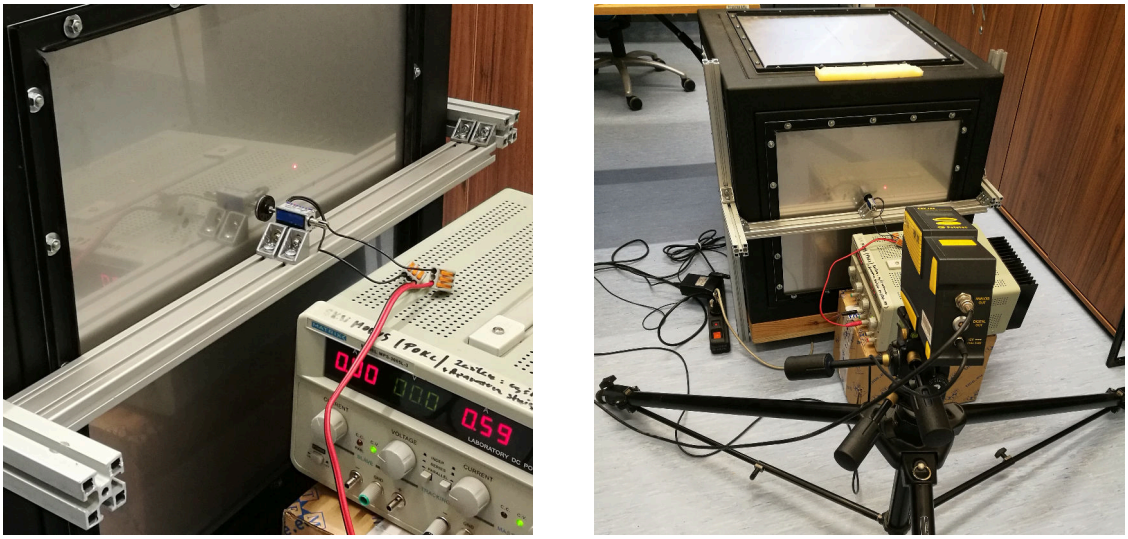

(a) Electromagnetic coupling. (b) Casing with LDV.

Figure 3.16: Laboratory setup used in the experiment.

The investigated structure is excited to vibration using an internal active loudspeaker emitting tonal signal with 147.9 Hz frequency, which corresponds to the 11^{th} mode. The source of the signal was DDS generator. Vibration of the panel was measured using LDV, connected to PCI-6289 DAQ card, through the dedicated terminal panel. The force, generated by the coupling element is set by the changing of the coil supply voltage on the external power supply unit (PSU), in range 0–11 V. The application for data acqusition and processing was developed in LabVIEW.

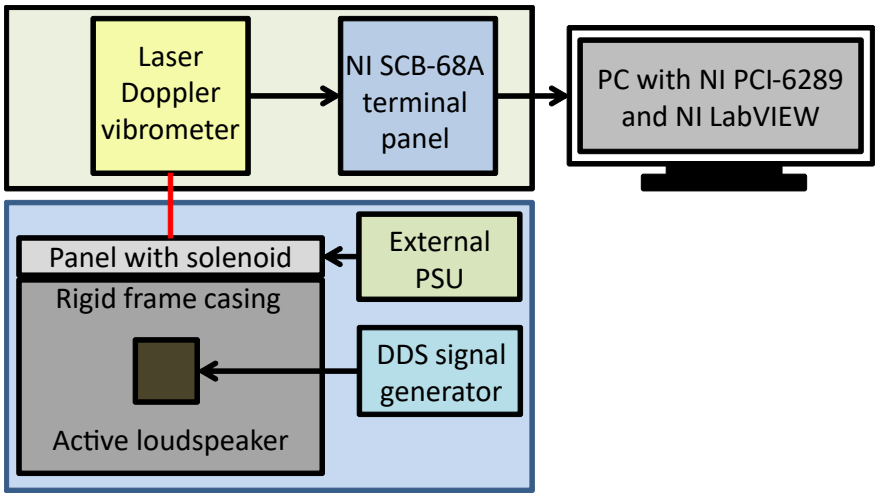

Figure 3.17: Scheme of measurement and control system for a single panel with a single electromagnetic element.

The vibration was measured in two points: farther away from the nodal line (Fig. 3.18(a)) and closer to the nodal line (Fig. 3.18(b)) of the 11^{th} mode.

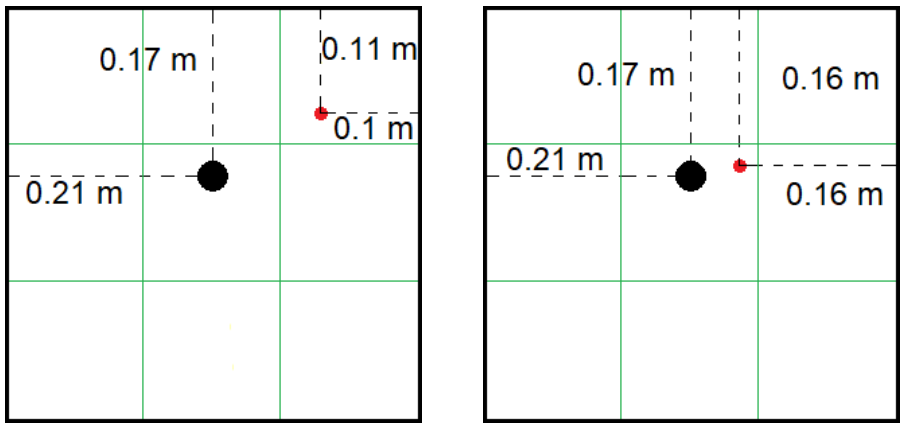

(a) Measurement point no. 1. (b) Measurement point no. 2.

Figure 3.18: Measurement points (red dots) and the placement of coupling (black dots).

The electromagnetic coupling was mounted near the center of the vibrating panel — in the same place for both the investigated cases. The value of coil supply voltage was changed from 0 V to 11 V, with 0.5 V step. Moreover, in Figure 3.18 the areas of nodal lines were marked with the green lines.

In Figure 3.19 a velocity of panel's vibration, measured in the point no. 1 is presented in function of coil supply voltage. It was observed that between 2.5 V and 4 V the velocity decreases significantly, while from 4.5 V the decrease is slight and almost linear. The measured velocity of a panel for 11 V is lower by 36% than the value

measured without activated coupling.

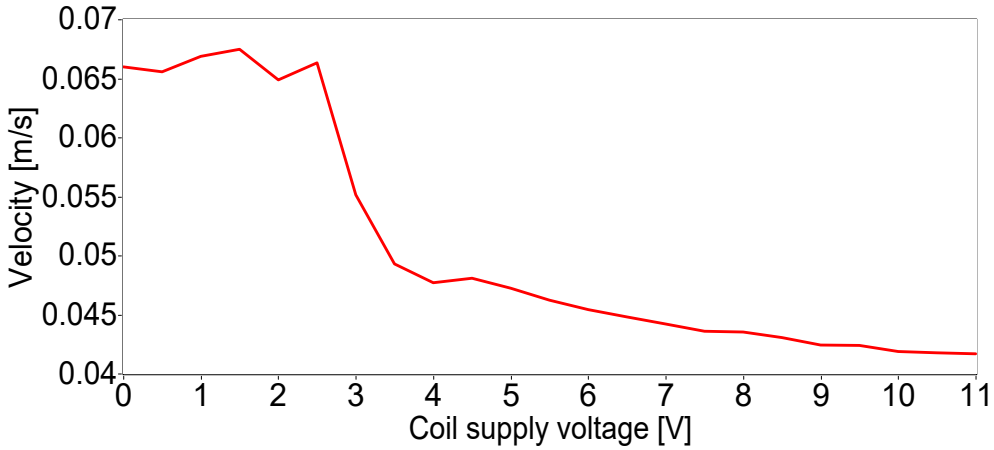

Figure 3.19: Velocity of panel's vibration measured in the point no. 1.

In Figure 3.19 a velocity of panel's vibration, measured in the point no. 2 is presented in function of coil supply voltage.

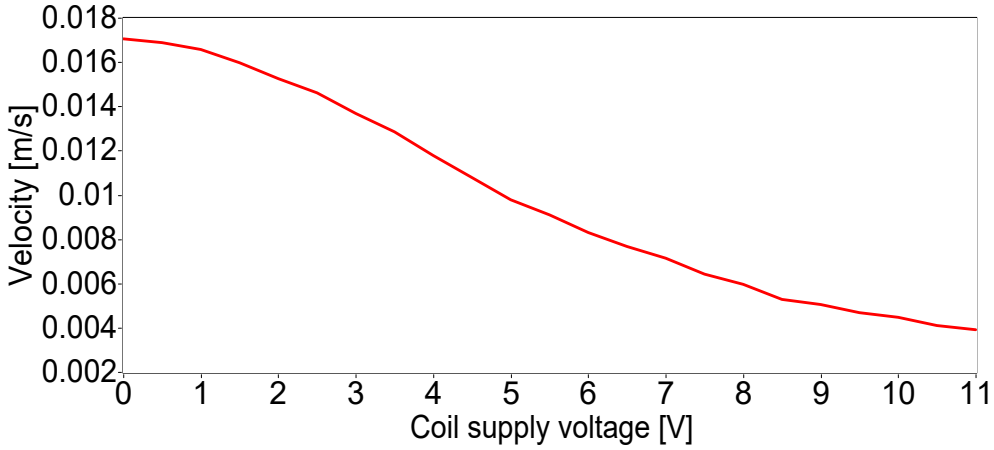

Figure 3.20: Velocity of panel's vibration measured in the point no. 2.

The velocity is four times less than in point no. 1, which results from the vibration amplitude differences closer and farther away from the areas of nodal lines. Moreover, it was observed that the decrease of the panel's velocity is almost linear. The difference between the measured velocity for 0 V and 11 V is 0.013 m/s, which is 72% of maximal value.

The obtained results of the preliminary experiment are promising, in both the cases a significant vibration reduction was observed. It is also noteworthy that the coupling works more efficiently closer to the areas of nodal lines. For that case the percentage difference between the highest and the lowest amplitude of the velocity was two times higher in comparison to the second case.

3.7 Discussion

In this Chapter the device casing with a single panel was investigated. The research was concentrated mainly on the semi-active shunt circuits with piezoelectric elements. However, the results were compared with the other types, i.e., passive and active. Moreover, the new electromagnetic coupling element was preliminarily tested. The influence of the type and material of the casing walls on the frequency response of a front panel was also investigated.

In the first experiment an isotropic steel panel with a five MFCs was considered. The ESD of the measured vibration was compared for three different MFC circuits: open, short and a passive implementation of SSDI. The last circuit provided approximately 3.5 dB of vibration reduction in comparison to the short circuit, while the ESD for the open circuit remains similar.

The second experiment was similar, however, the panel was orthotropic and made from aluminum. Besides the circuits considered previously, the semi-active SSDI and active SSDV were also employed. Comparing the ESD of the measured vibration, the best results were obtained for the active system, as was expected. The least efficient was observed in semi-active and passive systems. The vibration reduction was 5.5 dB, 4.5 dB and 3.8 dB, respectively.

The next experiment concerned the influence of casing walls on the frequency response of a front panel. The three kinds of materials, i.e., foam, plywood, aluminum, and three types of walls, i.e., frame, solid, and layered structure were investigated. Moreover, the front wall was considered as a single and a double-panel structure, and combined in the various configurations with the top and side walls. It was observed that the plywood has the most beneficial damping properties among the considered materials. The double-panel structure as a front wall provides significantly better results in comparison to a single panel. It is noteworthy that it is possible to shape the characteristic of frequency response of the front wall, using the layered structures as a top and side walls.

In the last experiment the new type of electromagnetic coupling was preliminarily investigated. The element was rigidly connected to the frame of the casing and to the vibrating panel. The velocity of the panel was measured in two points: closer to the anti-node and closer to the nodal line of investigated modeshape. Based on the characteristics of the velocity in a function of coil supply voltage, it was observed that the element is more efficient near the area of nodal lines.

Chapter 4

Device casing with a double-panel structure

4.1 Background

A double-panel structure is widely used in industry and in transportation, due to its beneficial sound insulation. Moreover, it may be additionally improved by the modification of the panels, e.g. using metamaterials [75], or phononic crystals (PC) [76]. An alternative modification is an attachment of the piezoelectric elements on the panel surface, and use it as sensors or actuators [77]. The noise and vibration in a double-panel structure may be then reduced with the use of semi-active [78] or active methods [79]. The piezoelectric elements can be also connected into the arrays or stacks to enhance the efficiency of noise and vibration reduction [80]. Besides the panels modifications it is noteworthy that the vibroacoustic properties of a double-panel structure can be also enhanced by using different mediums [81], [82] or material layers [83] in cavity gap, between the panels. Moreover, if the distance between the panels is sufficient it is also possible to mounting additional elements, such as mass-spring dampers [84], vibration absorbers [85], or couplings (e.g. permanent magnets [86]).

A double-panel structure with the coupling elements between the panels was described, with the author's contribution, in context of both the electromagnetic and stiff, magnetic couplings. The use of a single, centrally placed electromagnetic coupling was investigated by comparison of the 1^{st}, 4^{th} and 11^{th} modeshapes, for different forces generated by the element. The results were obtained with the use of LDV, measuring panels vibration in 7×7 grid of points [87]. The 11^{th} modeshape was also investigated in

experiments with the use of five electromagnetic elements. The vibration was measured by the MFC elements, and the root mean square (RMS) values were calculated [88], as well as the PSD estimates [89]. The other paper presents a novel approach to observe the modeshapes of vibrating panel — the use of modified Chladni's experiment [90]. The last paper includes the stiff, neodymium coupling elements, placed inside a double-panel structure in various configurations, and the frequency response functions (FRF) are estimated using the microphone measurement [91].

This Chapter presents a research included in the papers [87–91]. However, it is extended by the full description of electromagnetic coupling conception, and the experimental validation of this element. Moreover, the research described in the papers were extended by the additional, more complex analysis of behaviour of electromagnetic couplings between the vibrating panels.

4.2 Electromagnetic couplings

4.2.1 Semi-active electromagnetic element for damping of transverse vibration of planar structures

During the research on semi-active methods for vibration damping, the electromagnetic element for damping of transverse vibration of planar structures was proposed in the patent [92]. The element can be used in objects such as devices casings, car bodies or other thin-walled barriers. The damper enables the reduction of surface vibration without adding external energy to the system. The lack of mechanical friction between the components results in its noiseless operation. Moreover, the damper can work in various configurations adapted to the application. It is also possible to dampen vibration over a large area, depending on the length of the ferromagnetic rod, and the electromagnetic force, generated by used coil. Additionally, the maximal stroke of the ferromagnetic rod can be adjusted without any modifications to the mechanical structure of the damper. Due to the semi-active work of the damper, the stability of the system is ensured. It is also possible to use a switching law, as in the PSDa circuits.

Inside the iron casing, a coil is rigidly mounted. The ferromagnetic rod moves frictionless inside the coil, thanks to the phenomenon of electromagnetic induction, along its longitudinal axis, and is connected rigidly to the element attached to the vibrating surface. The coil is attached to a vibrating structure or to the support element. The ferromagnetic rod is positioned at an angle from 0 to 90 degrees to the vibrating surface. The damper can be mounted in different configurations:

- with coil and ferromagnetic rod mounted on the same surface (Fig. 4.1(a)),
- with coil and ferromagnetic rod mounted on the parallel surfaces (Fig. 4.1(b)),
- with coil and ferromagnetic rod mounted on the perpendicular surfaces (Fig. 4.1(c)).

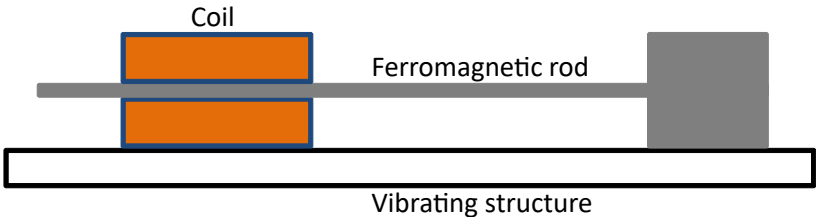

(a) Damper with coil and rod mounted on the same surface.

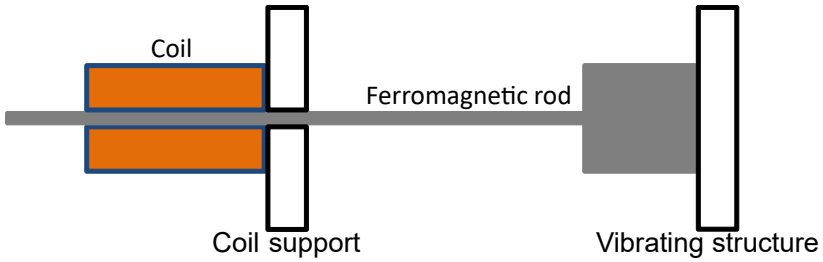

(b) Damper with coil and rod mounted on parallel surfaces.

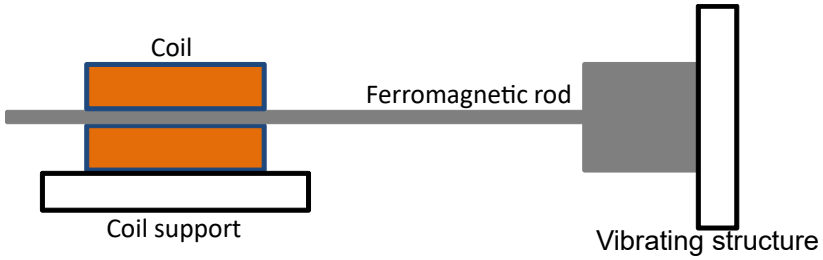

(c) Damper with coil and rod mounted on perpendicular surfaces.

Figure 4.1: Proposed semi-active damper, mounted in different configurations.

4.2.2 Properties of electromagnetic couplings

The idea of a damper described in the previous section can be implemented with the use of a simple push-pull solenoid with some modifications (Fig. 2.6(g)). The original damper (Fig. 4.2(a)) was too long to fit between the panels mounted on a rigid frame casing. Therefore, the length of core was shortened by 15 mm, to avoid hitting the panel by the core if the panels will vibrate in the opposite phases. The spring, nut and rubber ring were also removed to allow the core to move freely inside the coil.

The solenoid with partial modifications was tested using the laboratory electronic scale (Fig. 4.2(b)), to measure generated force dependently on the different parameters,

i.e.:

- value of coil supply voltage,
- displacement of core,
- frequency of pulse-width modulation (PWM) signal,
- order of duty cycle change (hysteresis).

The maximal value of the coil supply voltage is 12 V. However, it was assumed that the coil supply voltage will not exceed 11 V — to avoid coil's overheating. The element was supplied by external PSU connected to PWM controller (Fig. 2.6(f)) providing 0 — 11 V voltage values. When the maximal voltage is applied to the element, it generates its maximal force, and 0 V corresponding to the situation, when the core moves freely inside the coil. The exact value of voltage depends on the duty cycle of PWM signal, set on NI myRIO (Fig. 2.6(b)).

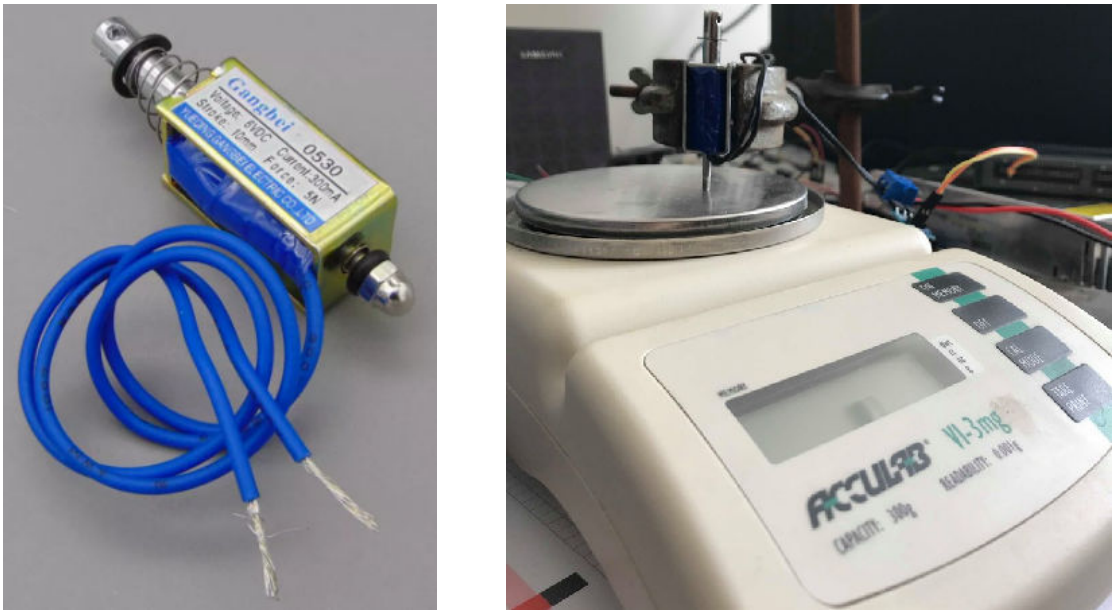

(a) Original solenoid. (b) Electronic scale with solenoid.

Figure 4.2: Solenoid before modifications (a), and Acculab VI-3mg electronic scale with solenoid mounted on stand (b).

The first experiment was performed for two different core's displacements: p1 — 5 mm, p2 — 1 mm, and three coil supply voltage values, with 1 kHz PWM frequency (Fig. 4.3). The core's displacement is a distance between the central point of the ferromagnetic part of the core and the central point of the coil, where the magnetic

field is the strongest. The duty cycle value was changed from 0% to 10% with 1% step, and from 10% to 100% with 5% step.

It was observed that the core's displacement has significant influence on the generated force, higher than the value of the coil supply voltage. The other conclusion was that it is unnecessary to use dense distribution of measurement points between 0% and 10% duty cycle. However, it should be considered above 70%, especially from 90% to 100%, where the growth of force is more rapid.

The second experiment was performed for five different PWM frequency values, and 9 V coil supply voltage value (Fig. 4.4). The core's displacement was constant, but not measured. The duty cycle value was changed from 0% to 10% with 10% step, from 10% to 70% with 5% step, from 70% to 90% with 2% step, and from 90% to 100% with 1% step.

The main conclusion was that the efficiency of the solenoid up to 90% of duty cycle is inversely proportional to PWM frequency. The highest differences of generated forces were observed for 78% duty cycle, between 500 Hz and 10 kHz, and between 1 kHz and 10 kHz. The differences were 17.43% and 9.34% of maximal force, respectively. However, above 90% duty cycle the relation between solenoid's efficiency and PWM frequency became directly proportional. The highest differences of generated forces were observed for 100% duty cycle, between 10 kHz and 500 Hz, and between 10 kHz and 1 kHz. The differences were 29.58% and 15.55% of maximal force, respectively.

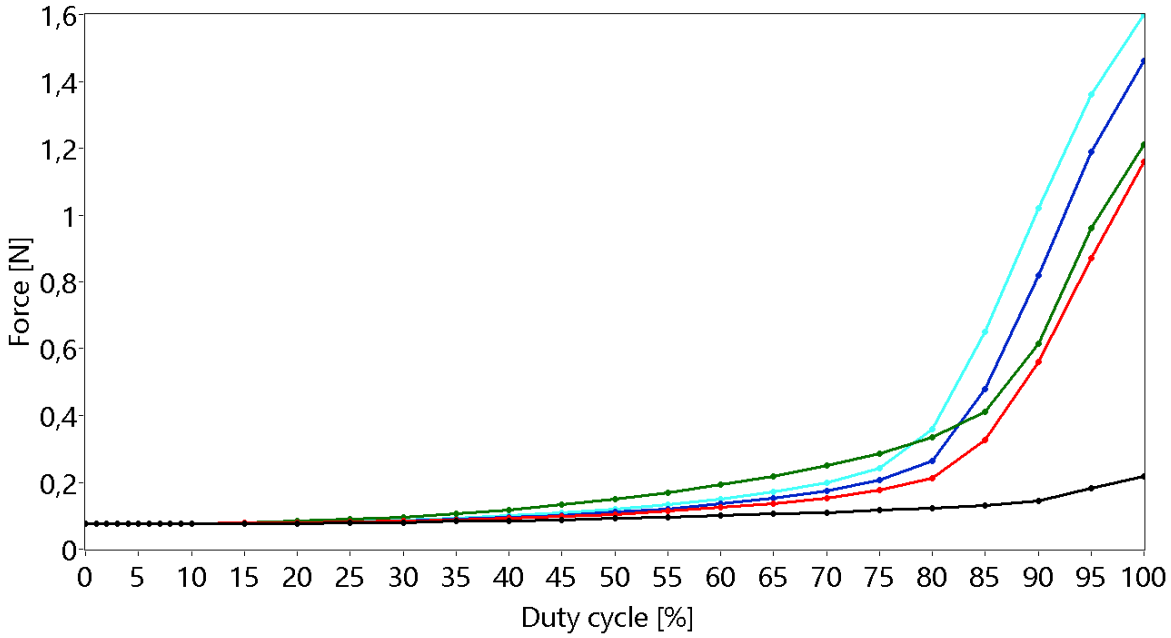

Figure 4.3: Comparison of solenoids' characteristics of force in PWM's duty cycle function, depending on core's displacement and coil supply voltage.

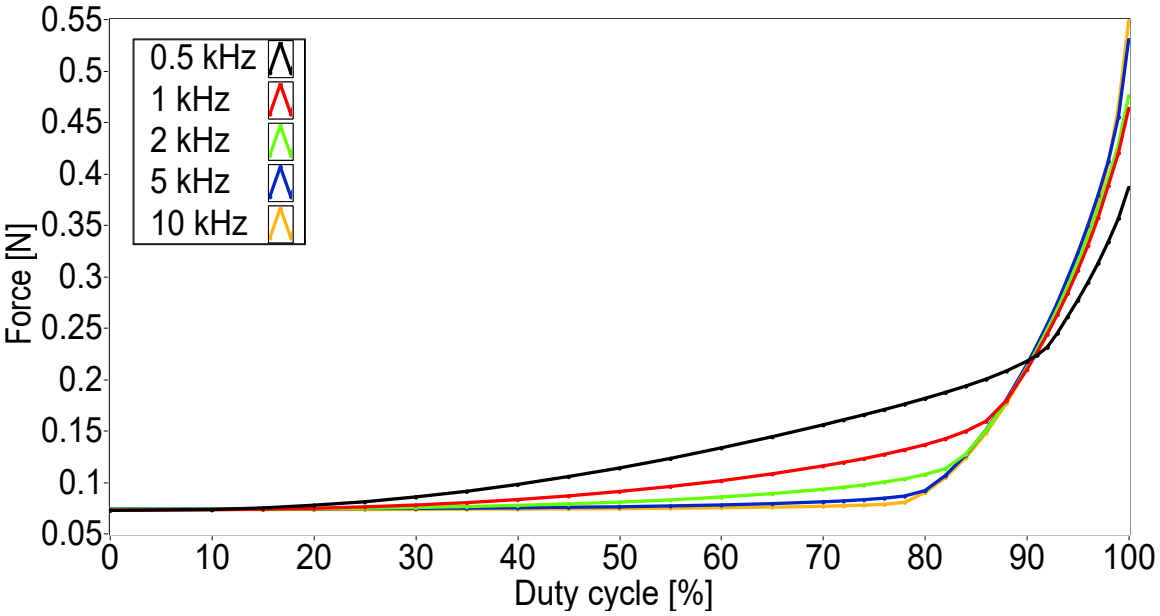

Figure 4.4: Comparison of solenoids' characteristics of force in PWM's duty cycle function, depending on PWM frequency.

The hysteresis loop was investigated for 9 V coil supply voltage value and 10 kHz PWM frequency (Fig. 4.5). The core's displacement was not measured. The obtained data were interpolated (Fig. 4.6).

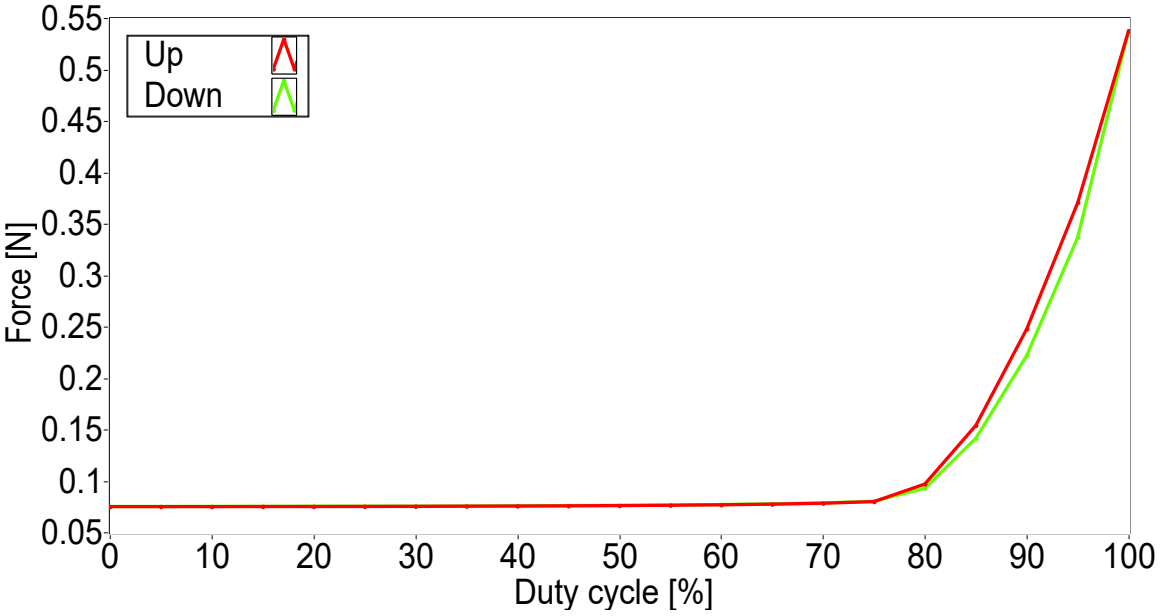

Figure 4.5: Hysteresis loop of investigated solenoid.

The hysteresis loop is narrow, because the core is made from soft ferromagnetic material. The enlargement of hysteresis loop is presented in Figure 4.6, where the widest area is marked with black cursors.

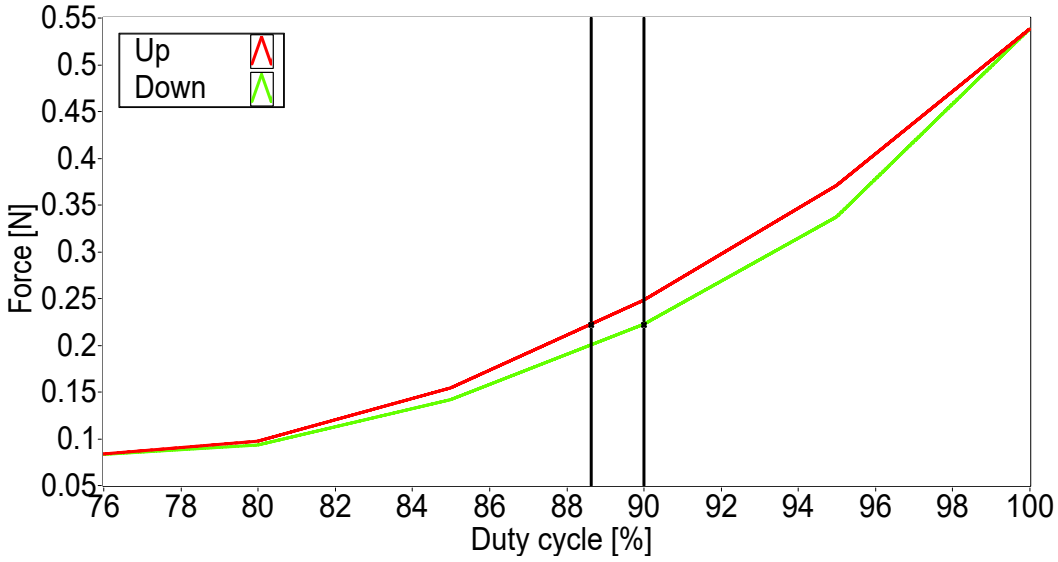

Figure 4.6: Enlargement of interpolated measurements of hysteresis loop.

In industrial valves hysteresis is defined as the percentage ratio of the highest difference between values of control current, applied to the valve to set the same values of flow, and rated current [93]. In solenoids (oftenly used in valves) the current is directly related with the duty cycle of PWM signal and the values of flow corresponds to applied force. Thus, the hysteresis can be also expressed as:

$$H = \left(\frac{DC_{up} - DC_{dw}}{DC_{max}} \right) \cdot 100\%; \tag{4.1}$$

where H is hysteresis, DC_{up}, DC_{dw} and DC_{max} are values of duty cycle up, down, and maximal, respectively. The maximal duty cycle value is related with rated current. For the investigated solenoid hysteresis is a 1.37%. This value variates depending on the temperature and parameters of the electromagnetic coupling element, e.g. value of coil supply voltage. According to the definition (Section 1.5), this element is not a smart material literally. However, this element placed inside a double-panel structure can be considered as a smart material in a macro scale.

4.2.3 Vibration damping using single coupling

The first experiment with elecromagnetic coupling inside the cavity of a double-panel structure was performed for the single element, coupling both the panels in central points. The experiment was performed according to the same scenario, and on the same laboratory setup as research described by Chrapońska et al. [87]. However, the presented results concerning different modeshapes, and different type of analysis, con-

stituting an extension of research included in mentioned paper.

As stated before, the core's displacement has the highest influence on a solenoid's efficiency. Therefore, the proper positions of both core and coil were achieved by using plastic discs with 3 mm thickness. The coil (Fig. 4.7(a)) was mounted on the incident panel and the modified core (Fig. 4.7(b)) was mounted on the radiating panel.

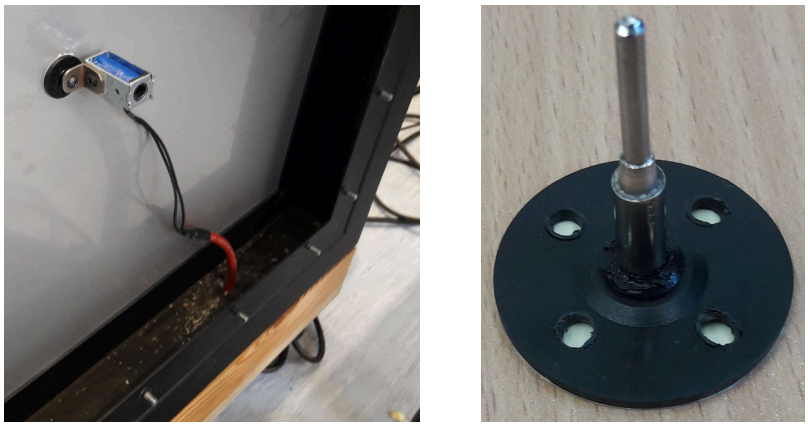

(a) Coil mounted on incident panel. (b) Core with plastic disc.

Figure 4.7: Coil and a core before mountage on radiating panel.

The laboratory setup is based on the rigid frame casing with a double-panel structure, coupled with a single electromagnetic element (Fig. 4.8).

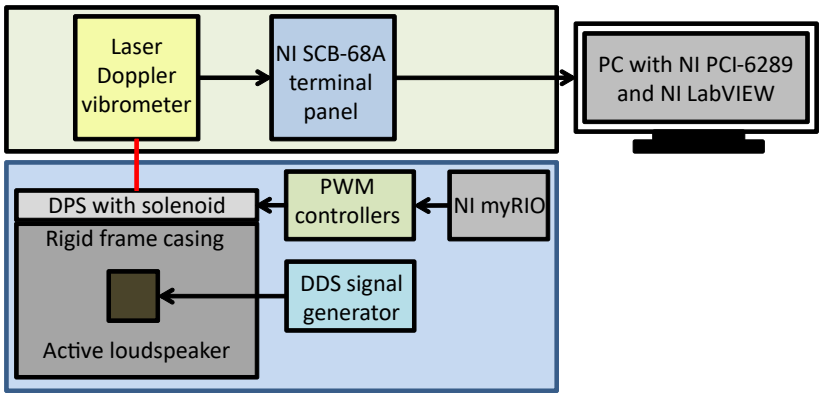

Figure 4.8: Scheme of measurement and control system for a double-panel structure with a single electromagnetic coupling.

The investigated structure is excited to vibration using internal active loudspeaker emitting uncorrelated random signal, band-limited to 500 Hz, with a constant PSD. The source of the signal was the DDS generator. Vibration of a double-panel structure was measured using LDV, connected to PCI-6289 DAQ card, through the dedicated terminal panel. The force generated by the solenoid is set by changing of the duty cycle

of PWM signal using myRIO platform. The application for data acqusition, processing and generation of the PWM signal was developed in LabVIEW.

The vibration was measured on a square grid of 49 points regularly distributed on the radiating panel (Fig. 4.9). The distance between the nearest points is 70 mm. During such experiments it is recommended to use more dense distribution of points. However, the temperature of solenoid coil fluctuates rapidly, which may result in change of boundary conditions, when the panel's dimensions change. It was the reason for the reduction of the density of grid of measurement points.

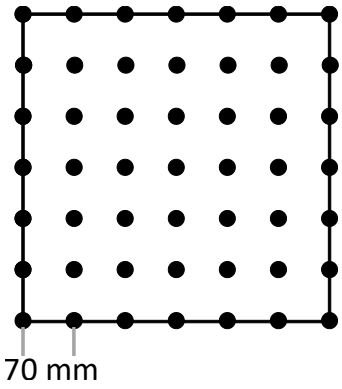

Figure 4.9: Grid of measurement points distributed on a panel.

During the experiment only the control with ON and OFF states was considered, for 99% and 0% duty cycle, respectively. The ESD was estimated according to the procedure, described in Section 3.5. A comparison of mean ESD, calculated from every point on a measured grid, for both ON and OFF state is presented in Figure 4.10.

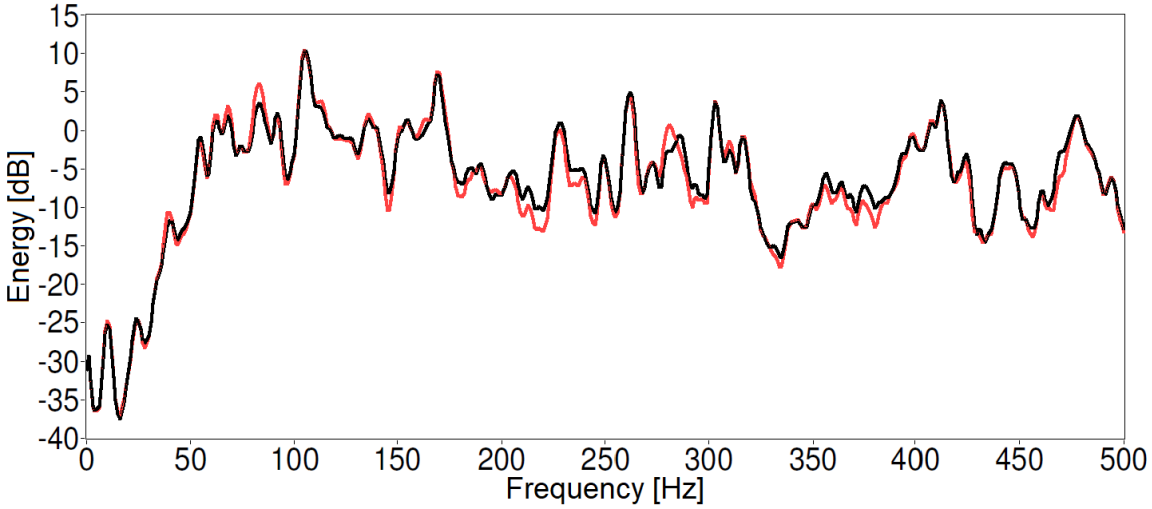

Figure 4.10: Mean ESD of measured vibration for ON (red) and OFF (black) states.

It was observed that vibration reduction may exceed 3 dB for particular frequencies. The presented characteristics are narrowed to 500 Hz as the frequency band of excitation signal. However, further investigation was conducted for the frequencies up to 250 Hz. The main goal is to select the modeshapes (Section 2.2.2) that will be used in analysis of energy distribution along the radiating panel. Due to the low density of grid of measurement points only four modeshapes were considered (Fig. 4.11): 4^{th} at 91 Hz, 5^{th} at 104 Hz, 11^{th} at 163 Hz, and 12^{th} at 187 Hz.

For every measurement point in ON state the energy distribution on panel was presented as a color map. For every modeshape the areas of nodes and anti-nodes are clearly separated. The red and purple colors are corresponding to the highest and the lowest values of energy, respectively. On every presented color map a contour of corresponding, simulated modeshape (Fig. 2.3) was transparently overlayed.

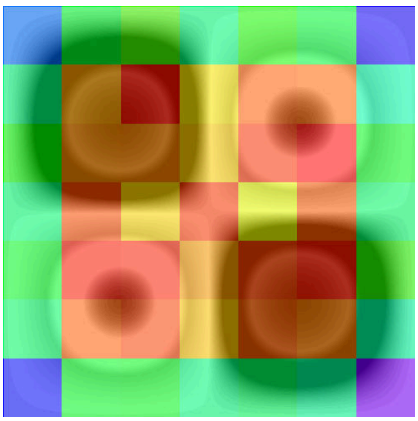

(a) Energy distribution for the 4^{th} mode.

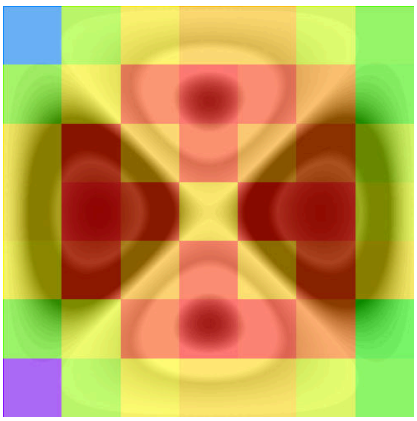

(b) Energy distribution for the 5^{th} mode.

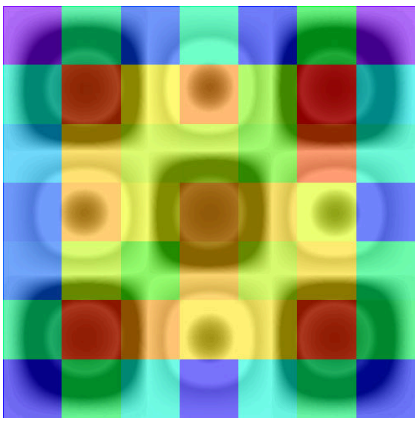

(c) Energy distribution for the 11^{th} mode.

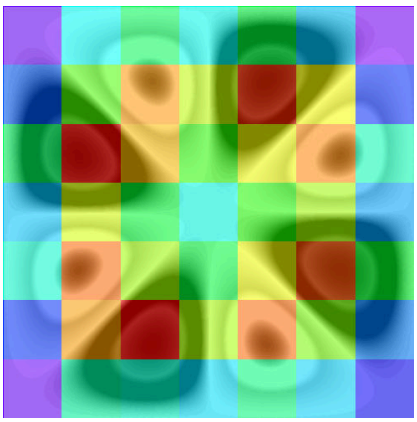

(d) Energy distribution for the 12^{th} mode.

Figure 4.11: Energy distribution on panel presented as a color map, for ON state, for the four selected modes with contours of corresponding, simulated modeshapes.

In Figure 4.11 only the ON state was presented to compare the simulation with measurements. The differences of vibration energy between the ON and OFF states on the color maps were subtle, and difficult to distinguish. To better visualize such variations, these differences are presented as the numerical values (Tab. 4.1 — 4.4). The negative values, marked with green color mean the vibration reduction. The x and y values are coordinates of grid points, with origin of coordinate system placed in the bottom-left corner of the vibrating part of a panel.

Table 4.1: Differences of energy values between ON and OFF states for the 4^{th} mode.

0.42	0.55	-2.40	-1.74	-0.47	-0.08	-0.08	0.13
0.35	0.53	1.15	0.67	1.00	-1.16	-1.12	-0.85
0.28	-0.77	-0.49	-0.91	-2.44	-2.90	2.45	-0.94
0.21	-1.61	-2.24	-1.71	-1.69	-2.43	-1.56	-1.85
0.14	0.45	1.21	1.27	-2.42	0.15	-0.57	-0.53
0.07	-0.86	0.25	2.85	0.62	0.45	-1.33	0.91
0	0.70	0.57	1.13	-0.15	-0.60	-1.91	-1.70
y/x	**0**	**0.07**	**0.14**	**0.21**	**0.28**	**0.35**	**0.42**

For the 4^{th} mode it was observed that the vibration is reduced mainly in the central point of the panel, in the areas of nodes and near the clamping frame (at the edges). In the areas of anti-nodes the vibration is mainly magnified, however, in these places the reduction was observed as well.

Table 4.2: Differences of energy values between ON and OFF states for the 5^{th} mode.

0.42	0.80	0.83	1.44	1.47	1.58	2.13	-0.89
0.35	1.35	-1.19	0.27	0.58	0.88	-1.16	-1.25
0.28	0.62	0.55	-0.75	-0.54	-0.46	-0.11	0.26
0.21	1.35	1.38	1.23	-2.69	1.55	1.33	1.13
0.14	1.51	1.50	-0.04	0.81	-0.26	0.50	0.05
0.07	1.39	1.90	0.21	0.40	1.02	0.89	0.69
0	-0.26	0.09	0.70	0.21	0.22	0.02	-0.03
y/x	**0**	**0.07**	**0.14**	**0.21**	**0.28**	**0.35**	**0.42**

For the 5^{th} mode it was observed that the vibration is reduced mainly in the panel's diagonals — where the areas of nodes are, with the highest reduction in central point of the panel. In the opposition to nodes — in places of anti-nodes the vibration magnification was observed.

Table 4.3: Differences of energy values between ON and OFF states for the 11^{th} mode.

0.42	1.93	0.75	-0.03	-1.02	1.70	1.51	-0.45
0.35	2.27	2.19	1.13	1.12	3.12	2.08	1.13
0.28	4.11	2.98	-0.56	2.58	0.72	1.57	-2.05
0.21	-5.54	-1.04	4.19	0.31	-0.14	1.06	0.20
0.14	1.83	2.40	-0.23	1.24	-1.48	-0.41	-5.11
0.07	2.33	0.75	3.13	0.44	2.81	1.15	1.86
0	3.15	1.93	1.09	-0.77	0.00	-0.33	-1.45
y/x	**0**	**0.07**	**0.14**	**0.21**	**0.28**	**0.35**	**0.42**

For the 11^{th} mode the vibration is reduced mainly for the nodes and for only one anti-node. No significant relation between the placements of the points on a grid and vibration reduction or magnification was observed.

Table 4.4: Differences of energy values between ON and OFF states for the 12^{th} mode.

0.42	-3.79	1.30	1.11	2.12	2.84	-1.69	1.77
0.35	5.07	4.86	0.45	-0.52	0.34	-3.63	0.73
0.28	-0.19	0.62	-2.20	-4.37	0.55	-1.08	1.71
0.21	-0.80	-1.21	-2.48	-3.80	1.26	0.71	1.28
0.14	3.65	2.15	-0.50	3.17	-3.06	-0.43	-0.43
0.07	2.87	-5.21	1.67	0.89	2.40	-0.57	-0.84
0	-0.07	-1.08	4.28	0.58	-0.03	-4.04	-2.59
y/x	**0**	**0.07**	**0.14**	**0.21**	**0.28**	**0.35**	**0.42**

For the 12^{th} mode the vibration is reduced mainly in the panel's diagonals and near the perpendicular lines passing through the central point of the panel — in the areas of nodal lines. For most anti-nodes areas, the vibration is magnified. The main conclusion drawn from the analysis is that the vibration reduction is observed mainly in areas of nodes, while the amplitudes in anti-nodes are magnified. It could mean that for the central, single couple the energy from nodal lines is cumulated in anti-nodes. However, the grid of measurement points should be more dense, and the number of investigated modes should be higher to confirm this theory. It is also worth mentioning that the presented research was preliminary and the results can be improved, by the use of a different method for a more stiff assembly of coil on the incident panel. Bending of the mounting element when the coupling force is high may affect the system similarly to spring mounted between the coil and radiating panel, which is undesirable.

4.2.4 Vibration damping using five couplings

The next experiment was a continuation of research performed for the single coupling. As stated before, the efficiency of solenoid could be improved by using a stiffer type of mounting element for the coil. In this research the five electromagnetic couplings were used. The placement of the solenoids was dedicated to low-frequency (i.e. up to 100 Hz) modes with simple shapes. However, the frequency band up to 500 Hz was investigated. The four elements were mounted in the places of anti-nodes of the 4^{th} mode (Fig. 2.3), and a fifth element was mounted in the center of the panel (Fig. 4.12).

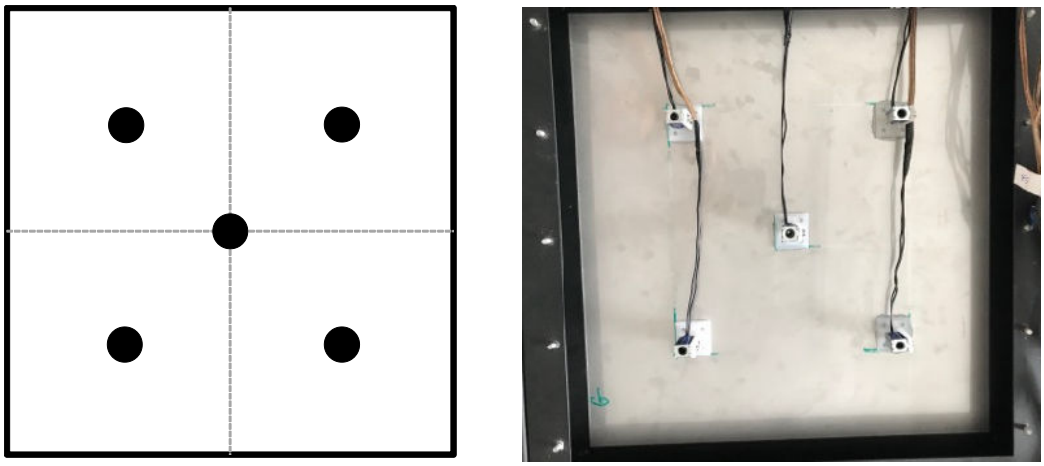

(a) Placement of the solenoids. (b) Coils attached on the incident panel.

Figure 4.12: Placement of electromagnetic couplings and attachement of the coils.

The new mounting elements for coils were designed and prepared, using 3D printing technology (Fig. 4.13). Moreover, the coils distances from the incident panel can be adjusted. The cores were attached to 1 mm thin brass plates (Fig. 2.6).

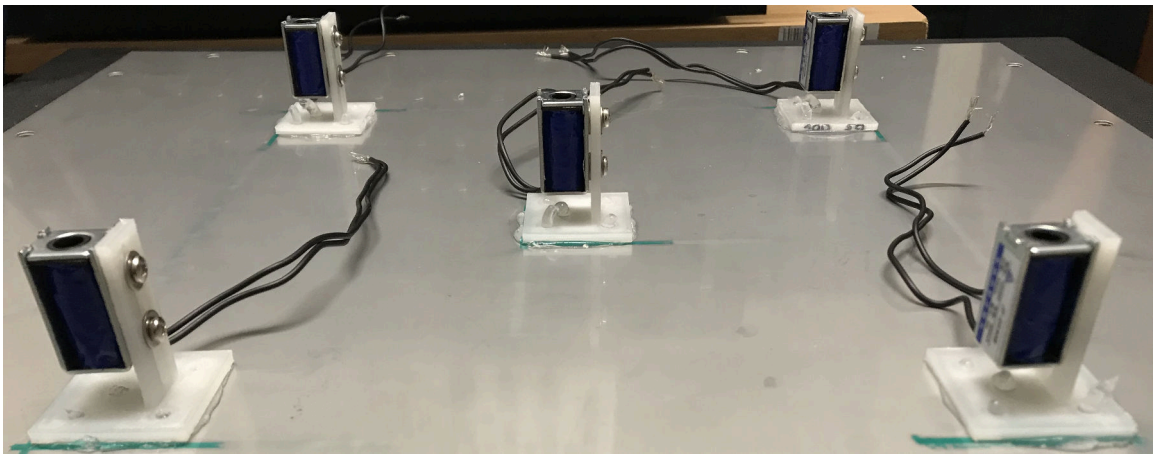

Figure 4.13: Enlargement of the incident panel with attached coils.

The laboratory setup is based on the rigid frame casing with a double-panel structure, coupled with five electromagnetic elements (Fig. 4.14). The investigated structure is excited to vibration using an internal active loudspeaker emitting an uncorrelated random signal, band-limited to 500 Hz, with a constant PSD. The source of the signal was DDS generator. Vibration of a double-panel was measured using MFC elements, connected to PCI-6289 DAQ card, through the dedicated terminal panel. In the experiment an isotropic steel panel with MFC elements was used (Fig. 3.1). The force, generated by the solenoid is set by the changing of the duty cycle of PWM signal using myRIO platform. The application for data acqusition, processing and generation of the PWM signal was developed in LabVIEW.

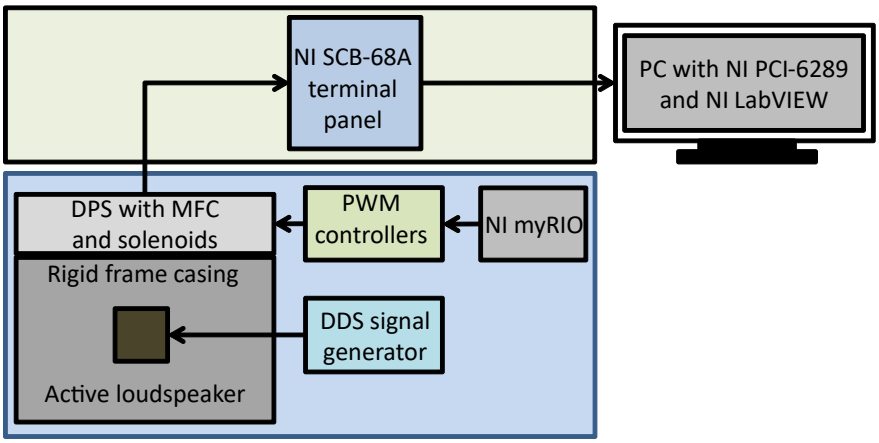

Figure 4.14: Scheme of measurement and control system for a double-panel structure with five electromagnetic couplings.

A comparison of ESD of measured vibration for every MFC element, and different numbers of activated couplings: one (in the central point of panel), four (in every corner) or five (all of the elements) was performed (Fig. 4.15). The analysis was conducted up to 500 Hz. Every pattern is divided into five areas, representing estimated ESD for duty cycle equal to 0%, 25%, 50%, 75%, and 99%, respectively, starting from the left side. The rows contain the following MFC elements, and the columns represent the number of activated couplings. Due to the significant changes in values of energy for different cases, the color map on particular pattern was rescaled to the highest value of energy, estimated in this case, e.g. MFC3, five solenoids. Thus, every single pattern should be analysed separately. The main goal of the presented results is to analyse, how the combinations of coupling numbers and duty cycle values impact on the energy dispersion in the investigated frequency range. The red and purple colors represent the highest and the lowest energy values, respectively.

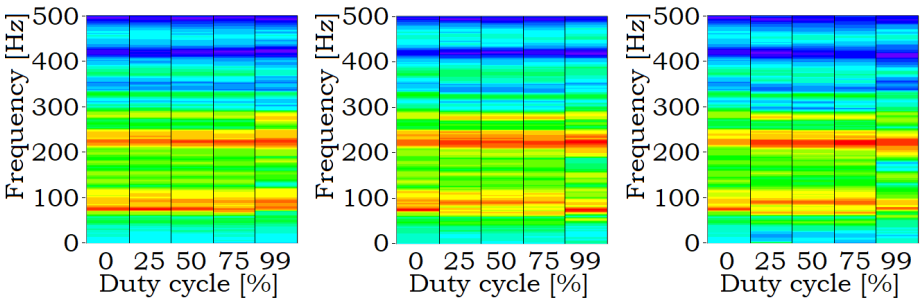

MFC1, one solenoid. MFC1, four solenoids. MFC1, five solenoids.

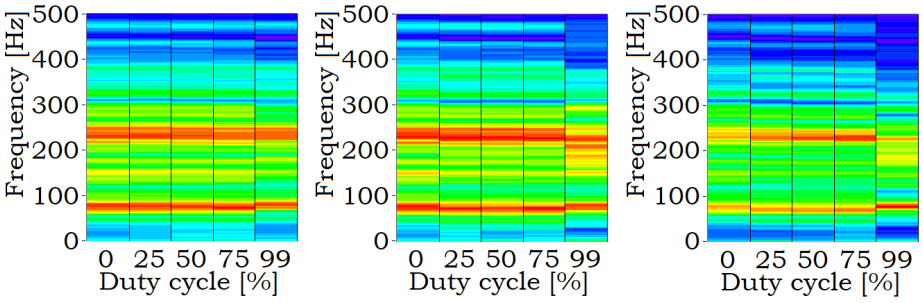

MFC2, one solenoid. MFC2, four solenoids. MFC2, five solenoids.

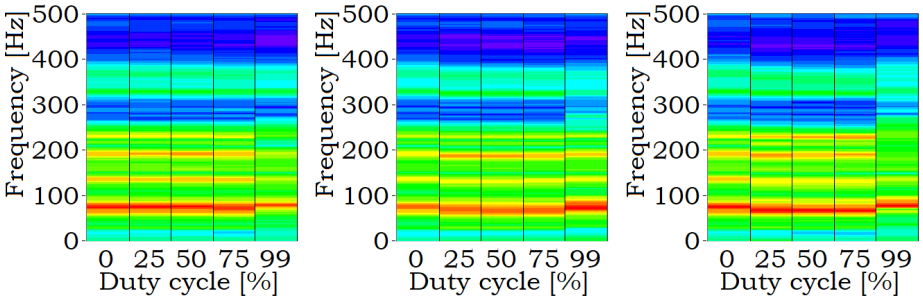

MFC3, one solenoid. MFC3, four solenoids. MFC3, five solenoids.

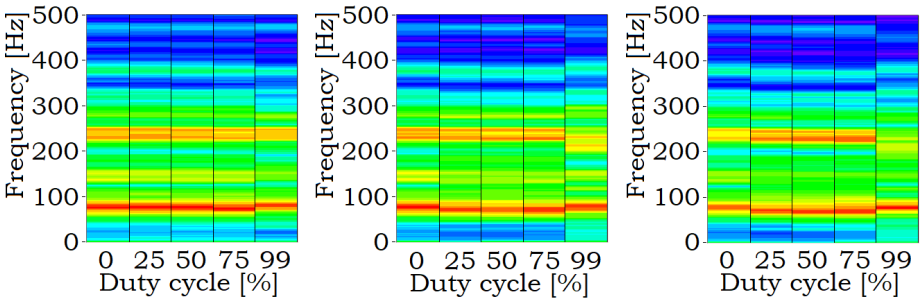

MFC4, one solenoid. MFC4, four solenoids. MFC4, five solenoids.

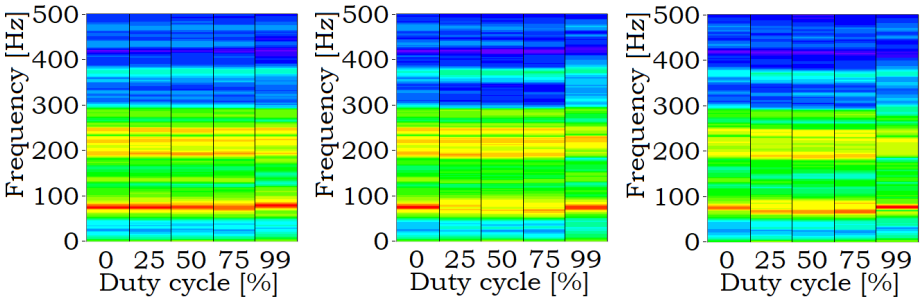

MFC5, one solenoid. MFC5, four solenoids. MFC5, five solenoids.

Figure 4.15: Frequency patterns generated from values of vibration energy for every MFC element, and different combinations of coupling numbers.

For higher clarity the results were summarized for every MFC element separately, where every point represent one, four and five activated couplings, respectively.

MFC1:

- for the one activated coupling the results were similar for every value of duty cycle, except 75%, where significant energy reduction was observed around 75 Hz,
- for the four activated couplings a magnification of vibration amplitude was observed for 99% duty cycle, especially around 75 Hz and 220 Hz. However, around 190 Hz vibration was reduced significantly. Setting a value of 25%, 50% and of the 75% duty cycle provide vibration reduction between 70 Hz and 110 Hz, and magnification of vibration amplitude between 200 Hz and 300 Hz,
- for the five activated couplings a significant decrease of energy value was observed for 99% duty cycle around 75 Hz, and between 100 Hz and 200 Hz, with the most significant decrease around 220 Hz. Setting a value of 25%, 50% and 75% of the duty cycle given similar results, however, with energy dispersion between 70 Hz and 110 Hz, and with efficiency improvement below 50 Hz.

In the majority of cases vibration can be reduced between 70 Hz and 110 Hz, however, with significant deterioration of efficiency of damping between 200 Hz and 300 Hz. The most efficient combination is four activated couplings with 75% duty cycle.

MFC2:

- for the one activated coupling setting a value of 25%, 50% and 75% of the duty cycle given results similar to the case with deactivated coupling. The maximal duty cycle value slightly improved vibration reduction in the whole frequency band,
- for the four activated couplings the vibration was damped slightly in whole frequency band, when the duty cycle was set to 25%, 50% or 75%. The maximal duty cycle value provides energy dispersion above 150 Hz and slight vibration damping below 75%,
- for the five activated couplings it was observed that every value of duty cycle worsen the efficiency of vibration damping.

In the majority of cases, vibration amplitudes stay on a similar level, except slight energy reduction for one coupling with 99% duty cycle, high dispersion of energy for the four couplings with 99% duty cycle, and the last case, where every value of duty cycle worsens the efficiency of vibration damping. The most efficient combination is one coupling with 99% duty cycle.

MFC3:

- as for the MFC2, the maximal value of duty cycle combined with the one coupling significantly improves vibration reducion, and the other values of duty cycle given results similar to the case with deactivated coupling,
- for the four activated couplings, a worsening of vibration reduction was observed for every value of duty cycle,
- for the five activated couplings a significant vibration reduction was observed from 50 Hz to 250 Hz when the duty cycle is set to 99%. The other values of duty cycle allow to reduce the vibration slightly.

In the majority of cases, vibration amplitudes stay on the similar level, except significant energy reduction for one and five couplings with 99% duty cycle, and the case with four couplings, where every value of duty cycle worsens the efficiency of vibration damping. The most efficient combination, as before, is one couplings with 99% duty cycle.

MFC4:

- for the one activated coupling it was observed that setting a value of 25%, 50% and 75% of the duty cycle given results similar to the deactivated solenoid. However, the maximal value of duty cycle provides vibration reduction in the whole frequency band,
- for the four activated couplings it was observed that for the maximal value of duty cycle the efficiency of vibration reduction is on a similar level as for deactivated couplings. However, the vibration reduction for other cases is slightly improved,
- for the last case it was observed that every value of duty cycle worsen the vibration damping efficiency. However, the 99% duty cycle improved the vibration damping above 150 Hz.

In the majority of cases vibration amplitudes stay on the same level, except the duty cycle set to 99% with significant energy reduction for one coupling, and with the last two cases, where the efficiency of vibration damping is worsens. The most efficient combination is one coupling with 99% duty cycle.

MFC5:

- for the one activated coupling the results are similar for all of the cases with all of the duty cycle values, except 99%, where vibration reduction is worsened up to 100 Hz and improved above this frequency,
- for the four activated couplings setting a value of 25%, 50% and 75% of the duty cycle significantly improve vibration damping efficiency up to 190 Hz and above 300 Hz. In the case with the maximal duty cycle value, the amplitude of vibration was magnified in almost whole investigated frequency range,
- for the five activated couplings it was observed that every value of duty cycle worsen the vibration damping efficiency — especially, the 99% duty cycle around 75 Hz.

For the last MFC element vibration remained on a similar level for the one coupling. Using four or five elements, vibration can be damped or magnified, respectively. The most efficient combinations are four couplings with 50% and 75% duty cycle.

After the analysis two main conclusions can be drawn:

- setting a value of 25%, 50% and 75% of the duty cycle is usually not effective. It can result from the coupling element characteristics (Fig. 4.3), where the rapid increasing of the force can be observed above 80% duty cycle, independently on parameters,
- for almost all of the MFC elements the most efficient combination was one coupling with a 99% duty cycle. This duty cycle value, combined with a higher numbers of solenoids usually worsen the vibration damping efficiency. This is because these elements cannot absorb or dissipate the energy, but by the coupling of the panels it is possible to transfer the energy into the areas, that are not covered by measurement elements. Consequently, if the amplitude of vibration will be reduced in one area, it will be also magnified in the other parts of the panel. With the use of higher number of coupling elements, the smooth dispersion of energy on the panel's surface is more difficult, and the higher amount of energy is cumulated in narrower areas, which increase the amplitude of vibration locally.

The investigation was extended by analysis of maximal energy values (Tab. 4.5) and mean energy values (Tab. 4.6) in the frequency range up to 500 Hz for every combination of duty cycle value and number of couplings. The maximal values of vibration reduction are marked in green, while the worst cases are marked in red. Additionally, the best combination for every MFC is marked by bold font.

Table 4.5: Maximal energy values obtained on MFC elements, depending on the number of coupling elements and duty cycle of PWM signal, up to 500 Hz.

Couplings	Duty cycle	MFC1	MFC2	MFC3	MFC4	MFC5
1	0%	18.68	16.72	25.44	19.81	21.68
	25%	19.48	16.76	25.99	19.95	21.94
	50%	18.09	16.88	25.36	20.21	20.21
	75%	17.86	18.21	25.15	20.43	18.69
	99%	17.98	16.42	**23.19**	19.57	21.42
4	0%	18.68	16.72	25.44	19.81	21.68
	25%	18.34	16.68	24.15	18.49	15.61
	50%	17.95	16.87	24.16	**17.26**	**14.82**
	75%	**17.48**	17.23	25.01	18.40	15.32
	99%	19.08	**15.99**	28.55	18.75	20.49
5	0%	18.68	16.72	25.44	19.81	21.68
	25%	19.85	19.76	25.61	20.26	18.93
	50%	20.10	20.69	25.54	21.45	19.95
	75%	20.97	21.15	25.90	21.49	21.42
	99%	20.20	22.70	25.87	22.71	25.00

It was observed that the highest vibration reduction of ESD amplitude is achieved for the different values of duty cycle, dependant on the number of couplings. The most efficient combinations were:

- for the single coupling: 75% duty cycle for MFC1 and MFC5, and 99% duty cycle for MFC2 — MFC4,
- for the four couplings: 25% duty cycle for MFC3, 50% duty cycle for MFC4 and MFC5, 75% duty cycle for MFC1, and 99% duty cycle for MFC2,
- for the five couplings: 0% duty cycle for MFC1 — MFC4, and 25% duty cycle for MFC5.

However, the highest vibration reduction (marked by bold font) was achieved for corner elements (MFC1, MFC2, MFC4 and MFC5) using four couplings, while the single coupling is efficient for the central element (MFC3).

Moreover, comparing each corresponding cell in Table 4.5 for different numbers of coupling (e.g. 50% duty cycle for MFC4 for each couplings combination) it was observed that the use of five couplings given the worst results for every value of duty cycle and MFC element, except the only 25% and 99% duty cycle for MFC3, and 25% and 50% duty cycle for MFC5.

Table 4.6: Mean energy values obtained on MFC elements, depending on the number of coupling elements and duty cycle of PWM signal, up to 500 Hz.

Couplings	Duty cycle	MFC1	MFC2	MFC3	MFC4	MFC5
1	**0%**	-0.80	-1.29	-0.81	-2.25	-2.10
	25%	-0.83	-1.44	-0.92	-2.39	-2.16
	50%	-0.78	-1.34	-0.90	-2.37	-2.12
	75%	-0.92	-1.57	-1.04	-2.47	-2.40
	99%	-1.42	**-3.33**	**-2.57**	**-3.91**	**-2.56**
4	**0%**	-0.80	-1.29	-0.81	-2.25	-2.10
	25%	-0.93	-1.63	-0.41	-2.29	-2.10
	50%	-0.98	-1.71	-0.49	-2.34	-2.23
	75%	-1.08	-1.82	-0.71	-2.36	-2.40
	99%	-1.29	-2.48	-0.40	-1.74	-1.89
5	**0%**	-0.80	-1.29	-0.81	-2.25	-2.10
	25%	-0.69	-1.52	-1.25	-2.10	-1.84
	50%	-0.67	-1.64	-1.75	-2.02	-2.09
	75%	-0.39	-1.52	-1.82	-1.81	-1.86
	99%	**-1.67**	-3.24	-2.21	-1.67	-1.84

It was observed that the highest vibration reduction is achieved for the different values of duty cycle, dependant on the number of couplings. The most efficient combinations were:

- for the single coupling: 99% duty cycle for all of the MFC elements,
- for the four couplings: 0% duty cycle for MFC3, 75% duty cycle for MFC4 and MFC5, and 99% duty cycle for MFC1 and MFC2,
- for the five couplings: 0% duty cycle for MFC4 and MFC5, and 99% duty cycle for MFC1 — MFC3.

Moreover, the highest vibration reduction (marked by bold font) was achieved for MFC2 — MFC5 using the single element with 99% duty cycle. For the MFC1 the

highest reduction was observed during the activation of five couplings with the maximal value of duty cycle.

Comparing each corresponding cell in Table 4.6, as before, for different numbers of coupling, it was observed that the use of five elements gave the worst results for MFC4, MFC5 and for MFC1 except 99% of duty cycle. The conclusion is that the suggested number of activated couplings and their placement depend on the preferred effect. The four corner elements gave the best results in reduction of the vibration, while the use of single, central coupling is dedicated to obtain the highest mean reduction of the vibration.

In Figures 4.16 — 4.20 a comparison between the best, the worst, and the case with deactivated couplings is presented, for each MFC element. The investigated frequency range was divided into the 0.1 Hz frequency bins, for which the energy was analysed individually for each combination of couplings and the value of duty cycle. By the best and the worst cases the combinations giving the lowest and the highest energy value are meant, for each frequency bin separately. The main idea behind this analysis is to show, how the vibration can be damped with the proper use of the electromagnetic couplings. However, the consequences of improper switching of the number of elements and the values of duty cycle are also shown.

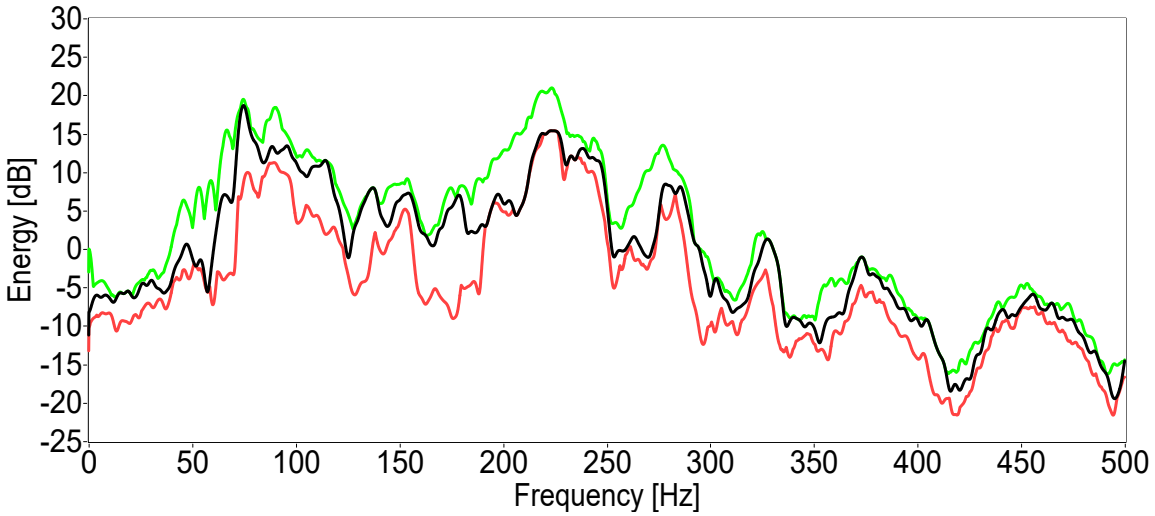

Figure 4.16: ESD of measured vibration for zero couplings (black), the best case (red) and the worst case (green) for MFC1.

For the MFC1 the vibration reduction compared to the zero coupling case is observed mainly in four frequency bands: up to 120 Hz, 140 — 240 Hz, 250 — 325 Hz, and 350 — 375 Hz. The maximal difference of energy value between the best and the worst cases is 15.25 dB for 177.4 Hz, with a 3.7 dB mean difference of energy value

between the best and the worst cases up to 500 Hz.

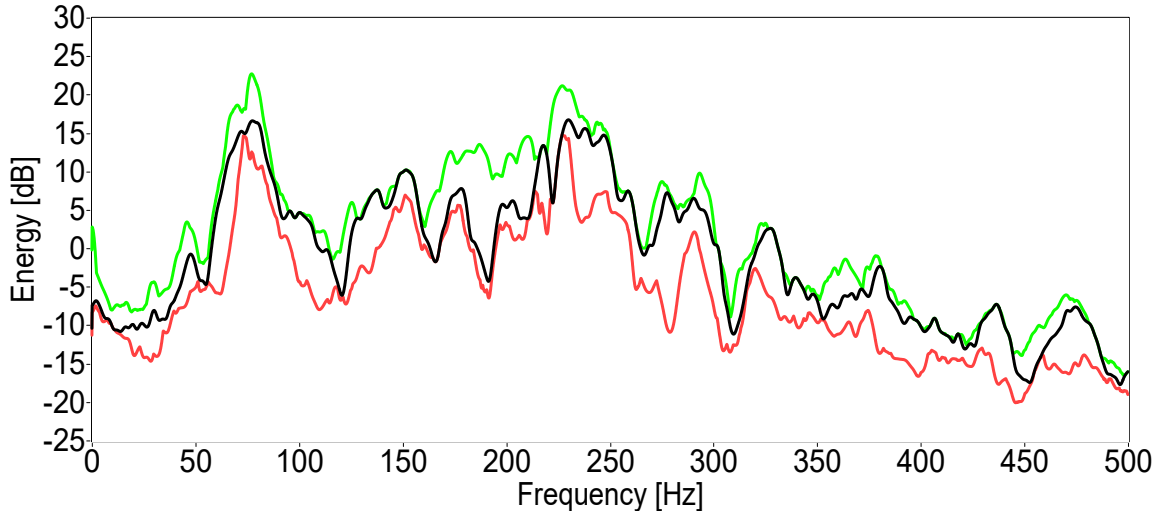

Figure 4.17: ESD of measured vibration for zero couplings (black), the best case (red) and the worst case (green) for MFC2.

For the MFC2 the vibration reduction in comparison to zero coupling case is observed mainly in six frequency bands: up to 125 Hz, 160 — 220 Hz, 225 — 250 Hz, 270 — 325 Hz, 350 — 375 Hz, and 450 — 475 Hz. The maximal difference of energy value between the best and the worst cases is 17.81 dB for 278.1 Hz, with a 4.64 dB mean difference of energy value between the best and the worst cases up to 500 Hz.

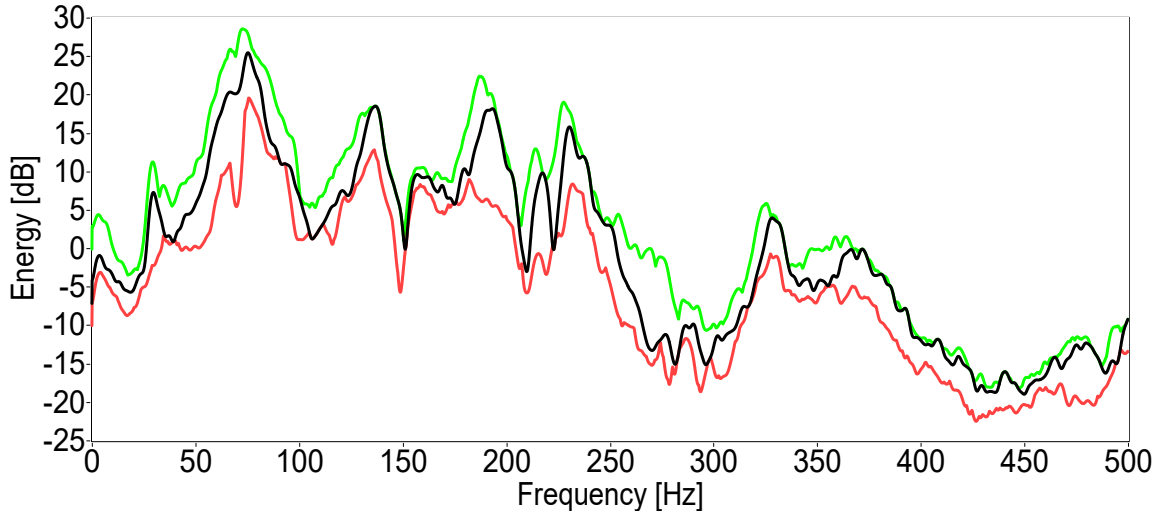

Figure 4.18: ESD of measured vibration for zero couplings (black), the best case (red) and the worst case (green) for MFC3.

For the MFC3 the vibration reduction compared to zero coupling case is observed mainly in five frequency bands: up to 130 Hz, 160 — 190 Hz, 200 — 240 Hz, 250 —

325 Hz, and 330 — 370 Hz. The maximal difference of energy value between the best and the worst cases is 14.71 dB for 69.8 Hz, with a 4.26 dB mean difference of energy value between the best and the worst cases up to 500 Hz.

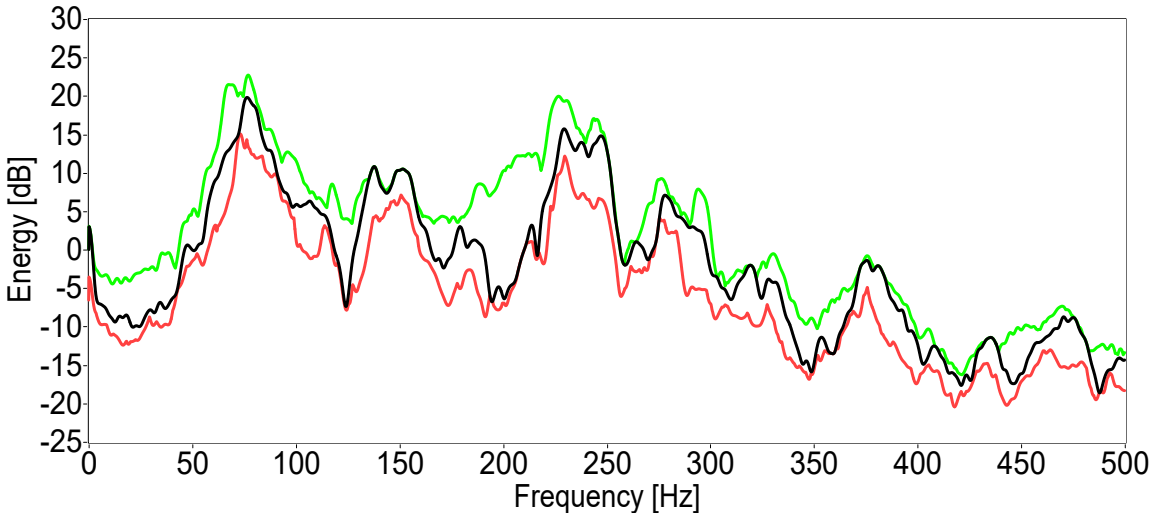

Figure 4.19: ESD of measured vibration for zero couplings (black), the best case (red) and the worst case (green) for MFC4.

For the MFC4 the vibration reduction in comparison to zero coupling case is observed mainly in six frequency bands: up to 125 Hz, 160 — 250 Hz, 260 — 375 Hz, 380 — 435 Hz, 440 — 475 Hz, and 480 — 500 Hz. The maximal difference of energy value between the best and the worst cases is 11.91 dB for 74.4 Hz, with a 3.31 dB mean difference of energy value between the best and the worst cases up to 500 Hz.

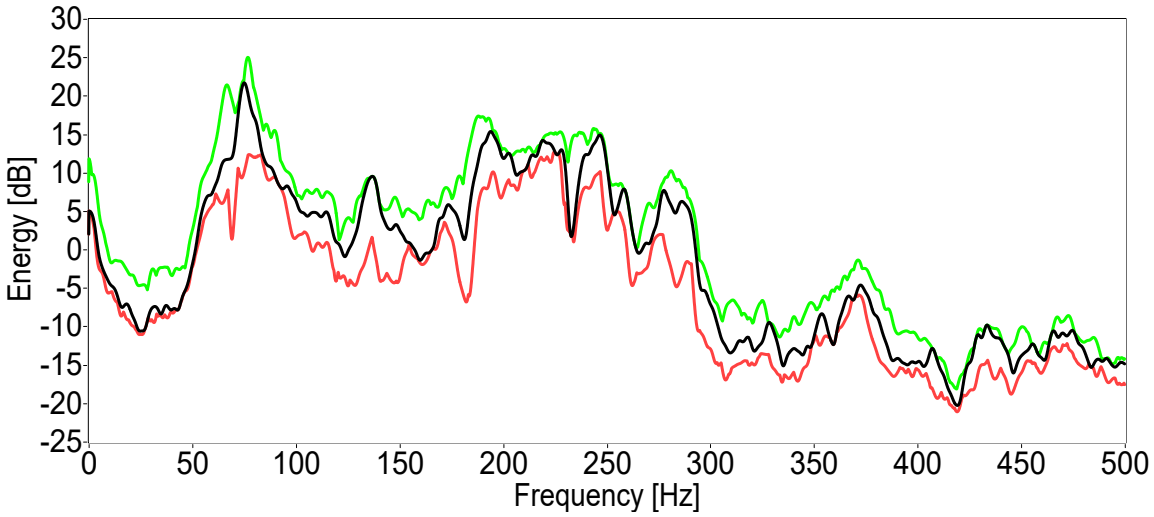

Figure 4.20: ESD of measured vibration for zero couplings (black), the best case (red) and the worst case (green) for MFC5.

For the MFC5 the vibration reduction in comparison to zero coupling case is observed mainly in five frequency bands: up to 135 Hz, 140 — 250 Hz, 265 — 435 Hz, 445 — 455 Hz, and 470 — 500 Hz. The maximal difference of energy value between the best and the worst cases is a 15.25 dB for 177.4 Hz, with a 3.70 dB mean difference of energy value between the best and the worst cases up to 500 Hz.

By the zero coupling case, setting a value of 0% of the duty cycle is meant. However, it should be taken into account that the additional masses of coils and cores are still bonded with incident and radiating panels, respectively. It may results in shifting of the resonant frequencies, and change of the mechanical properties, thus, the zero coupling case is different than the panels without any additional elements.

The approach of activation of the different numbers of couplings, with the different values of duty cycle is appropriate in the narrow band vibration response of the radiating panel. However, in the real object it should be taken into account that the measured vibration response is usually a wide band signal. Thus, the last analysis was conducted for the single configuration, compared with the zero coupling scenario. After the previous analysis a single coupling with 99% duty cycle was selected as the optimal configuration. The results of the comparison are presented in Figures 4.21 — 4.25.

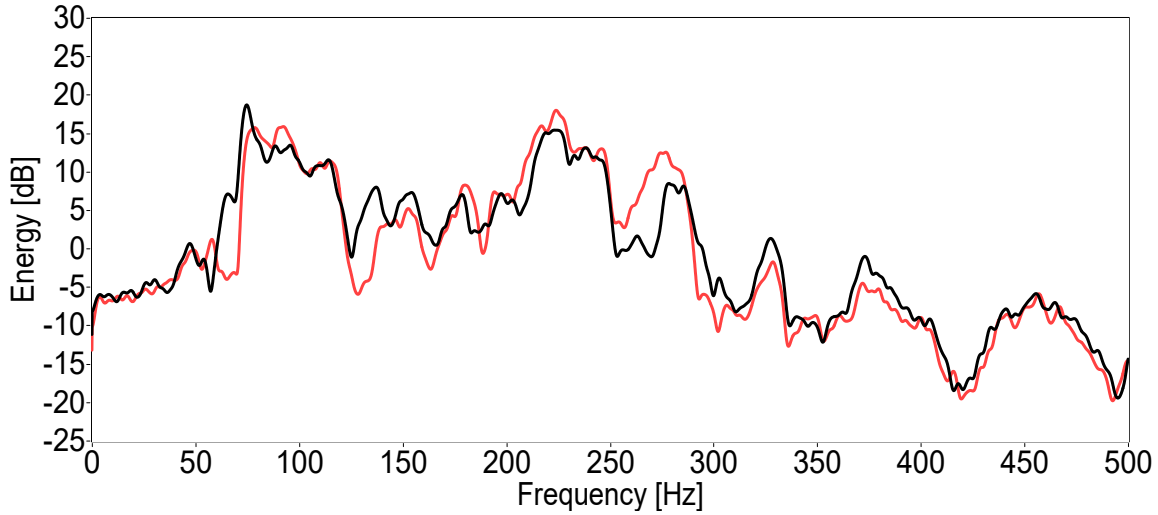

Figure 4.21: ESD of measured vibration for zero couplings (black), and one coupling (red) with 99% duty cycle of PWM signal, for MFC1.

For the MFC1, the vibration reduction was observed in the whole frequency range, except 75 — 100 Hz and 175 — 280 Hz. The maximal vibration reduction is 11.51 dB for 70.6 Hz.

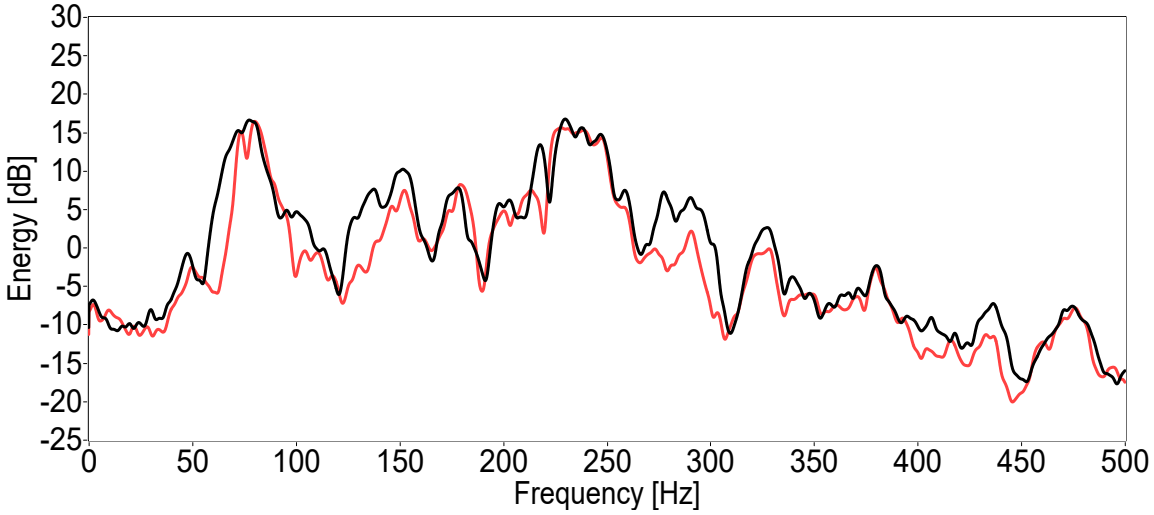

Figure 4.22: ESD of measured vibration for zero couplings (black), and one coupling (red) with 99% duty cycle of PWM signal, for MFC2.

For the MFC2, the vibration reduction was observed in the whole frequency range, with slight exceptions around 75 Hz, 175 Hz, 210 Hz, and 225 Hz. The maximal vibration reduction is 13.37 dB for 63.2 Hz.

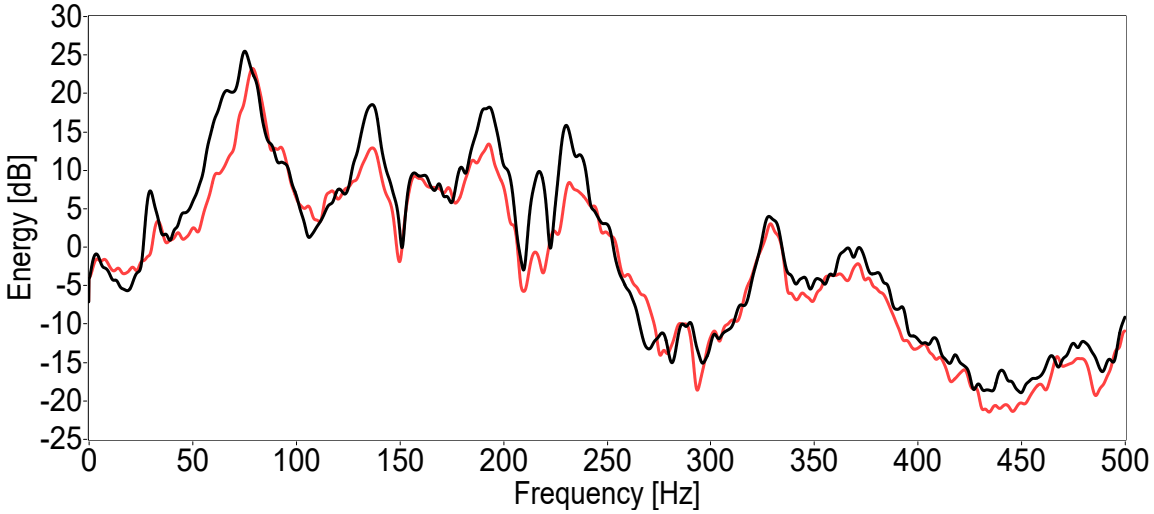

Figure 4.23: ESD of measured vibration for zero couplings (black), and one coupling (red) with 99% duty cycle of PWM signal, for MFC3.

For the MFC3, the vibration reduction was observed in the whole frequency range, except 5 — 30 Hz, 75 — 120 Hz, 250 — 270 Hz, and in some single frequencies. The maximal vibration reduction is 12.32 dB for 218.6 Hz.

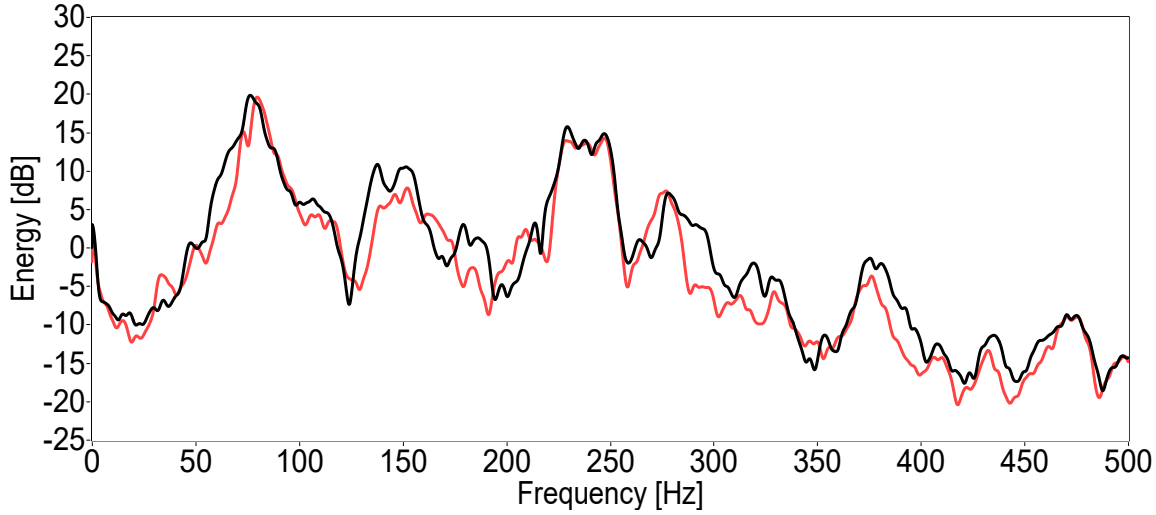

Figure 4.24: ESD of measured vibration for zero couplings (black), and one coupling (red) with 99% duty cycle of PWM signal, for MFC4.

For the MFC4, the vibration reduction was observed in the whole frequency range, except 30 — 45 Hz, 155 — 175 Hz, 190 — 210 Hz, 265 — 275 Hz and in some single frequencies. The maximal vibration reduction is 9.21 dB for 288.4 Hz.

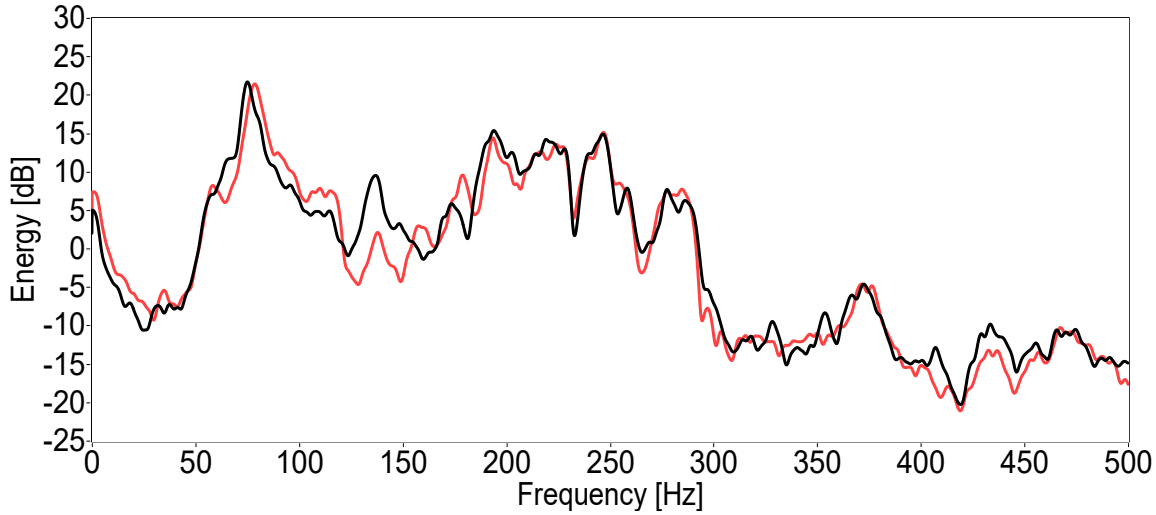

Figure 4.25: ESD of measured vibration for zero couplings (black), and one coupling (red) with 99% duty cycle of PWM signal, for MFC5.

For the MFC5, the vibration reduction was observed at around half of the investigated frequency range, especially in 60 — 75 Hz, 125 — 155 Hz, and 405 — 460 Hz. The maximal vibration reduction is 9.17 dB for 133.76 Hz.

It was observed that the use of single, central coupling mounted between two panels allows to reduce the structural vibration significantly. The results are also consistent

with the data presented on patterns (Fig. 4.15) and in Tables 4.5, 4.6. However, it should be taken into account that the energy is not dissipated, but transferred into the other areas of the panel's surface, where the amplitude of vibration will be magnified.

4.3 Modified Chladni's method

The results presented in Sections 4.2.3, 4.2.4 were promising. However, due to the insufficient density of grid of the measurement points, it was necessary to use the other method to investigate how the energy is transmitted through the panel's surface. Several methods can be distinguished:

- LDV/scanning LDV,
- high-speed vision camera,
- grid of accelerometers,
- SONAH,
- Chladni's method.

Advantages and disadvantages of every method are presented in Table 4.7 with the ✓and × symbols, respectively. However, not every disadvantage eleminates the use of the method in the further research. The crucial parameters are: resolution, cost, and measurement time. If the method does not follow those requirements, it is marked additionally with the red color.

Table 4.7: Advantages and disadvantages of the considered methods.

	LDV	**Camera**	**Accelerometers**	**SONAH**	**Chladni**
Resolution	✓	✓	×	✓	✓
Cost	✓	×	✓	×	✓
Robustness	✓	✓	✓	×	×
Contactless	✓	✓	×	✓	×
Freq. range	✓	×	✓	×	✓
Meas. time	×	✓	✓	✓	✓

In the LDV the sampling frequency is too low to visualize the modeshapes in sufficiently high resolution. As for sufficient resolution, it was assumed that the distance

between the measurement points on a square grid, covering the whole panel, is 2 cm. It gives a grid with 22 points × 22 points dimensions (484 points in total). Even the use of scanning LDV [94] with 2 Hz sampling frequency reduces the time of measurement to 4 minutes, while the expected time should not exceed a half a minute. This time regime is due to the coil's overheating, mentioned in Section 4.2.3. The possible solution to reduce the measurement time is the use of continuous scanning LDV [95], where the data is acquired for the whole vector of points, instead of a single point. However, these devices are expensive and, thus, unavailable to use for this research.

The high-speed camera is widely used in modal analysis as an alternative approach to LDV. It was proven that it is possible to measure the structural vibration with vision devices as efficiently as with the use of LDV [96]. The most popular camera-based method used in measurement of the structural vibration is digital image correlation (DIC), beneficial due to its high resolution and time of measurement [97]. However, high-speed cameras are expensive, which eliminated this approach in further analysis.

The accelerometers are the most commonly used sensors in vibration measurement. However, to obtain sufficient resolution of visualization of the modeshapes it is necessary to use the high number of sensors. Such additional masses, mounted on the thin structure change its modal properties significantly and, thus, the measurements are not reliable.

SONAH can be found in literature as an alternative to LDV, and it is beneficial due to the time of measurement with a sufficient resolution of estimated modeshapes. However, it requires the use of high number of microphones and multi-channel data acquisition system, which makes it an expensive solution. However, it is possible to decrease the cost of the device by building it, e.g. as it was presented in Section 2.4. However, the SONAH algorithm is not implemented on the test stand yet, and the device was not used in further research.

Chladni's method is a well known scientific experiment, used in observation of the modeshapes of a planar, vibrating structures, proposed in 1781 by E.F.F. Chladni [98]. It is possible thanks to the bulk material cumulating in the areas of nodal lines during the excitation of the investigated object. The classic version of the experiment is based on a rigid connection between the source of excitation and a vibrating single panel with free boundary conditions. The modified version of this method was described by Rzepecki et al. [90] and the full analysis is presented (Section 4.3.1, 4.3.2).

4.3.1 Electromagnetic couplings case

In the modified version of Chladni's method, a single panel was replaced by a double-panel structure mounted, as in the previous experiment, on the rigid frame (Fig. 4.26). Therefore, the boundary conditions are fully clamped, contrary to free boundary conditions in the classic approach. The next difference is source of the excitation, placed parallel to the structure with the 100 mm distance from the incident panel, without any mechanical connection.

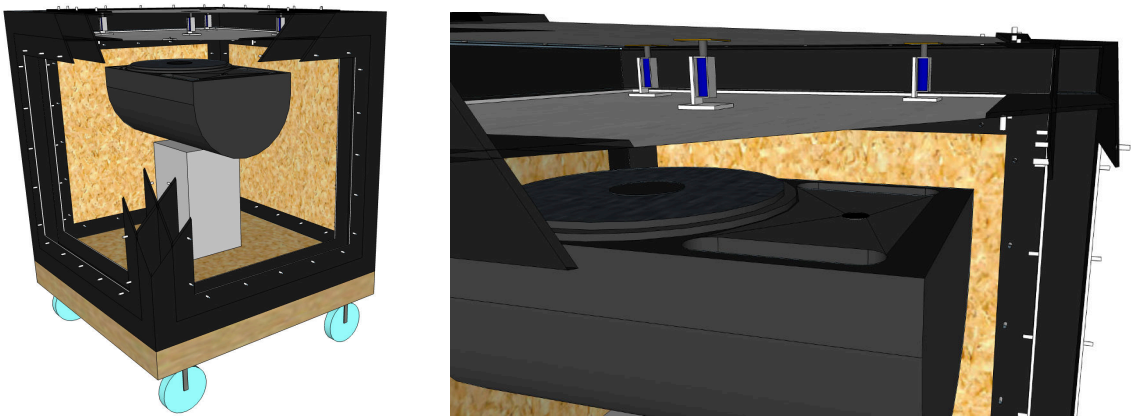

(a) View of oblique section of casing.

(b) View of a double-panel structure and loudspeaker.

Figure 4.26: Schemes of casing configuration used in experiment.

The laboratory setup (Fig. 4.27) is based, as previously stated, on the rigid frame casing with a double-panel structure, placed horizontally, as the top wall of the casing.

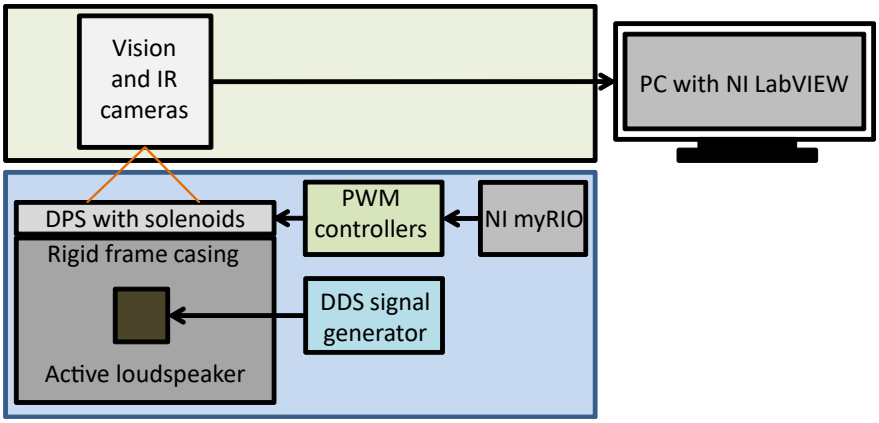

Figure 4.27: Scheme of measurement and control system for modified Chladni's experiment.

The panels are coupled with five electromagnetic elements. The investigated structure is excited to vibration using internal active loudspeaker emitting tonal signals with selected frequencies. The source of the signal was a DDS generator. The modeshapes obtained during the experiment are acquired with the use of vision and IR cameras. The force generated by the solenoid is set by changing the duty cycle of PWM signal using myRIO platform. The application for data acqusition, processing and generation of the PWM signal was developed in LabVIEW.

The first experiment was performed for a single frequency, for the four different cases: without activation of couplings, with a single centrally placed coupling, with four couplings localized in corners, and for five couplings (all elements activated). A double-panel structure was excited to vibration by 90 Hz tonal signal (Fig. 4.28), which corresponds to the 5^{th} mode (Fig. 2.3).

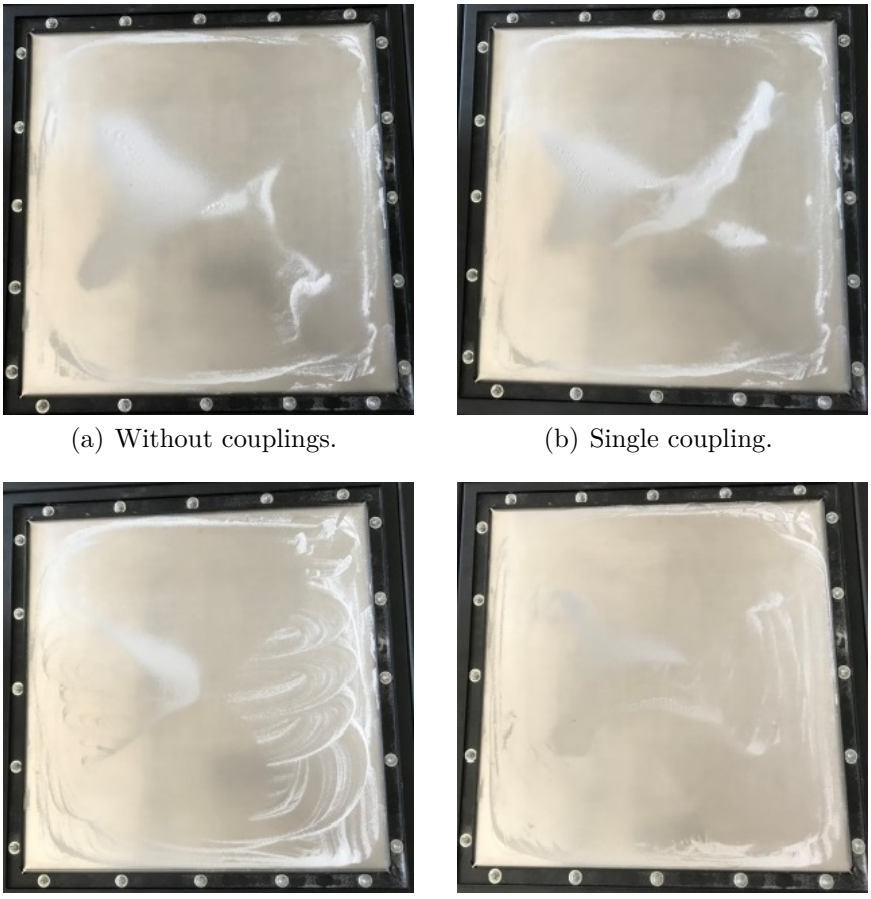

(a) Without couplings. (b) Single coupling.

(c) Four couplings. (d) Five couplings.

Figure 4.28: Vision images of modeshapes for 90 Hz with the different numbers of activated couplings.

The obtained results are difficult to interpret due to the light reflections in shining surface of the panel. To improve the clarity of results IR imaging was used (Fig. 4.29). The experiment was performed, as before, for 90 Hz without the activation of couplings. Different images types and filters were compared: vision image, RAW IR image, IR image with sharpening filter, and IR image with emboss filter. Both, the vision and IR images are acquired using the same device.

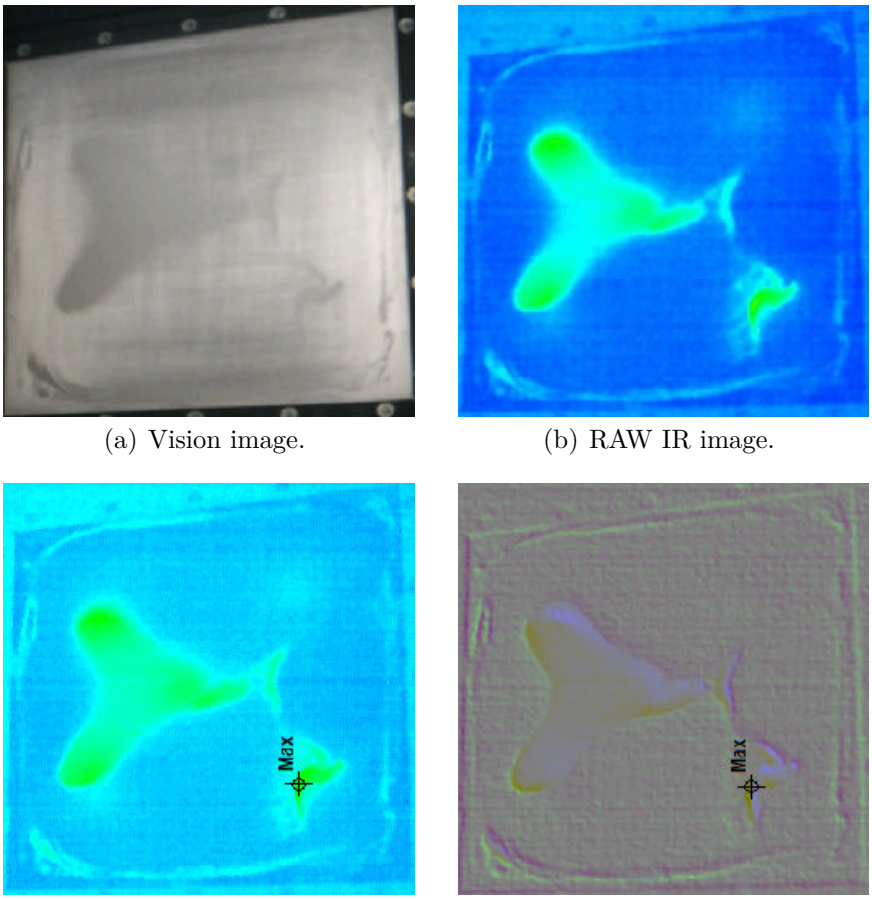

(a) Vision image. (b) RAW IR image.

(c) IR image with sharpening filter. (d) IR image with emboss filter.

Figure 4.29: Obtained modeshape presented with the use of different types of images and filters.

The vision image is blurred and difficult to analyse, however, the use of IR imaging brought out the contours of areas of nodal lines. The use of two examplar filters: sharpening and emboss, does not improve the quality of images significantly. Thus, the results of the next experiment were presented as RAW IR images (Fig. 4.30). The frequency of excitation signal and couplings combinations were the same as previous (Fig. 4.28).

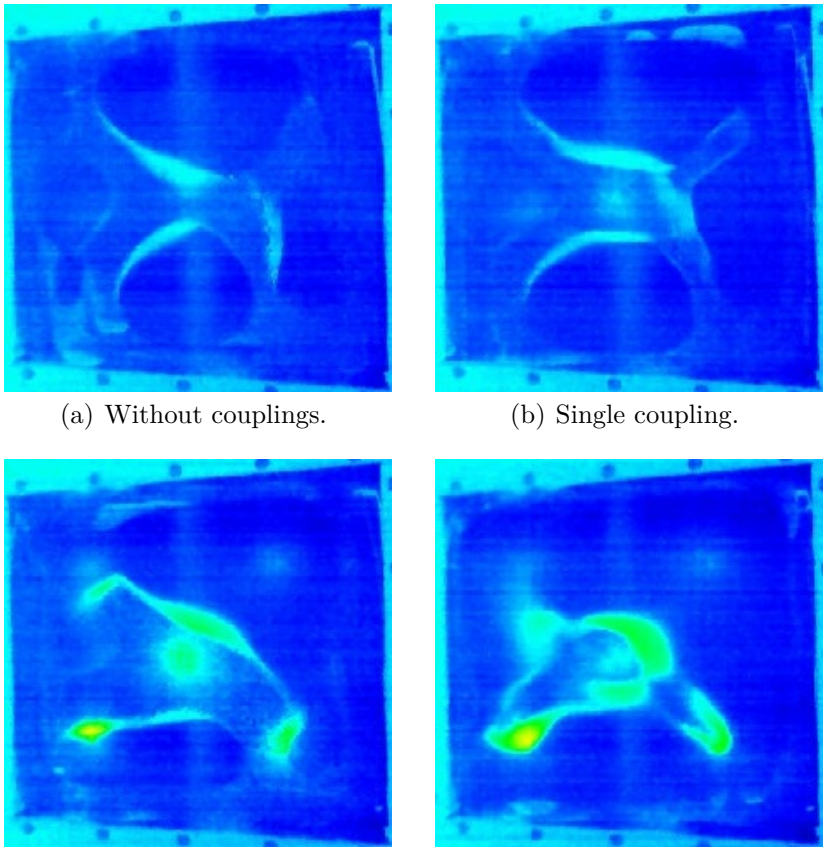

(a) Without couplings. (b) Single coupling.

(c) Four couplings. (d) Five couplings.

Figure 4.30: Modeshapes for 90 Hz, depending on number of activated couplings.

It was observed that the activation of a single coupling extends the size of the area of nodal lines in center of the vibrating panel, in a vertical direction. However, the obtained modeshapes are deformed, especially for the four and five activated elements. Moreover, it was observed that the temperature of the panel in places of coupling mountage increased. It was supposed that the overheating of coils was the reason for the problem. To confirm it, the maximal value of voltage was applied on the coil for 30 seconds, and the temperature of the coil was measured every 5 seconds (Tab. 4.8).

Table 4.8: Temperature of panel for 11 V coil supply voltage, depending on time.

Time [s]	**Temperature [°C]**
0	22.1
5	25.9
10	29.6
15	32.6
20	35.9
25	39.8
30	41.5

In 30 seconds the temperature increased by almost 20 °C, which means that the coils were overheated. Such a situation has influence on the efficiency of the elements, and may decrease the generated forces. It may be related with the observed deformations of the modeshapes obtained on IR images (Fig. 4.30). Therefore, in the next experiment the electromagnetic couplings were replaced by stiff, neodymium magnets. Moreover, due to the low quality of IR images, the further results were acquired using a vision camera, however, with the proper lighting to obtain higher quality.

4.3.2 Stiff couplings case

To avoid rapid fluctuations of temperature during the experiments, the stiff couplings were used. The couplings are built from the packets of ten 5 mm thick neodymium magnets (Fig. 4.31(a)). The couplings were placed inside a double-panel structure, as before, however, the corner elements were mounted in the places of anti-nodes of the 11^{th} mode (Fig. 4.31(b)), instead of the 4^{th} mode. To assure the stable positions of the couplings, additional magnets were placed outside both the radiating and incident panels.

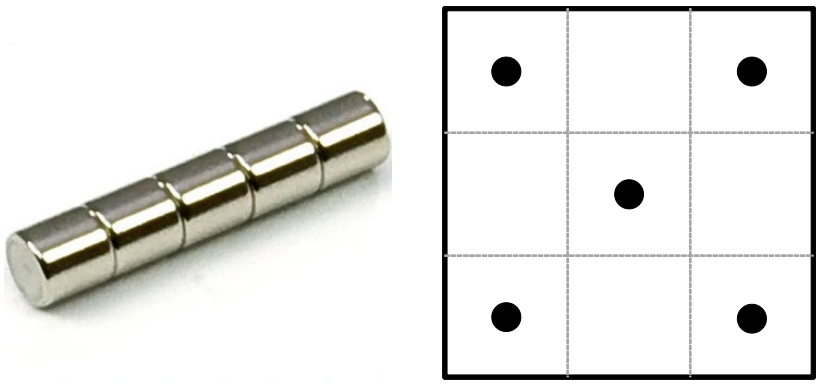

(a) (b)

Figure 4.31: Packet of neodymium magnets (a), and the placement of couplings on the panel (b).

The experiment was performed for the four different cases: without couplings, with a single centrally placed coupling, with four couplings localized in corners, and for five couplings (all elements between the panels). A double-panel structure was excited to vibration with the use of tonal signals with around 85 Hz, 150 Hz, and 200 Hz frequencies. The values slightly vary for every combination of couplings, because the boundary conditions changed after every coupling replacement. The frequencies correspond to 5^{th}, 13^{th}, and 14^{th} modes, respectively (Fig. 2.3).

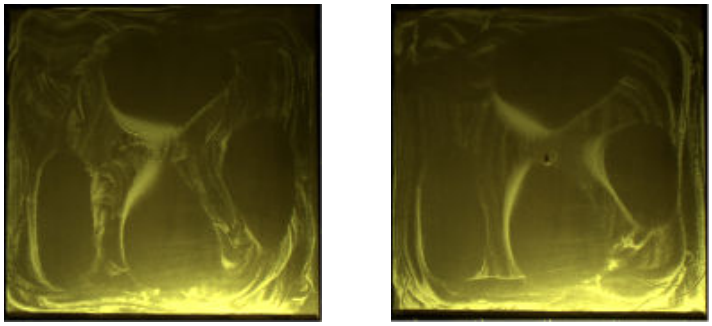

(a) Zero coup., 84.2 Hz. (b) One coup., 85.9 Hz.

(c) Four coup., 85.4 Hz. (d) Five coup., 85.8 Hz.

Figure 4.32: 5^{th} modeshape for different combinations of couplings.

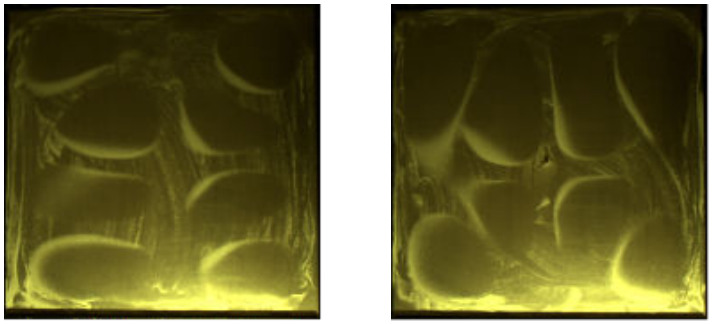

(a) Zero coup., 153.8 Hz. (b) One coup., 148.5 Hz.

(c) Four coup., 156.8 Hz. (d) Five coup., 160.9 Hz.

Figure 4.33: 13^{th} modeshape for different combinations of couplings.

For the 5^{th} mode it was observed that the use of a single coupling extends the size of the areas of nodal lines in the center of the vibrating panel, in a vertical direction. The obtained modeshapes are deformed, as before, however, only for the scenarios without couplings and with a single coupling. For the four elements the modeshape are more regular, and the diagonal areas of nodal lines are narrowed. The use of five elements extends the side anti-nodal areas, and central area of nodal lines.

In the case of the 13^{th} mode for a single coupling it was observed that the modeshape is rotated by a 90 degrees angle. It may result from unintentional rotation of the panel before the reassembly. It also indicates that the radiating panel is not perfectly isotropic. Moreover, the anti-nodal areas are expanded. For the four couplings the anti-nodal areas are narrowed, and the modeshape is more regular, and more symmetrical. The use of five elements, results in significant expanding and merging of the anti-nodal areas in a vertical direction.

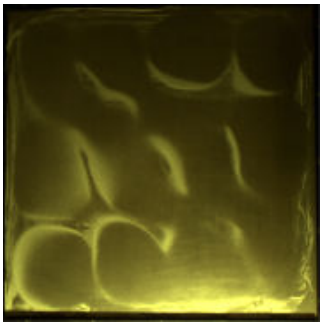

(a) Zero coup., 194.9 Hz.

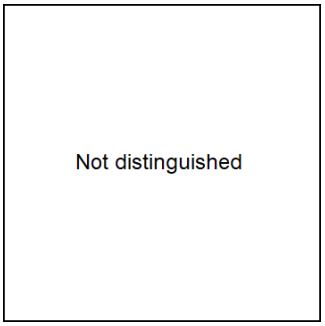

(b) One coup.

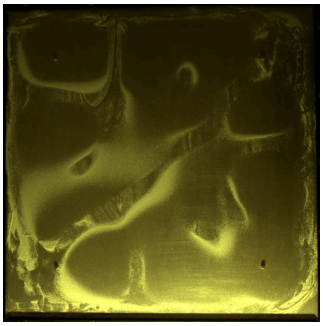

(c) Four coup., 196.2 Hz.

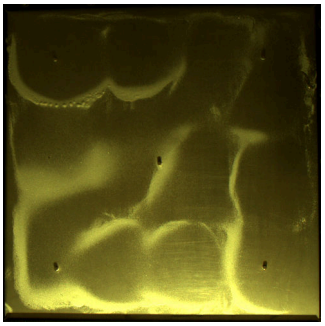

(d) Five coup., 199.4 Hz.

Figure 4.34: 14^{th} modeshape for different combinations of couplings.

The last modeshape is complicated and the explanation of influence of the coupling on the modeshape may not be unequivocal. For the first case the modeshape is rotated by a 90 degrees angle, which means that the panel was unintentionally rotated, or the neighboring (15^{th}) modeshape was obtained. The second modeshape cannot be distinguished. The use of four elements expand the anti-nodal areas, while the five elements

magnify the vibration significantly. It is visible especially in the areas, where the bulk material is granulated, e.g. in the top-left corner. The modified Chladni's method can be used as a preliminary analysis of the modeshapes of vibrating, planar structures, however, the method should not be considered in more precise investigations.

4.4 Discussion

In this Chapter the device casing with a double-panel structure was investigated. The proposed damper was implemented, based on the modified push-pull solenoid. The element was tested using the precise laboratory electronic scale. It allowed to investigate how the selected parameters influence the force generated by the solenoid.

In the first experiment, a single element was mounted between the panels, as the central coupling. The vibration of the radiating panel was measured using the LDV for a grid of 49, regularly distributed points. The data was used to estimate the ESD, and the energy distribution on the vibrating panel was additionally visualized for the selected modeshapes. The main conclusion was that the using of central coupling reduces the vibration in nodal lines, while the vibration in anti-nodes was magnified.

The second experiment was performed for the five elements, mounted in central point of the panels and in every corner (in places of anti-nodes of the 4^{th} mode). The vibration was measured using the five MFC elements, attached in the same places as thecouplings. The experiment was performed for the different combinations of the couplings and values of force, generated by the elements. The main conclusion was that the use of a single, central coupling gives the best results in reduction of both the mean and maximal values of vibration energy. However, the energy might be tranferred into the areas of the panel, not covered by the measurement elements. Thus, it was necessary to investigate the energy distribution on the whole vibrating panel.

Several methods of the multi-point vibration measurement were considered. However, it was decided to use the novel approach, by the modification of Chladni's method. The modeshapes were acquired as the vision and IR images. During the experiments the rapid fluctuations of temperature of the couplings were observed. Therefore, the electromagnetic elements were replaced by neodymium stiff couplings. The main conclusion is that the Chladni's method can be used as a preliminary method, but it is not possible to observe the energy distribution precisely. During the experiments it was also noted that the radiating panel is not perfectly isotropic.

Chapter 5

Magnetorheological vehicle suspension

5.1 Background

Vehicle suspension is the system including i.a. tires, springs, shock absorbers, and elements connecting sprung (vehicle body) and unsprung (wheels) masses. The main goal of vehicle suspension is to reduce the sprung mass movement, simultaneously with keeping maximal wheel contact with the road surface, to assure safe vehicle handling, especially in corners. During the years many types of vehicle suspensions were created. Such systems can be divided into the three main groups: passive, semi-active, and active. The passive suspensions have one damping characteristic, tuned to a specific vehicle, for obtaining a desired effect. Usually, it is a compromise between vehicle handling and attenuation of vibration propagated to the sprung mass. The most popular examples of passive suspensions are: leaf spring, coil springs, shock absorbers, and torsion bars [99]. Passive suspensions do not require an external power supply to work. In practice, semi-active suspensions are the passive systems with an infinite number of damping characteristics. In opposition to the passive systems, an external source of energy is required, however, only to change the properties of the suspension (e.g. stiffness). The most popular examples of semi-active suspensions are: conventional semi-active dampers, ER and MR dampers, and semi-active spring systems [100]. In active suspensions, an external source of energy is used to control the actuators, in order to obtain an expected response of the system upon excitation, i.e. contact of vehicle with the obstacle on the road. The most popular examples of active suspensions are: conventional active actuators, hydraulic and pneumatic actuators, and electromagnetic

actuators [101].

The MR vehicle suspension was described, with the author's contribution, in context of different approaches to estimation of the vertical suspension velocity. In this dissertation, a quarter vehicle model is assumed. The idea of the use of LVDT sensors in estimation of the vertical suspension velocity is described in [102, 103]. Moreover, driver's comfort was analysed during the experiments carried out on the test route [26], as well as driving safety in the laboratory environment [104]. This Chapter presents a research included mainly in the papers [102, 103], and partially in [26, 104].

5.2 Vehicle suspension modeling

The vibration of the investigated vehicle can be modeled using a multiple input, multiple output (MIMO) dynamic system, described in a general way using a diagram (Fig. 5.1) [105]. As the source of the vibration only the suspension movement inducted by the road roughness was taken into account.

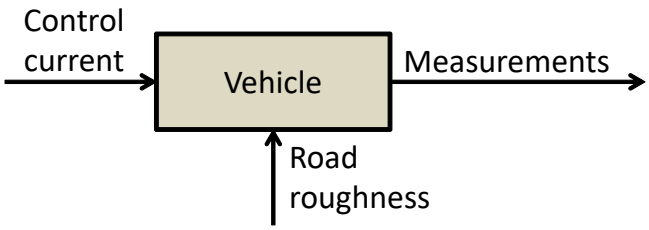

Figure 5.1: General scheme of MIMO system for investigated vehicle.

There are several approaches to mechanical modeling of a vehicle in literature. The most common is a quarter vehicle model, described e.g. by Majdoub [106]. The main assumption is to consider every vehicle's quarter separately, without taking into account the mutual interactions with the other quarters. Prabakar et al. presented half vehicle model, where both the vehicle's quarters on the front side are considered as one system, as well as both the vehicle's quarters on the rear side [107]. The most complicated variation is the full vehicle model, where all of the interactions between the vehicle's quarters are taken into account [108]. The vehicle models can be also categorized by the numbers of degrees of freedom (DoF). By this term it is meant the number of independent motions, allowed for the object. Typically, in the basic case 2-DoF system is assumed. However, many systems with higher number of DoF can be found in literature, e.g. 7-DoF [109] or 11-DoF [110].

In this dissertation a 2-DoF quarter vehicle model is considered. In general, the translational mechanical system can be denoted in matrix form as:

$$M\ddot{x} + C\dot{x} + Kx = F, \tag{5.1}$$

where: M, C, K are mass, damping and stiffness matrices, respectively, F is the applied force, and x is displacement. The presented quarter vehicle model (Fig. 5.2) can be expressed using the system of two differential equations:

$$m_u\ddot{x_1} = -c_u(\dot{x_1} - \dot{x_0}) - k_u(x_1 - x_0) + c_s(\dot{x_2} - \dot{x_1}) + k_s(x_2 - x_1) - F, \tag{5.2}$$

$$m_s\ddot{x_2} = -c_s(\dot{x_2} - \dot{x_1}) - k_s(x_2 - x_1) + F, \tag{5.3}$$

where: m_u is an unsprung mass, m_s is a sprung mass, $x_0 - x_2$ are the displacements, c_s and k_s are the damping and stiffness between unsprung and sprung masses, respectively, c_u and k_u are the damping and stiffness between unsprung mass and road, respectively, and i_{mr} is current applied to MR damper to generate force F.

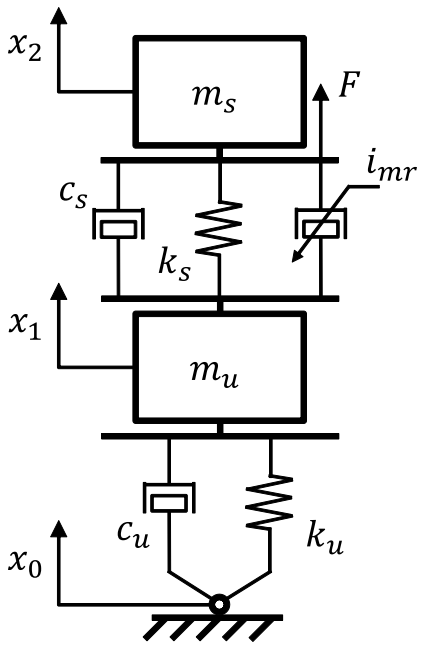

Figure 5.2: Quarter model of investigated vehicle.

5.3 Vibration attenuation

The main goal of the vibration control algorithms in vehicles is to reduce the sprung mass movement while driving through the obstacle. It can be achieved by a decrease

of the stiffness of the suspension at the moment of contact between the wheel and the road, and increase of stiffness of the suspension, when the sprung mass oscillates before returning to equilibrium position.

A Skyhook is the most common algorithm used for vibration control in semi-active vehicle suspension systems [111]. Optimally, the sprung mass is isolated from road induced vibration. Thus, the force generated by the MR damper should be proportional to the absolute value of vertical velocity of the sprung mass [102]:

$$F = -\delta |v_s|, \tag{5.4}$$

where: F is a force generated by the MR damper, v_s is an absolute value of vertical velocity of the sprung mass, and δ is a gain factor, tuned to achieve the highest attenuation of spring mass vibration. The value of current i_{mr} applied to the MR damper can be calculated from the following relation:

$$i_{mr} = \begin{cases} i(F, v_{mr}) & \text{for } v_s(v_s - v_u) > 0 \\ 0 & \text{for } v_s(v_s - v_u) \leq 0 \end{cases}, \tag{5.5}$$

where: v_{mr} is a vertical suspension velocity (MR damper), which is a difference between velocity of the sprung mass and velocity of the unsprung mass, and can be denoted as:

$$v_{mr} = v_s - v_u. \tag{5.6}$$

The current function $i(F, v_{mr})$ was obtained during the identification experiment of the MR damper [112]:

$$i(F, v_{mr}) = \left[\frac{-F - c_0 v_{mr} - \alpha_0}{\alpha_1 tanh(\beta_0 v_{mr}) + c_1 v_{mr}} \right]^2, \tag{5.7}$$

where: $\alpha_0 = 62.42$, $\alpha_1 = 1340$, $\beta_0 = 39.95$, $c_0 = 802.8$, and $c_1 = 488.5$. The experimental setup (Fig. 5.3) is based on the Freescale Sabre Lite main controller. It is used for data processing and to communicate with the other controllers, i.e. peripheral MCUs, and NI sbRIO. Every vehicle's quarter has its separate peripheral MCU to acquire data from accelerometers and hall sensors, and to control the MR damper. The LVDT sensor is connected to NI sbRIO through the dedicated signal conditioner. The data from LVDT is acquired and preprocessed using LabVIEW graphical environment, which supports NI hardware platforms. Both the accelerometers and LVDT sensors are used for estimation of the velocity of the suspension, while the Hall sensor is used for measurement of the rotational speed of the wheel. IMU sensor, placed under the

vehicle's seat, is used for measurement of the vehicle rotation, and driver's comfort. By the comfort a minimisation of the vertical acceleration affecting the driver is meant.

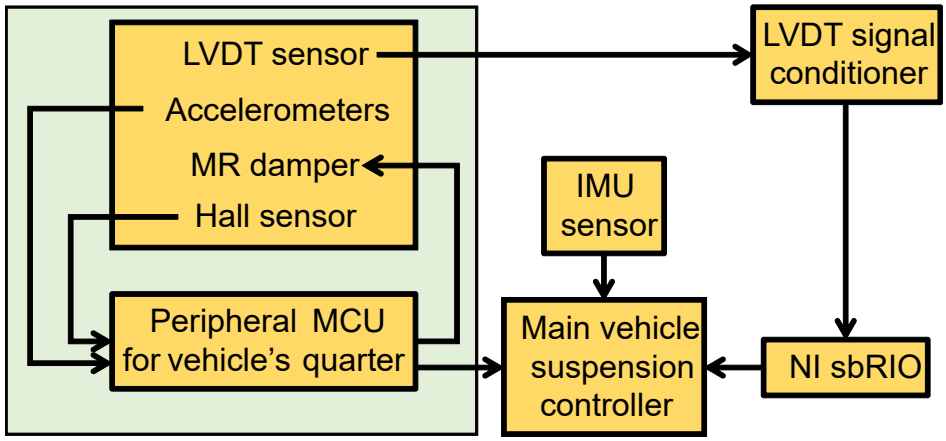

Figure 5.3: Scheme of measurement and control system for semi-active suspension of a single quarter of an ATV.

The movement of the vehicle through the obstacle can be divided into the separated stages. In the presented research it was assumed that the obstacle was 0.08 m thick single wooden beam with a square cross section (Fig. 5.4).

Figure 5.4: 0.08 m thick wooden beam, used as an obstacle, compared with investigated vehicle.

Thus, in this case the stages for the front left wheel are as follows (Fig. 5.5):

- I: The vehicle is near the obstacle, it can be assumed that vertical velocity of the vehicle suspension can be neglected.
- II: The wheel was bumped into the obstacle, and the front side of vehicle is moving up vertically, thus, the signs of the velocity of sprung and unsprung masses are the

same. However, the vertical speed of unsprung mass is higher than the vertical speed of sprung mass, due to the inertia of the spring in suspension. Using Equation 5.6 the final value of vertical velocity of vehicle suspension is negative.

- III: The spring in suspension is stretching, and the sprung mass is starting to move up vertically, while the unsprung mass is finishing its upward movement and is starting to falling down to the ground. Despite the different signs of the velocity of unsprung mass, in both cases, the final value of vertical velocity of vehicle suspension is positive.

- IV: During this stage the spring is returns to the balance state, pulling the sprung mass. The unsprung mass is finishing its downward movement and the wheel rebounds after contact with a ground. As in the previous stage, despite different signs of velocity of unsprung mass, the sign of final value of vertical suspension velocity remains the same — in this case it is a negative sign. After this stage the suspension oscillates before returning to the balance state.

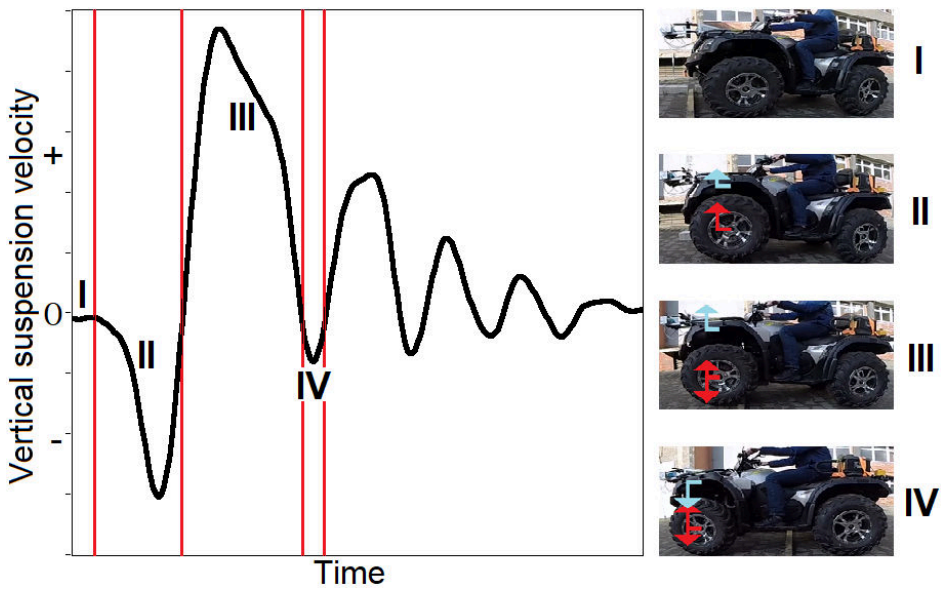

Figure 5.5: Stages of the movement of the vehicle through the 0.08 m wooden beam.

The stages for the other wheels will be the same, because of the quarter vehicle model assumption, thus, the other wheels will not be discussed. The stiffness of the semi-active vehicle suspension can be adjusted by changing the current that controls the viscosity of the MR fluid in damper. An increase of the current value increases the stiffness of the suspension. In Figure 5.6 a comparison of vertical suspension velocity

for each vehicle quarter is presented. In this case, suspension worked passively, and the five different current values were considered.

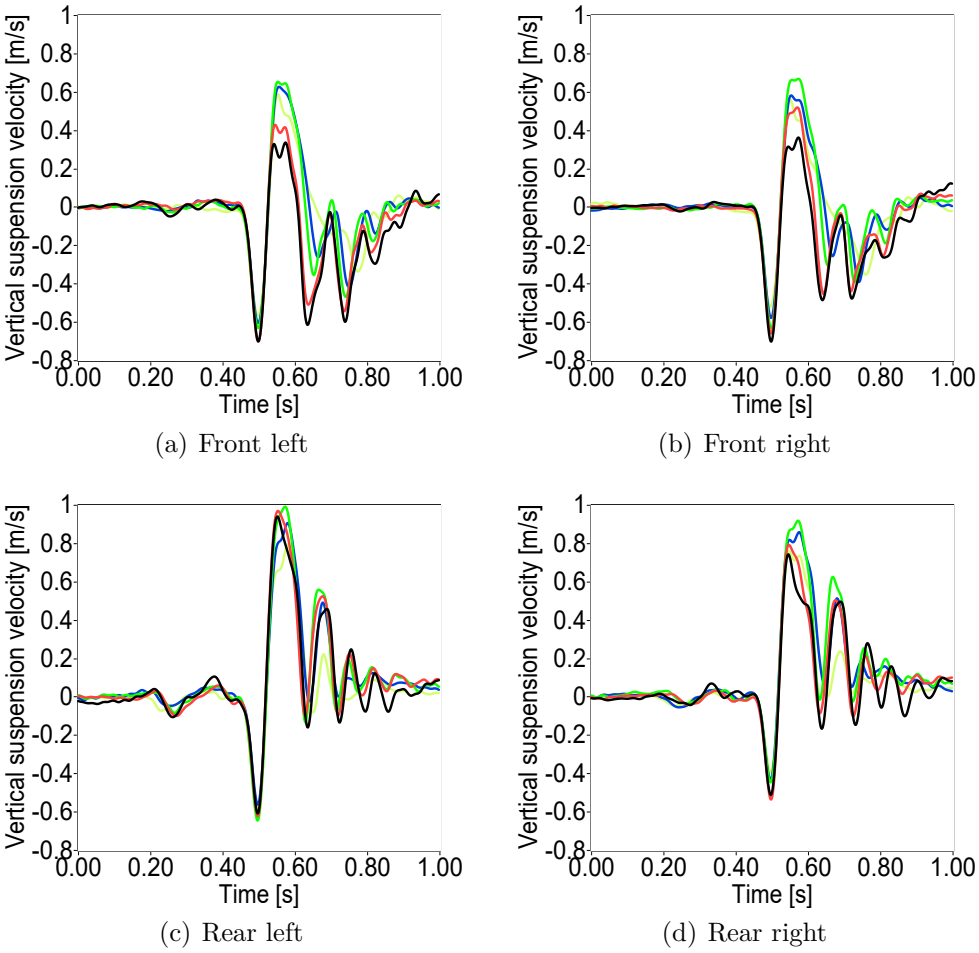

(a) Front left (b) Front right

(c) Rear left (d) Rear right

Figure 5.6: Velocity of the suspension estimated for each wheel and different currents: 0 A (black), 0.07 A (red), 0.13 A (green), 0.27 A (blue), and 0.53 A (light green).

It was observed that during stage III, the vertical suspension velocity increases with higher stiffness of the suspension. However, when the vertical suspension velocity reaches the negative values, the amplitudes are getting higher with the decrease of stiffness of the suspension. In Figure 5.7 the efficiency of vibration attenuation for different current values applied on MR dampers is compared. The vertical acceleration affecting the driver was measured using an IMU sensor.

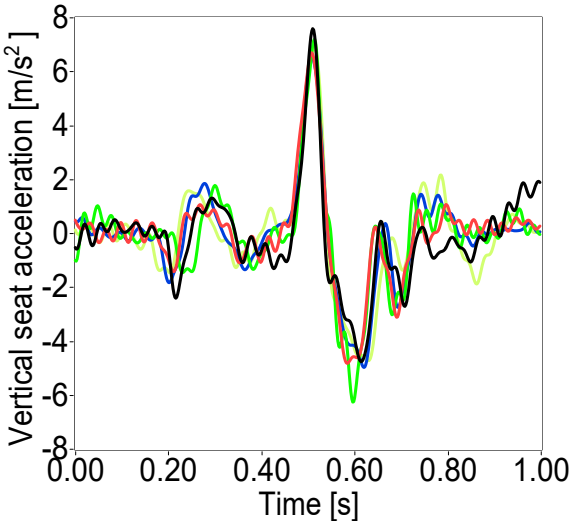

Figure 5.7: Comparison of vertical acceleration affecting the driver, for different currents: 0 A (black), 0.07 A (red), 0.13 A (green), 0.27 A (blue), and 0.53 A (light green).

The differences between the characteristics are not significant. Therefore, for a more accurate comparison in Table 5.1 RMS values of vertical acceleration affecting the driver are presented with corresponding values of current applied to MR dampers.

Table 5.1: RMS values of vertical acceleration with corresponding values of current.

MR current [A]	0	0.07	0.13	0.27	0.53
RMS acceleration [m/s^2]	4.53	4.49	4.69	4.57	4.81

The hardening of the suspension worsen the efficiency of the vibration damping in comparison to the zero-current, except 0.07 A. However, it is noteworthy that in this experiment only the passive case was considered, and stiffness of the suspension was constant in all of the stages. To obtain optimal vibration attenuation, the values of current applied to the MR dampers should vary between 0 A and other values, depending on the stage.

5.4 Estimation of suspension velocity using LVDT

As stated before, vertical suspension velocity is a crucial component in a control current function (Eq. 5.7), thus, its estimation should be as precise as possible. Typically, the accelerometers mounted on the sprung and unsprung masses are used [113,114]. Rarely, the data from accelerometers mounted on the sprung mass is replaced by acceleration

measurements, extracted from the IMU sensor [115]. Assuming the typical approach, the vertical suspension velocity can be estimated using the following formula:

$$v_i = \rho v_{i-1} + a_i \Delta t, \tag{5.8}$$

where: v_i is a vertical suspension velocity, ρ is a weight factor for the previous value of a vertical suspension velocity v_{i-1}, a_i is a vertical acceleration of vehicle suspension, and Δt is a 2.5 ms time step. An estimated value of velocity, using integration of the data acquired by the accelerometers, is affected by an integration error. To reduce the influence of previous iterations on current estimated value of velocity, the ρ weight factor was introduced, with the experimentally selected value 0.925. However, the upper accelerometers were mounted on the elastic part of the sprung mass, which makes them sensitive on undesired vibration sources, e.g. engine. LVDT sensors were assembled on the same screws as MR dampers, which allowed to direct measurement of the displacement of suspension in each quarter of the vehicle. The vertical suspension velocity was estimated using the following formula:

$$v_i = \frac{x_i - x_{i-1}}{\Delta t}, \tag{5.9}$$

where: v_i is a vertical velocity of vehicle suspension, x_i is the current displacement of the vehicle suspension, x_{i-1} is the previous value of displacement of the vehicle suspension, and Δt is a 2.5 ms time step. Both the methods of velocity estimation were compared for the same vehicle's runs, and two different values of control current: 0 A as a soft suspension and 0.27 A as a hardened suspension (Fig. 5.8).

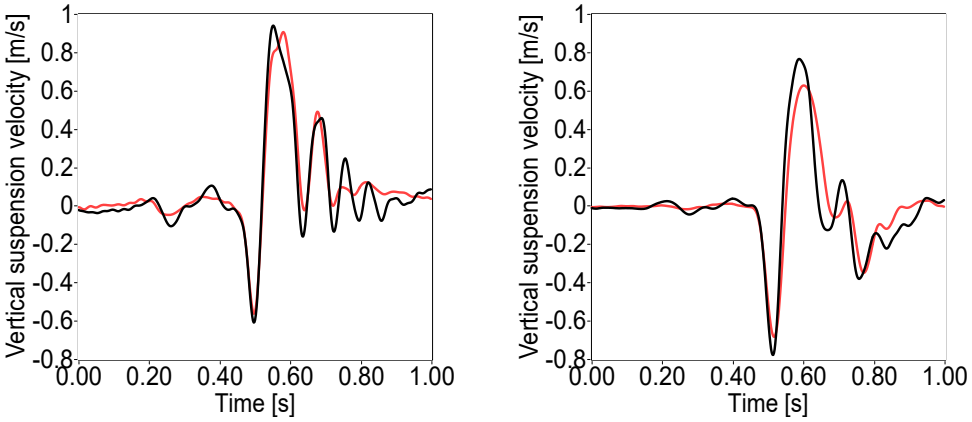

(a) Accelerometers (b) LVDT

Figure 5.8: Estimation of vertical suspension velocity of rear left quarter of vehicle using accelerometers (a) and LVDT (b) for 0 A (black) and 0.27 A (red) control current.

It was observed that in the II stage the amplitude of vertical suspension velocity estimated using LVDT is significantly lower than using the accelerometers. In the III stage the relation is opposite. In both cases the differences are approximately 0.2 m/s, which is 12.5% of the whole range. Moreover, for velocity estimation using accelerometers the oscillations of velocity after the IV stage are observed, while in case of using LVDT they are not present. The efficiency of vibration attenuation for vertical suspension velocity estimated using both the sensors were compared for semi-active suspension with the Skyhook algorithm (Eq. 5.5). The vertical acceleration affecting the driver was measured using the IMU sensor (Fig. 5.9).

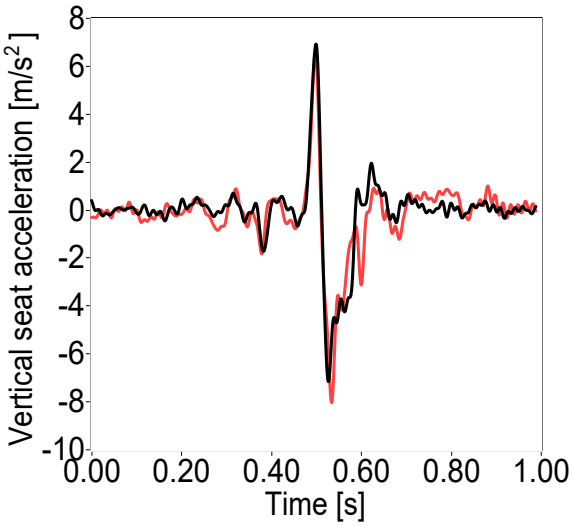

Figure 5.9: Comparison of vertical acceleration affecting the driver, for suspension velocity estimated using accelerometers (black) and LVDT (red).

The presented results are an average of the vehicle's four different runs. The gain factor δ was 2500. A comparison was difficult due to issues with experiment repeatability. The results depended on many factors, like e.g. position of the vehicle in relation to the obstacle, which should be perfectly perpendicular to ensure the same time of contact between the obstacle and the wheels on the same axle. The second factor is a vehicle speed, which should be constant for every vehicle's run. Despite the similar results for both the sensors, it is noteworthy that assembly of LVDT on the same mounting screws as MR dampers provides more reliable information about vertical suspension velocity.

5.5 Discussion

In this Chapter the MR vehicle suspension was investigated. The research was based on the ATV suspension quarter model with Skyhook algorithm, using a previously identified model of MR damper. An estimation of the vertical velocity of the vehicle suspension using LVDT sensors was proposed. It allows to reduce the influence of undesirable sources of vibration on the estimated velocity. One of these sources is engine vibration, propagated through the sprung mass, which affects on measurements acquired by upper accelerometers. The results obtained for both the sensors: accelerometers and LVDT, were compared using an IMU sensor placed under the vehicle seat to evaluate the efficiency of such an approach. The comparison of final results was not reliable, due to inability to provide repeatability of experiment scenario. However, assembly of the LVDT sensors makes the measurement robust on undesirable vibration sources, which allows to estimate vertical velocity of the vehicle suspension more precisely than using accelerometers.

Chapter 6

Summary

6.1 Conclusion

This dissertation is focused on vibration reduction, using mainly semi-active methods. However, in some cases, passive and active methods are also investigated to compare the efficiency of different solutions. Moreover, three different types of smart materials based structures were considered: a panel with piezoelectric elements, a double-panel wall internally coupled using electromagnetic elements, and an MR damper based suspension. The research covers a wide range of work varying from mathematical modeling of the vibrating structure, to the design, optimization, construction, and preliminary validation of the measurement device and coupling element.

The acoustic camera was constructed based on a previously designed and optimised microphone array, originally dedicated to vibrating panels mounted on a rigid frame casing. The device was preliminary validated using various objects, and it was proven that it can be used for the localization of sound sources in mid-low range.

The single panels were mathematically modeled, and the obtained modeshapes were used for optimization of the piezoelectric elements placement. The various methods of vibration reduction, i.e., passive, semi-active, and active were tested, and some of them were compared, depending on technical capabilities. However, by the passive systems not only open and short circuits are meant, but also passive implementation of SSDI. As expected, the active methods gave the best results, while the semi-active and passive systems were less efficient. It is noteworthy that the permanent stiffening of the piezoelectric elements magnify the amplitude of the vibration.

The influence of different types and materials of casing walls on a frequency response of a front panel was investigated. The plywood provided the highest efficiency

of vibration damping of a front panel, which may also be improved with the use of a double-panel structure as a front wall. However, the combination of the plywood and a double-panel structure was not investigated. It is noteworthy that the use of layered structures as the top and side walls allows for the shaping of the characteristics of the frequency response of a front wall.

The electromagnetic coupling element idea was described, and implemented. The element was preliminary validated, and the force characteristics were investigated depending on duty cycle values and selected parameters. The elements were mounted between the plates in a double-panel structure, and the experiments with different combinations of numbers of activated couplings and forces generated by elements were conducted. The main conclusion is that the highest efficiency in vibration reduction was achieved for the single, central coupling. In this case, the efficiency was considered as the minimization of maximal and mean vibration energy. Moreover, it was also observed, that the amplitude of the vibration was magnified in the places of anti-nodes and attenuated in areas of nodal lines. However, it is necessary to verify if the energy dissipated in observed areas are not transferred into the other areas of the structure that were not covered by the measurement grid.

Due to the need for visualization of modeshapes of the vibrating structure, a literature analysis in this area was conducted. In consequence, the acoustic camera was built for visualization of modeshapes, however, the SONAH or similar algorithm should be implemented to make it possible. Finally, it was decided to use Chladni's method with various modifications relative to its original form. It was necessary to use the vision imaging method for acquisition of the experimental results. The industrial camera and IR imaging were considered. Finally, the vision imaging with proper lighting was used. However, using IR imaging the rapid temperature fluctuations of the electromagnetic elements were observed. To avoid undesired consequences of heating of the structure it was decided to use stiff, magnetic couplings. The main conclusion is that the modified Chladni's method can be used to vizualize the modeshapes of the vibrating structure, however, due to its low precision it cannot be a reliable solution for observation of the energy distribution on the panel's surface.

The MR damper based suspension was investigated in the passive and semi-active ways. For the permanent change of the stiffness, results were worst when the current was applied to the MR damper in comparison to the soft suspension, however, with only one exception. The different approach for an estimation of vertical velocity of the suspension based on the LVDT sensors was also proposed. The placement of the sensors makes an estimation robust on the errors caused by undesirable vibration

sources. However, it was not possible to ensure repeatability of the following series during the experiment. Therefore, the proposed approach cannot be unequivocally validated.

Finally, in the author's opinion, the presented results allow for the conclusion, that by using electrical or electromagnetic induction phenoena in smart materials, it is possible to effectively reduce vibration of mechanical structures. It could be done by control the stiffness of the structure in selected areas or damping the vibrations in selected points of the structure. However, it should be noted, that improperly used damping system can even magnify the vibration. The examples are vertical suspension velocity in ATV, that should be estimated precisely, or the electrical charge stored in MFC element, that should be dissipated.

6.2 Author's contribution

The author believes that his contributions are following:

- Design and optimization of a microphone array, suitable for analysing noise radiated from a vibrating panel.
- Participation in development of the concept of a semi-active electromagnetic element for damping of transverse vibration of planar structures.
- Implementation and experimental validation of efficiency of semi-active electromagnetic damper with a push-pull solenoid.
- Proposition of a smart material, in macro scale, based on a double-panel with semi-active electromagnetic couplings.
- Development of a method for analysis of modeshapes of vibrating planar structures, based on Chladni's figures.
- Proposition of use of LVDT elements for estimation of vertical suspension velocity in the Skyhook algorithm, implemented on an experimental ATV.

6.3 Further research

The research presented in this dissertation covers a wide range of work described in Section 6.1. Moreover, during each experiment, new scientific and practical problems

were noticed. To investigate these aspects properly the dissertation should be broadly extended outside the scope of the presented research. In the author's opinion the following topics may be worthy of consideration:

- Implementation of the SONAH or similar algorithm on the acoustic camera, for a more precise analysis of the energy distribution on the surface of a vibrating panel.
- The use of the piezostack inside a double-panel structure instead of piezoelectric elements attached on the surface of a single panel.
- Investigation of a more complicated layered or sandwich structures, applied as the top and side walls on the device casing.
- The use of different types of electromagnetic coupling elements, which are more robust to rapidly increasing temperature.
- Development of a repeatable method for conducting the experiments with ATV, for reliable comparison of the estimation of vertical suspension velocity.

Bibliography

[1] S. S. Rao and Y. F. Fah, *Mechanical vibrations*. Prentice Hall, 5 ed., 2010.

[2] G. Kelly, *Mechanical vibrations: theory and applications*. Cengage Learning, 1 ed., 2011.

[3] W. A. Siswanto, M. Ibrahim, M. Madlan, and S. Mohamad, "Shaker table design for electronic device vibration test system," *International Journal of Engineering and Technology*, vol. 3, no. 6, pp. 664–668, 2011.

[4] S. Kashem, R. Nagarajah, and M. Ektesabi, *Vehicle suspension systems and electromagnetic dampers*. Springer, 1 ed., 2018.

[5] CMH-17, *Composite materials handbook vol.6: structural sandwich composites*. SAE International, 1 ed., 2013.

[6] A. Kelly and C. Zweben, *Comprehensive composite materials*. Elsevier Science Ltd., 1 ed., 2000.

[7] M. Schwartz, *Encyclopedia of smart materials*. John Wiley&Sons, 1 ed., 2002.

[8] A. Olabi and A. Grunwald, "Design and application of magnetostrictive materials," *Materials & Design*, vol. 29, no. 2, pp. 469–483, 2008.

[9] N. M. Wereley, *Magnetorheology: advances and applications*. The Royal Society of Chemistry, 1 ed., 2013.

[10] A. Khanicheh, D. Mintzopoulos, B. Weinberg, A. A. Tzika, and C. Mavroidis, "Evaluation of electrorheological fluid dampers for applications at 3-t mri environment," *IEEE/ASME Transactions on Mechatronics*, vol. 13, no. 3, pp. 286–294, 2008.

[11] M. Kciuk and R. Turczyn, "Properties and application of magnetorheological fluids," *Journal of Achievements in Materials and Manufacturing Engineering*, vol. 18, no. 1–2, pp. 127–130, 2006.

[12] A. Preumont, *Vibration control of active structures: an introduction*. Springer Netherlands, 3 ed., 2011.

[13] G. P. Gogue and J. J. Stupak, "Voice-coil actuators: insight into the design," in *Intelligent Motion*, pp. 241–253, 1989.

[14] I. Mancisidor, I. n. Laka, X. Beudaert, and J. Munoa, "Design and validation of an active damping device for chatter suppression on flexible workpieces," in *5th International Conference on Virtual Machining Process Technology*, 2016.

[15] M. Schwartz, *Smart materials*. CRC Press Taylor&Francis Group, 1 ed., 2009.

[16] M. Ferrara and M. Bengisu, *Materials that change color—smart materials intelligent design*. Springer, 1 ed., 2014.

[17] S. J. Rupitsch, *Piezoelectric sensors and actuators: fundamentals and applications*. Springer-Verlag Berlin Heidelberg, 1 ed., 2019.

[18] K. E. Wilkes and P. K. Liaw, "The fatigue behavior of shape-memory alloys," *The Journal of the Minerals, Metals & Materials Society*, vol. 10, no. 52, pp. 45–51, 2000.

[19] L. Yang, G. Meng, M. Shengfu, H. Yanting, and L. Jing, "Ultra-compliant liquid metal electrodes with in-plane self-healing capability for dielectric elastomer actuators," *Applied Physics Letters*, vol. 103, no. 6, p. 064101, 2013.

[20] R. Pelrine, P. Sommer-Larsen, R. D. Kornbluh, R. Heydt, G. Kofod, Q. Pei, and P. Gravesen, "Applications of dielectric elastomer actuators," in *Smart structures and materials 2001: electroactive polymer actuators and devices*, vol. 4329, pp. 335–349, International Society for Optics and Photonics, 2001.

[21] M. Pawełczyk, *Feedback control of acoustic noise at desired locations*. Silesian University Press, Gliwice, 2005.

[22] M. Pawełczyk, *Application-oriented design of active noise control systems*. Academic Publishing House Exit, Warsaw, 2013.

[23] S. Wrona and M. Pawełczyk, "Feedforward control of double-panel casing for active reduction of device noise," *Journal of Low Frequency Noise, Vibration and Active Control*, vol. 38, no. 2, pp. 787–797, 2019.

[24] Q. Mao, "Improvement on sound transmission loss through a double-plate structure by using electromagnetic shunt damper," *Applied Acoustics*, vol. 158, p. 107075, 2020.

[25] J. Wyrwał, M. Pawełczyk, L. Liu, and Z. Rao, "Double-panel active noise reducing casing with noise source enclosed inside - modelling and simulation study," *Mechanical Systems and Signal Processing*, vol. 152, p. 107371, 2021.

[26] P. Krauze, J. Kasprzyk, and J. **Rzepecki**, "Experimental attenuation and evaluation of whole body vibration for an off-road vehicle with magnetorheological dampers," *Journal of Low Frequency Noise, Vibration and Active Control*, vol. 38, no. 2, pp. 852–870, 2019.

[27] A. Pipinato, *Innovative bridge design handbook: construction, rehabilitation and maintenance*. Elsevier, 1 ed., 2015.

[28] P. Krauze, "Control of semiactive vehicle suspension system using magnetorheological dampers," PhD thesis, 2015.

[29] F. Gross, *Smart antennas for wireless communications*. McGraw-Hill Professional, 1 ed., 2005.

[30] S.-H. Shin and C. Cheong, "Experimental characterization of instrument panel buzz, squeak, and rattle (bsr) in a vehicle," *Applied Acoustics*, vol. 71, pp. 1162–1168, 2010.

[31] V. Cook and A. Ali, "End-of-line inspection for annoying noises in automobiles: trends and perspectives," *Applied Acoustics*, vol. 73, pp. 265–275, 2012.

[32] W. Lu, W. Jiang, H. Wu, and J. Hou, "A fault diagnosis scheme of rolling element bearing based on near-field acoustic holography and gray level co-occurrence matrix," *Journal of Sound and Vibration*, vol. 331, no. 15, pp. 3663–3674, 2012.

[33] T. Österlind, A. Archenti, L. Daghini, and C. M. Nicolescu, "Improvement of gear cutter dynamics by use of acoustic imaging and high damping interface," *Procedia CIRP*, vol. 4, pp. 17–21, 2012.

[34] J. **Rzepecki**, S. Budzan, S. Wrona, and M. Pawełczyk, "Performance analysis of the image fusion methods of the proposed 2d acoustic camera," in *23rd International Conference on Methods Models in Automation Robotics*, pp. 397–400, 2018.

[35] J. **Rzepecki**, S. Wrona, A. Chrapońska, K. Mazur, and M. Pawełczyk, "Acoustic camera as an universal tool to measure acoustic emission of devices," in *XXI National Conference on Discrete Process Automation*, pp. 185–192, 2018.

[36] I. McCowan, "Robust speech recognition using microphone arrays," PhD thesis, 2001.

[37] J. R. Underbrink, "Circularly symmetric, zero redundancy, planar array having broad frequency range applications," U.S. Patent 6,205,224, 2001.

[38] J. Hald, "Combined nah and beamforming using the same microphone array," *Sound and Vibration*, vol. 38, no. 12, pp. 18–27, 2004.

[39] J. Hald, "Basic theory and properties of statistically optimized near-field acoustical holography," *The Journal of the Acoustical Society of America*, vol. 125, no. 4, pp. 2105–2120, 2009.

[40] O. Bölke, J. Heimann, and J. García, "Modal analysis for damage detection in structures by non-contact measurements with a commercial microphone array," in *Proceedings of the 23rd International Congress on Acoustics*, pp. 142–148, 2019.

[41] C. Puhle, S. Barré, and S. Hollands, "On the sunflower spiral: acoustical holography results," in *Inter-Noise and Noise-Con Congress and Conference Proceedings*, pp. 5715–5726, 2016.

[42] R. Schmidt, "Multiple emitter location and signal parameter estimation," *IEEE Transactions on Antennas and Propagation*, vol. 34, no. 3, pp. 276–280, 1986.

[43] K. Zhang, J. Pan, and T. R. Lin, "Vibration of rectangular plates stiffened by orthogonal beams," *Journal of Sound and Vibration*, vol. 513, p. 116424, 2021.

[44] L. Zhao, "Low-frequency vibration reduction using a sandwich plate with periodically embedded acoustic black holes," *Journal of Sound and Vibration*, vol. 441, pp. 165–171, 2019.

[45] D. Chen, H. Zi, Y. Li, and X. Li, "Low frequency ship vibration isolation using the band gap concept of sandwich plate-type elastic metastructures," *Ocean Engineering*, vol. 235, p. 109460, 2021.

[46] J. Madeira, A. Araújo, C. Mota Soares, and C. Mota Soares, "Multiobjective optimization for vibration reduction in composite plate structures using constrained layer damping," *Computers & Structures*, vol. 232, p. 105810, 2020.

[47] K. Marakakis, G. K. Tairidis, P. Koutsianitis, and G. E. Stavroulakis, "Shunt piezoelectric systems for noise and vibration control: A review," *Frontiers in Built Environment*, vol. 5, pp. 1–17, 2019.

[48] S. Behrens, A. J. Fleming, and S. O. R. Moheimani, "Vibration isolation using a shunted electromagnetic transducer," in *Smart Structures and Materials 2004: Damping and Isolation*, vol. 5386, pp. 506–515, International Society for Optics and Photonics, 2004.

[49] C.-J. Lin, C.-Y. Lee, and Y. Liu, "Vibration control design for a plate structure with electrorheological atva using interval type-2 fuzzy system," *Applied Sciences*, vol. 7, no. 7, p. 707, 2017.

[50] K. Mazur, S. Wrona, and M. Pawełczyk, "Performance evaluation of active noise control for a real device casing," *Applied Sciences*, vol. 10, no. 1, p. 377, 2020.

[51] K. Mazur, S. Wrona, A. Chrapońska, J. **Rzepecki**, and M. Pawełczyk, "Synchronized switch damping on inductor for noise-reducing casing," in *26th International Congress on Sound and Vibration*, 2019.

[52] J. **Rzepecki**, A. Chrapońska, K. Mazur, S. Wrona, and M. Pawełczyk, "Semi-active reduction of device casing vibration using a set of piezoelectric elements," in *20th International Carpathian Control Conference*, 2019.

[53] K. Mazur, J. **Rzepecki**, A. Chrapońska, S. Wrona, and M. Pawełczyk, "Vibroacoustical performance analysis of a rigid device casing with piezoelectric shunt damping," *Sensors*, vol. 21, no. 7, p. 2517, 2021.

[54] A. Love, "The small free vibrations and deformation of a thin elastic shell," *Philosophical Transactions of the Royal Society A*, vol. 179, pp. 491–546, 1888.

[55] J. Gripp, L. Goes, and R. Pirk, "Dynamical modeling of an annular plate," in *VII Congresso Nacional de Engenharia Mecânica*, 2012.

[56] J. Reddy, *Theory and analysis of elastic plates and shells*. CRC Press, 2 ed., 2006.

[57] A. Leissa, *Vibration of plates*. National Aeronautics and Space Administration, 1969.

[58] Q. Mao and S. Pietrzko, *Control of noise and structural vibration. A MATLAB-based approach*. Springer, London, 1 ed., 2013.

[59] M. Dalaei and A. Kerr, "Natural vibration analysis of clamped rectangular orthotropic plates," *Journal of Sound and Vibration*, vol. 189, no. 3, pp. 399–406, 1996.

[60] S. Alisjahbana, "Dynamic response of clamped orthotropic plates to dynamic moving loads," in *The 13th World Conference on Earthquake Engineering*, 2004.

[61] N. Hagood and A. Flotow, "Damping of structural vibrations with piezoelectric materials and passive electrical networks," *Journal of Sound and Vibration*, vol. 146, no. 2, pp. 243–268, 1991.

[62] A. J. Fleming, S. Behrens, and S. O. R. Moheimani, "Reducing the inductance requirements of piezoelectric shunt damping systems," *Smart Materials and Structures*, vol. 12, pp. 57–64, 2003.

[63] S. Behrens, A. J. Fleming, and S. O. R. Moheimani, "A broadband controller for shunt piezoelectric damping of structural vibration," *Smart Materials and Structures*, vol. 12, pp. 12–28, 2003.

[64] J. J. Hollkamp, "Multimodal passive vibration suppression with piezoelectric materials and resonant shunts," *Journal of Intelligent Material Systems and Structures*, vol. 5, pp. 105–114, 1994.

[65] S. Behrens, S. O. R. Moheimani, and A. J. Fleming, "Multiple mode current flowing passive piezoelectric shunt controller," *Journal of Sound and Vibration*, vol. 266, pp. 929–942, 2003.

[66] M. Vatavu, V. Năstăsescu, F. Turcu, and I. Burda, "Voltage-controlled synthetic inductors for resonant piezoelectric shunt damping: a comparative analysis," *Applied Sciences*, vol. 9, no. 22, p. 4777, 2019.

[67] C. Kelley and J. Kauffman, "Adaptive synchronized switch damping on an inductor: a self-tuning switching law," *Smart Materials and Structures*, vol. 26, no. 3, pp. 1–10, 2017.

[68] C. Richard, D. Guyomar, D. Audigier, and H. Bassaler, "Enhanced semi-passive damping using continuous switching of a piezoelectric device on an inductor," in *Smart structures*, vol. 3989, pp. 288–299, 2000.

[69] C. Richard, D. Guyomar, D. Audigier, and G. Ching, "Semi-passive damping using continuous switching of a piezoelectric device," in *Smart Structures and Materials: Passive damping and isolation*, vol. 3672, pp. 104–111, 1999.

[70] E. Lefeuvre, A. Badel, L. Petit, C. Richard, and D. Guyomar, "Semi-passive piezoelectric structural damping by synchronized switching on voltage sources," *Journal of Intelligent Material Systems and Structures*, vol. 17, no. 8–9, pp. 653–660, 2006.

[71] A. Badel, G. Sebald, D. Guyomar, M. Lallart, E. Lefeuvre, and C. Richard, "Piezoelectric vibration control by synchronized switching on adaptive voltage sources: towards wide band semi-active damping," *Journal of the Acoustical Society of America*, vol. 119, pp. 2815–2825, 2006.

[72] H. Ji, J. Qiu, J. Cheng, and D. Inman, "Application of a negative capacitance circuit in synchronized switch damping techniques for vibration suppression," *Journal of Vibration and Acoustics*, vol. 133, no. 4, p. 041015, 2011.

[73] W. W. Clark, "Vibration control with state-switched piezoelectric materials," *Journal of Intelligent Material Systems and Structures*, vol. 11, no. 4, pp. 263–271, 2000.

[74] T. Wei, B. Wang, J. Cao, and B. Bao, "Experimental comparisons of two detection methods for semi-passive piezoelectric structural damping," *Journal of Vibration Engineering & Technologies*, vol. 5, pp. 367–379, 2017.

[75] N. G. Rocha de Melo Filho, L. Van Belle, C. Claeys, E. Deckers, and W. Desmet, "Dynamic mass based sound transmission loss prediction of vibro-acoustic metamaterial double panels applied to the mass-air-mass resonance," *Journal of Sound and Vibration*, vol. 442, pp. 28–44, 2019.

[76] X. Ma, H. Xiang, X. Yang, and J. Xiang, "Optimal geometric parameters for a double panel structure with low frequency forbidden characteristics," *Applied Acoustics*, vol. 177, p. 107944, 2021.

[77] H. Okumura, H. Ohmori, and A. Sano, "Adaptive hybrid approach to active noise and vibration control by piezoelectric ceramic transducers," *IFAC Proceedings Volumes*, vol. 43, no. 10, pp. 196–201, 2010.

[78] W. Larbi, J.-F. Deü, and R. Ohayon, "Finite element reduced order model for noise and vibration reduction of double sandwich panels using shunted piezoelectric patches," *Applied Acoustics*, vol. 108, pp. 40–49, 2016.

[79] J. P. Carneal and C. R. Fuller, "An analytical and experimental investigation of active structural acoustic control of noise transmission through double panel systems," *Journal of Sound and Vibration*, vol. 272, no. 3, pp. 749–771, 2004.

[80] B. Aloufi, K. Behdinan, and J. Zu, "Vibro-acoustic model of an active aircraft cabin window," *Journal of Sound and Vibration*, vol. 398, pp. 1–27, 2017.

[81] A. Akrout, L. Hammami, M. Ben Tahar, and M. Haddar, "Vibro-acoustic behaviour of laminated double glazing enclosing a viscothermal fluid cavity," *Applied Acoustics*, vol. 70, no. 1, pp. 82–96, 2009.

[82] S. Shi, G. Jin, and Z. Liu, "Vibro-acoustic behaviors of an elastically restrained double-panel structure with an acoustic cavity of arbitrary boundary impedance," *Applied Acoustics*, vol. 76, pp. 431–444, 2014.

[83] K. Idrisi, M. E. Johnson, A. Toso, and J. P. Carneal, "Increase in transmission loss of a double panel system by addition of mass inclusions to a poro-elastic layer: a comparison between theory and experiment," *Journal of Sound Vibration*, vol. 323, no. 1–2, pp. 51–66, 2009.

[84] Q. Mao and H. Shen, "Improvement on sound transmission loss through a double-plate structure by connected with a mass–spring–damper system," *Advances in Mechanical Engineering*, vol. 9, no. 7, pp. 1–9, 2017.

[85] Z. Sun, J. Sun, C. Wang, and Y. Dai, "Dynamic vibration absorbers used for increasing the noise transmission loss of aircraft panels," *Applied Acoustics*, vol. 48, no. 4, pp. 311–321, 1996.

[86] O. Akintoye, "Analytical modelling of sound transmission through finite clamped double-wall panels with magnetic-linked stiffness," *Acoustics Australia*, vol. 47, pp. 153–163, 2019.

[87] A. Chrapońska, J. **Rzepecki**, K. Mazur, S. Wrona, and M. Pawełczyk, "Influence of double-panel structure modification on vibroacoustical properties of a rigid device casing," *Archives of Acoustics*, vol. 45, no. 1, pp. 119–127, 2020.

[88] A. Chrapońska, J. **Rzepecki**, C. W. Isaac, K. Mazur, S. Wrona, and M. Pawełczyk, "Vibroacoustical properties of a double-panel structure with stiffness-varying couplings," in *27th International Congress on Sound and Vibration*, 2021.

[89] A. Chrapońska, J. **Rzepecki**, C. W. Isaac, K. Mazur, and M. Pawełczyk, "Spectral analysis of macro-fiber composites measured vibration of double-panel structure coupled with solenoids," *Sensors*, vol. 20, no. 12, p. 3505, 2020.

[90] J. **Rzepecki**, A. Chrapońska, S. Budzan, C. W. Isaac, K. Mazur, and M. Pawełczyk, "Chladni figures in modal analysis of a double-panel structure," *Sensors*, vol. 20, no. 15, p. 4084, 2020.

[91] J. **Rzepecki**, A. Chrapońska, K. Mazur, C. W. Isaac, S. Wrona, and M. Pawełczyk, "Analysis of noise emission of a device enclosed in a rigid casing with modified double-panel wall," in *27th International Congress on Sound and Vibration*, 2021.

[92] M. Pawełczyk, J. **Rzepecki**, and S. Wrona, "Semi-active electromagnetic element for damping of transverse vibration of planar structures," PL Patent 426875, 2018.

[93] W. J. Thayer, "Specification standards for electrohydraulic flow control servovalves," *MOOG Technical Bulletin*, vol. 117, pp. 1–24, 1962.

[94] B. Stoffregen and A. Felske, "Scanning laser doppler vibration analysis system," *SAE Technical Paper Series*, p. 850327, 1985.

[95] A. Stanbridge and D. Ewins, "Modal testing using a scanning laser doppler vibrometer," *Mechanical Systems and Signal Processing*, vol. 13, no. 2, pp. 255–270, 1999.

[96] E. Meteyer, S. Montresor, F. Foucart, J. Le Meur, K. Heggarty, C. Pezerat, and P. Picart, "Lock-in vibration retrieval based on high-speed full-field coherent imaging," *Scientific Reports*, vol. 11, no. 1, p. 7026, 2021.

[97] L. Yu and B. Pan, "Single-camera high-speed stereo-digital image correlation for full-field vibration measurement," *Mechanical Systems and Signal Processing*, vol. 94, pp. 374–383, 2017.

[98] E. Chladni and R. Beyer, *Treatise on acoustics, the first comprehensive english translation of E.F.F. Chladni's traité d'acoustique*. Springer International Publishing: Switzerland, 1 ed., 2015.

[99] B. Fijalkowski, *Automotive mechatronics: operational and practical issues*. Springer, 2 ed., 2011.

[100] D. Fischer and R. Isermann, "Mechatronic semi-active and active vehicle suspensions," *Control Engineering Practice*, vol. 12, no. 11, pp. 1353–1367, 2004.

[101] I. Jiregna and G. Sirata, "A review of the vehicle suspension system," *Journal of Mechanical and Energy Engineering*, vol. 4, no. 2, pp. 109–114, 2020.

[102] J. Kasprzyk, P. Krauze, S. Budzan, and J. **Rzepecki**, "Vibration control in semi-active suspension of the experimental off-road vehicle using information about suspension deflection," *Archives of Control Sciences*, vol. 27, no. 2, pp. 251–261, 2017.

[103] J. Kasprzyk, S. Budzan, J. **Rzepecki**, R. Marek, and P. Krauze, "Vibration control in semiactive suspension system of the experimental off-road vehicle using information about road roughness," in *XX National Conference on Discrete Process Automation*, 2016.

[104] P. Krauze, J. Kasprzyk, A. Kozyra, and J. **Rzepecki**, "Experimental analysis of vibration control algorithms applied for an off-road vehicle with magnetorheological dampers," *Journal of Low Frequency Noise, Vibration and Active Control*, vol. 37, no. 3, pp. 619–639, 2018.

[105] S. Kurczyk, "Soft computing algorithms for noise and vibration control," PhD thesis, 2018.

[106] K. E. Majdoub, F. Giri, and F. Chaoui, "Backstepping adaptive control of quarter-vehicle semi-active suspension with dahl mr damper model," *IFAC Proceedings Volumes*, vol. 46, no. 11, pp. 558–563, 2013.

[107] R. Prabakar, C. Sujatha, and S. Narayanan, "Optimal semi-active preview control response of a half car vehicle model with magnetorheological damper," *Journal of Sound and Vibration*, vol. 326, no. 3, pp. 400–420, 2009.

[108] M. Boreiry, S. Ebrahimi-Nejad, and J. Marzbanrad, "Sensitivity analysis of chaotic vibrations of a full vehicle model with magnetorheological damper," *Chaos, Solitons and Fractals*, vol. 127, pp. 428–442, 2019.

[109] P. Krauze, "Modelling and identification of magnetorheological vehicle suspension," in *17th International Conference on Methods and Models in Automation and Robotics*, pp. 228–233, 2012.

[110] S. H. Zareh, M. Abbasi, H. Mahdavi, and K. Ghaemi Osgouie, "Semi-active vibration control of an eleven degrees of freedom suspension system using neuro inverse model of magnetorheological dampers," *Journal of Mechanical Science and Technology*, vol. 26, pp. 2459–2467, 2012.

[111] D. Karnopp, M. J. Crosby, and R. A. Harwood, "Vibration control using semi-active force generators," *Journal of Engineering for Industry*, vol. 96, no. 2, pp. 619–626, 1974.

[112] J. Kasprzyk, J. Wyrwał, and P. Krauze, "Automotive mr damper modeling for semi-active vibration control," in *International Conference on Advanced Intelligent Mechatronics*, pp. 500–505, 2014.

[113] S. Jain, S. Saboo, C. I. Pruncu, and D. R. Unune, "Performance investigation of integrated model of quarter car semi-active seat suspension with human model," *Applied Sciences*, vol. 10, no. 9, p. 3185, 2020.

[114] G. Pepe, N. Roveri, and A. Carcaterra, "Experimenting sensors network for innovative optimal control of car wuspensions," *Sensors*, vol. 19, no. 14, p. 3062, 2019.

[115] D. Lee, S. W. Jin, E.-j. Rhee, and C. Lee, "Practical damper velocity estimation for semi-active suspension control," *International Journal of Automotive Technology*, vol. 22, no. 2, pp. 499–506, 2021.